Renewable Energy Integrated Power System Stability Assessment with Validated System Model Based on PMU Measurements

Chen Wang

Dissertation submitted to the faculty of the Virginia Polytechnic Institute and State University in partial fulfillment of the requirements for the degree of

Doctor of Philosophy
In
Electrical Engineering

Virgilio A. Centeno Chair
Jaime De La Reelopez
Vasileios Kekatos
Chetan Mishra
Steve C Southward
Haibo Zeng

May 2nd, 2019
Blacksburg, Virginia

Keywords: PMU measurement, Transmission line parameters estimation, Transient stability assessment with direct method, Constrained stability region, Low voltage ride through, Voltage security, Voltage prediction

Renewable Energy Integrated Power System Stability Assessment with Validated System Model Based on PMU Measurements

Chen Wang

ABSTRACT

Renewable energy is playing an increasingly significant role in power system operation and stability assessment with its numerous penetration expansion. This is not only brought by its uncertain power output and inverter-based equipment structures but also its operation characteristics like Low Voltage Ride Through (LVRT). It is thus necessary to take these characteristics into consideration and further to find more adaptive schemes to implement them for more effective analysis and safer power system operation. All the aforementioned is based on the accurate identification of the system fundamental information. In this dissertation, a systematic approach is proposed to find the valid system model by estimating the transmission line parameters in the system with PMU measurements. The system transient stability assessment is conducted based on this validated model. The constrained stability region is estimated with Lyapunov functions family based method in the center of angles reference frame considering renewables LVRT as operation limits. In order to integrate the LVRT constraints, a polytopic inner approximation mechanism is introduced to linearize and organize the transformed constraints in state space, which brings much scalability to the whole process. From the voltage stability perspective, an approach to adaptively adjust LVRT settings of the renewable energy sources in the system is formulated to guarantee the system load margin and thus the voltage security. A voltage prediction method is introduced for critical renewable energy sources identification. Estimation methods based on interpolation and sensitivities are developed and conducted for saving computation effort brought by continuation power flows. Multiple test cases are studied utilizing the proposed approaches and results are demonstrated.

Renewable Energy Integrated Power System Stability Assessment with Validated System Model Based on PMU Measurements

Chen Wang

GENERAL AUDIENCE ABSTRACT

Renewable energy utilization is continuously rising nowadays. They are clean but highly dependent on natural resources, which causes their uncertainty and intermittence in electric power output. The power system, on the other hand, is designed for schedulable and controllable power generators, which make the traditional methods for system operation and analysis of the system stability much less effective facing the trend of renewables integration. In this dissertation, a series of systematic approaches are proposed to firstly identify the system parameters for more accurate system modeling through PMU measurements, then to assess the system transient stability considering the renewable energy sources operation limits, and finally to adaptively adjust these operation limits for improving the system voltage security. The operation limits are transferred into the form in terms of system states. Linearization and approximation methods are also introduced to enhance the scalability of the processes. Multiple test cases are studied with the proposed approaches and the results demonstrate their effectiveness and efficiency.

Dedicated to Yan

ACKNOWLEDGEMENT

It has been a long journey until I reach this point of completing my Ph.D. study. There have been many outstanding instructors of mine enlightening me about the directions along the route. Among them, I would like to express my most sincere gratitude to my advisor, Dr. Virgilio A. Centeno for his guidance, instructions, and help during my Ph.D. program. His support is always encouraging me to seek for more constructive academic work. I will continue benefiting from his advice both in future career development and life.

At the same time, I would like to thank my committee members Dr. Jaime De La Ree, Dr. Vasileios Kekatos, Dr. Chetan Mishra, Dr. Steve C. Southward, and Dr. Haibo Zeng for the valuable suggestions, help, and efforts they have devoted to my research work in these four years. Their multi-disciplinary points of view encouraged me to expand the horizon and consider the research from a broader perspective.

It was also my honor to have an opportunity to receive insightful guidance from the great mind of Dr. James S. Thorp. His optimism, consistency in academic research, and unparalleled wisdom set up the unsurpassable role model that I will always admire. May he rest in peace.

I would also like to thank my colleagues Dr. Duotong Yang, Xiawen Li, Tapas Kumar Barik, Zhijie Nie, Elliott Mitchell-Colgan, Manish Singh, Jacques Delport, Yijun Xu, Andreas Schmitt, Huiying Huang for their support and help.

Most of all, I would like to thank my parents for their endless love and continuous support. This whole journey originates from their words and deeds. My fiancée, Dr. Yan Wang is the person makes this journey meaningful. I would like to thank her for her unconditional love, trust, and support. This is by far the best four years in my life. I believe the happiness she brought to us will never end.

Finally, I would like to gratefully acknowledge Dr. Kevin D. Jones for being a perfect mentor during my summer interns at Dominion Energy Virginia and Mr. Kyle Thomas, my supervisor at Dominion for his support.

CONTENTS

List of Figures

List of Tables

CHAPTER 1. INTRODUCTION

The high penetration of renewable energy sources (RES) is becoming a more distinctive characteristic in modern power system configuration. One important factor is the continuously increasing significance of the role played by renewable energy in global energy consumption[1]. Among the electric power energy consumed in one year, 25% are from RES according to the statistics collected in 2017[2]. Not only the consumption of renewable energy increases rapidly with 5.4% every year in the decade 2005-2015, but the total renewable power capacity is also doubled in the decade 2007-2017 which is estimated to be 178GW[2]. The increment is also impressive and estimated to account for 70% of net electric power capacity rise all over the globe in the year of 2017[3], which makes the total capacity of the global renewable energy reach 2195 GW[1]. There is also large potential in the further development of the renewable energy. Take the United States as an example, 18% of the electric power generation in 2017 is produced by RES[4]. There is in total more than 8000 GW of potential capacity for land-based wind and nearly 7000 GW of potential capacity for concentrating solar power in seven southwestern states in the United States[5]. It can be easily seen that there is immense development space for the renewable energy. The utilization of renewable energy will also witness its own prosperity with more resilient smart cities[6]–[9] construction featured with new elements equipment such as electric vehicles integration[10], [11] and more flexible control schemes inspired by cyber-physical systems and machine learning based methodologies[12].

However, with the integration of renewable energy into the various scale or level of power systems, there is also challenges to the control and operation of the system[13], [14], especially from the transient stability [15] and voltage security [16] perspectives. Most of the challenges are brought by the uncertainty of the original renewable resources these RES usage, such as wind or solar. This uncertainty also causes more conservative operation strategies in power grids with RES integrated to maintain system security [17]. One representative scheme is the Low Voltage Ride Through (LVRT), which is standardized in [18], that requires the curtailment or tripping off-line of the RES as system suffering from low voltage situations for system security. Therefore, it is necessary to find more adaptive methods to identify, analyze and control the system with RES's integrated, so that the system operation can be affected by the RES's in a more positive way.

1.1 Research Problem Description

1.1.1 System Model Validation with PMU Measurements

RES's are basically integrated into the system as new active power generation. This addition will naturally bring the original grid new patterns of operation and even topology changes. However, the power output of the RES's is intermittent which creates variations on the power flows. The variating heat caused by these currents will further influence the transmission line parameters[19] which will lead to inaccurate system identification and/or modeling for system analysis and control. This inaccuracy can consequently bring false operation state recognition and improper operator actions.

Particularly in nowadays utilities' operation, the static analysis of the system operation basically needs the information of power generation, load, and more importantly system topology and line parameters such as impedances. But large chances are that the utilities use merely the recorded value of the line parameters as they were installed. For transmission lines, the operation status may largely influence their impedances as aforementioned. There do exist multiple measuring devices in the system, Current Transformers (CTs) and Potential Transformers (PTs), which provide energy management center with current and voltage measurements. It is inevitable that these measurements have errors brought by the transforming process[20]. Therefore, it is necessary to develop an approach to eliminate these measurement errors and to find the instantaneous true system model.

Thanks to the wide utilization of the Phasor Measurement Unit (PMU), a large amount of synchronized measurement data can be acquired from the field. The database makes highly frequent line parameters estimation possible. Despite the convenience and advancement lead by the PMUs, they also lead to errors within the signal processing. These errors should also be considered when practicing the line parameters estimation.

1.1.2 System Transient Stability Assessment Considering Renewables LVRT Characteristics

The transient stability assessment of the power system is a conventional yet significant topic in the research field of power system[21]. The transient stability of a power system is categorized as rotor angle stability and basically reveals the capability of the generation within the system to regain synchronization after suffering from disturbances. The time frame studied is generally short term, 3-5 seconds after the disturbance and won't extend to be beyond 10-20 seconds for very large scale systems. For system transient stability assessment, most researchers focus on finding the stability region[22] of the system facing a particular disturbance which provides the critical clearing time[23] indicating the allowed time for the manual or automatic fault clearing actions to be taken to prevent the system collapse. There are some other critical concepts that are explained as follows for convenience in the subsequent narrative.

Synchronous Generator Rotor Angles and Angular Velocity: For each synchronous generator serving as a power source in the power system, its rotor angle δ refers to the phase angle difference between its terminal electromotive force $\dot{E}$ and voltage $\dot{U}$ at the connection point to the bulk system as is shown in Figure. 1 and Figure. 2. ω_0 refers to the synchronous angular velocity of the system. For 60 Hz system, $\omega_0 = 60 \times 2\pi$. Both the rotor angles and their angular velocities serve as system transient states.

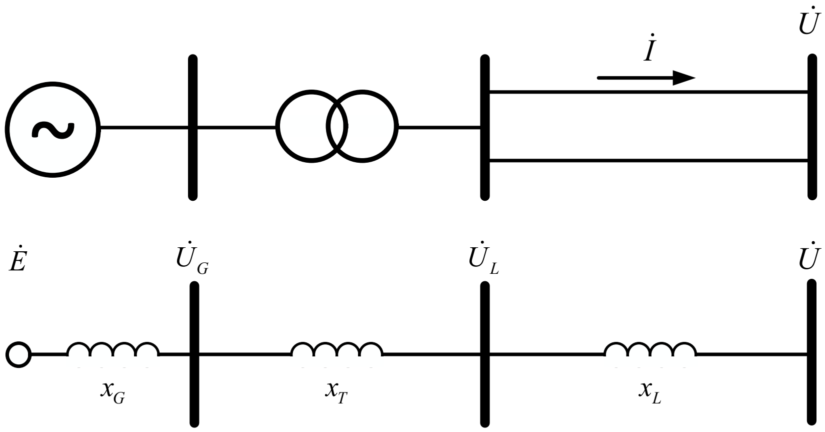

Figure. 1. Simple system diagram.

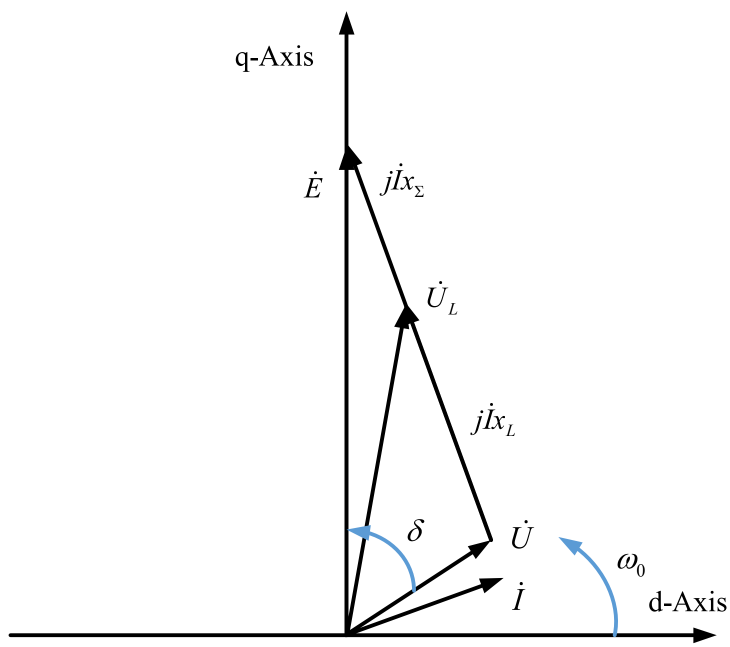

Figure. 2. Simple system phases.

Power system disturbances: The disturbances in a power system is generally defined as the sudden changes in system parameters or operation quantities happening in the system. For small disturbances, system dynamics can be linearized to be analyzed for simplicity, while large disturbances can not[24], [25]. The faults appearing in the system can be taken as a typical kind of disturbances.

Pre-fault, Fault-on, Post-fault system states: These three terms refer to the three stages of the fault happening and clearing. The pre-fault stage indicates the system states prior to the fault happening. The fault-on stage refers to the scenario where the concerned fault is acting and not cleared yet. The post-fault states indicate the system states after the fault is cleared. Normal system transient stability assessment mainly considers the post-fault initial state which is the system state right after the fault is cleared.

System State Space Model: The state space model of the system is in the form of differential-algebraic equation (DAE) set in terms of the aforementioned states, which is derived with the synchronous generators' dynamic swing equations (differential part) and static power flow equations (algebraic part) [26]. It reveals the time behavior of the system, or to be more specific, the mechanical and electrical power balance of the synchronous generators and power flow balance within the system.

Stable Equilibrium Point (SEP): The stable equilibrium point of the system refers to the system operating condition where the generators and the loads reach a balanced and stable operating condition, the equilibria. The system is to stay in this equilibria until other disturbance(s) happen. In the state space, this equilibrium is illustrated with a point indicating the corresponding vector of states.

Stability Region (SR): The stability region of a system under certain disturbance is a region if the state space, where all the state point within this region are certified to be stable. Any operating trajectory of the system starting with these points are guaranteed to converge to the SEP inside it. Normally there is only one SEP in each stability region. It is a typical invariant set where trajectories can never exit once enter it.

The most intuitive method to conduct the assessment is the time domain simulation[27] based on the system state space model. However, there are several deficiencies in the time simulation method. It is significantly time-consuming to conduct the simulation, especially for large scale systems. For different fault clearing time, there have to be different simulations conducted respectively which means that the simulation results are in the form of the system being stable or unstable for each fault and clearing time scenario. Many researchers have proposed to use direct methods to find estimated stability region in the state space which provides a clear idea of the stable boundary of the post-fault system states after suffering disturbances[28]–[30]. This approach is much more efficient and effective. The main objective is to find a proper energy function which best reveals the dynamic and energy damping characteristics of the original system that is modeled with differential and algebraic equations.

Besides the equality constraints in the form of these algebraic equations, the system can also be restricted by other operation limits in the form of inequality constraints. With RES's integration into the system, the LVRT curve can serve as a typical type of inequality constraints to maintain the RES's online. It can be projected toward the real world scenarios where the faults are cleared quickly and operators would like to have as little renewable energy capacity tripped offline as possible. Therefore, there is a need to find an approach transform the LVRT operation constraints into the state space and to estimate the LVRT constrained stability region targeting at providing the system operator with reference about clearing the faults while keeping RES's in the system functioning.

1.1.3 Renewables Adaptive LVRT Control Optimization Considering Voltage Security

The RES's Low Voltage Ride Through characteristic is generally considered as a precaution mechanism that prevents the RES's to feed the faults happening in the system which could cause damage to both the system and RES hardware[31], [32]. On the other hand, it can also be taken as a capability of the RES to withstand the disturbances. The purpose is to enable the system to feed more loads in operation when facing small disturbances. It is intuitively understandable that faults in the system may cause low voltage issues[33], [34] where buses with RES's installation may be tripped offline due to the voltage magnitudes exceeding the voltage lower limits set by the LVRT curve. The RES is trying to contribute to avoiding voltage collapse. On the other hand, the supplies are decreased for the tripping action. The system total generation capacity is declined. The capability of the system serving loads is thus sabotaged. It seems like a compromise between efficiency and system voltage security.

Nonetheless, the LVRT is more of an industry-recognized standard than a physical limit as the transmission line capacity constraint where the power flowing through the transmission line cannot exceed this limit otherwise overheating and other problems might happen. The curve and value of the LVRT are more flexible within a certain area close to the existing ones. This grants the space for adaptively adjusting the LVRT settings for better voltage security such as larger load margin the system can provide without losing RES's in some specific disturbed scenarios where maintaining the RES's online cannot bring negative influence. The approach to finding proper adjustment schemes under particular circumstances is the one to seek for better voltage security and RES's utilization.

1.2 Dissertation Outline

CHAPTER 2 provides the background of the PMU device and measurement. The data flow process from the measuring devices installed in the field to the utility energy management center is studied to analyze the data processing procedure. This procedure reveals the characteristics of the errors introduced into the measurements at various stages. The PMU data measurement error model is thus constructed. This model serves as the theoretical basis for the development of the transmission line parameters estimation method in the following chapter. The PMU measurements simulation process is also described and implemented providing a reference to the case studies in the following chapters.

CHAPTER 3 establishes the method of the transmission line parameters estimation. The positive sequence transmission line model utilized is provided as background. For each single transmission line, the estimation method is proposed based on the PMU measurement model derived in Chapter II. The corresponding PMU data sets configuration is described. The propagation approach of the estimation results is introduced to enable the estimation of all the transmission lines in the system without equipping multiple sets of costly revenue measurement devices. The propagation method covers both voltage and current measurements and facilitates the algorithm to traverse the complete system topology following the sequence path acquired through the proposed edge-based breadth-first search algorithm. The method proposed is applied to two study cases with different scales. The results are analyzed and discussed at the end of the chapter.

CHAPTER 4 addresses the constrained transient stability region estimation with direct methods considering renewables LVRT based on the validated system model from the previous chapter. The system state space model is described as a background in the first part of this chapter. The Lyapunov Function Family (LFF) in Center of Angle (COA) reference frame is proposed for stability region estimation. The concept of constrained stability region and renewables LVRT characteristics are also introduced as background. The LVRT constraints in terms of system states are derived and linearized. The approximation and combination process of these constraints are discussed in detail for being adapted to the proposed constrained stability region estimation method based on LFF. The complete process is implemented in a study case. The resulted estimation of the constrained stability region is demonstrated and discussed.

CHAPTER 5 focuses on developing an optimization scheme for adaptively adjusting LVRT settings of the RES's in the system so that the voltage security of the system can be guaranteed by satisfying the load margin limit. The background of the load margin and different types of system faults are discussed. With RES's tripping mechanism the system operation traces within the continuation power flow (CPF)[35] process is described. The interpolation method is utilized to simulate the state change when tripping occurs. A voltage prediction method is proposed to find out the critical RES's in the system without conducting time-consuming CPF procedure. The adjustment plans of these critical RES's LVRT constants are found. Their capability of increasing the load margin of the system to reach the limit is estimated with corresponding sensitivity. Feasible plans go through the optimization process and the optimal adaptive LVRT adjustment scheme is reached. The method is conducted on a study case and the results are analyzed.

CHAPTER 6 The results of the dissertation are stated and the conclusions are summarized. Future works are also listed for possible utilization and further development of the proposed work in this dissertation.

1.3 Contributions

The contributions of this work include,

1. Constructed of the PMU measurement error model considering both CT/PT measuring errors and quantization errors;
2. Developed of the PMU measurement data simulation process for further applications;
3. Updated single transmission line parameters estimation method considering PMU measurement data quantization characteristics;
4. Developed voltage/current measurement propagation method considering PMU measurement data quantization characteristics and parallel lines;
5. Proposed edge-based breadth-first search method for system topology information acquisition;
6. Formulated the system lines parameters estimation method combining the single line estimation with the voltage and current measurement propagation through topology sequence reached with edge-based breadth-first search;
7. Formulated the Lyapunov Functions Family approach in the center of angle reference frame;
8. Developed the optimal polytopic inner approximation of LVRT constrained feasibility region;
9. Proposed the system constrained stability region assessment approach considering LVRT constraints based on the Lyapunov Functions Family and LVRT constraints polytopic approximation method;
10. Developed system operation simulation considering renewables tripping with continuation power flow;

11. Proposed voltage prediction method and critical bus identification approach;

12. Formulated the optimal adaptive LVRT adjustment method.

CHAPTER 2. PMU DATA ANALYTICS

2.1 Introduction

The Phasor Measurement Unit (PMU)[36]is a widely used synchronized measurement device is modern power systems. This device does not directly measure voltages and currents in the system. It plays an important role in power system state identification by processing raw measurement data provided by conventional measurement devices CTs and PTs[37], [38]. By taking advantage of system frequency estimation and digital signal processing techniques like Discrete Fourier Transform (DFT), PMUs produce digital electric phasor measurements from sinusoidal signals provided by the aforementioned CTs and PTs. All these phasor measurements are time-stamped based on GPS devices built in the PMUs. With these time stamps, measurements from widely geographically distributed locations can be synchronized, which make wide area power system analysis far more realistic and accurate. Typical PMUs have a reporting rate of 30Hz, which is once every two cycles in a 60Hz power system. This rate is much faster than conventional widely deployed Supervisory Control and Data Acquisition (SCADA) systems[39]. With high reporting rates and synchronized time stamps, PMU measurements can be used for both static and dynamic analysis of the power systems. Relevant applications includes system modeling[40], fault location[41], state estimation[42], etc.

However, PMU measurements inevitably have errors. These errors are brought by both the source of data input into PMUs for processing and the processing procedure itself. The key input data provided by PMUs are voltage and current measurements obtained mostly from protection-type CTs and PTs installed across the power systems. These devices scale down the high voltage/current signals to the amount acceptable to PMU. This process leads to CT and PT ratio errors' integration into PMU measurements[20]. One of the practical ways to resolve the ratio error is to utilize revenue type CT/PT. However, it is not a cost-effective solution to apply these devices across the entire system due to their high economic cost.

In addition, most utilities only collect positive sequence data from their PMUs. These positive sequence measurements are computed directly from three-phase input signals affected individually by the aforementioned ratio errors. Due to the existence of un-transposed transmission lines, three-phase unbalance also has a negative impact on the accuracy of the measurements.

Several research works have conducted studies on the errors in PMU measurements in the past five years. Reference [43] provides a comprehensive study to estimate PMU measurement errors using nonlinear optimal estimation theory. The impact of the PMU measurement errors on the system dynamic load model is described and the stochastic distribution, as well as the frequency spectrum of the error, are analyzed in [44]. In reference [45], the PMU measurements errors are found to influence the system modeling in steady state. To resolve this problem, a calibration method using Least Squares Estimation (LSE) is proposed considering different PMU installation cases. Researchers also proposed estimating the CT and PT's ratio errors using PMU measurements. Wu et-al, from Virginia Tech, proposed a method to calibrate the instrument transducers using positive sequence PMU measurements in [46]. From the same institute, Pal et al. used a three-phase line model to calibrate the potential transformers with more accurate measurements [47].

All of the above research did not provide a comprehensive model to describe the complete data flow process from the input to the output of the PMUs. Namely, the data quantization when PMUs translate analog signals to digital signals has been ignored. Neither has the influence on the positive sequence data caused by these quantizations been paid any attention. Therefore, in this chapter, the author would like to build up a more detailed and accurate PMU measurement error model by analyzing the measurement data flow process of power system equipped with PMUs.

2.2 Power System Measurement Data Flow

Utilities' decision making relies highly on system states measurements and estimation results made based on these measured data. The knowledge of how the energy management systems (EMSs) receive the system operation conditions, or states, are vital for measurement errors analysis. In order to achieve a more accurate and realistic PMU measurement error model, the measurement data flow in normal power systems is studied here.

In general, after the transducers measured the analog signals of voltages and currents, these measurements are communicated to PMUs. Most of the PMU measurements used by utilities are from positive sequence signals. These data are transformed from individual three-phase measurements which are quantized by Analog to Digital Converters (ADC) inside PMUs. This quantization process will bring a loss of precision. A typical functional block diagram of the element in normal PMUs[48] is shown in Figure. 3.

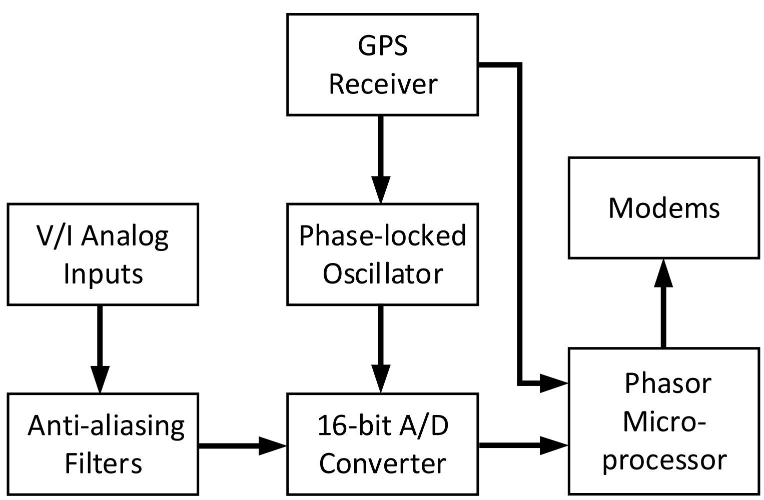

Figure. 3. Functional block diagram of the element in normal PMUs.

The general measurement data flow is shown in Figure. 4. The actual voltages on buses and currents flowing through transmission lines are measured by the installed CTs and PTs. Since the primary current is contributed by the core excitation current, there is a difference between the primary and the secondary values of the measurements in each one of the three phases. Due to these differences, ratio errors are inevitably added before the measurements are sent by the PMUs. After receiving the signals from CT and PTs, PMUs quantize each phase data and compute the positive sequence voltage or current phasor.

Hence, errors caused by different factors are accumulated within the measurements before they are sent to the central PMU data concentrator. Both the errors due to CT/PTs and PMUs can influence the accuracy of the system operation analysis, as well as the calculation of the line parameters. Therefore, the measurement data flowing process is to be analyzed to identify errors and to construct a math model of the PMU measurements to help build the basis for more realistic PMU measurement simulation and further applications like system parameter estimation.

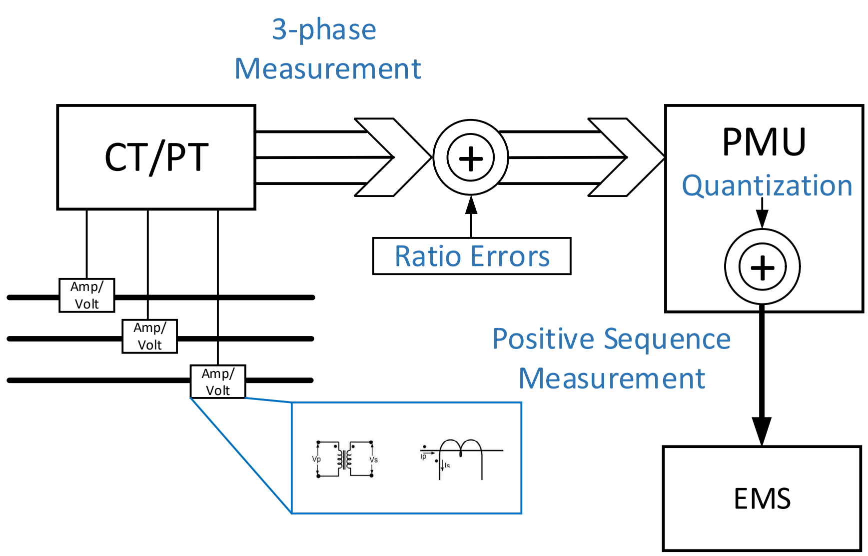

Figure. 4. Voltage and Current Measurement Data Flow.

2.3 PMU Measurements Error Model

The PMU measurement error model is built according to the previously discussed data flow. Ratio errors and quantization errors are added to accurate voltage and current values in the aforementioned sequence. Both the three-phase and positive sequence ratio errors are complex values. For each single transmission line, the relationship among true values, measurements, and ratio errors is shown in (2-1).

$$\begin{cases} V_{iM} = REV_i \times V_i \\ I_{iM} = REI_i \times I_i \\ V_{jM} = REV_j \times V_j \\ I_{jM} = REI_j \times I_j \end{cases} \tag{2-1}$$

where, REV_i, REI_i, REV_j, and REI_j are the ratio errors of voltage and currents on or flowing out of bus i and bus j, respectively.

For each phase, there is a different ratio error. Since these errors mainly depend on the transducers hardware, it can be assumed that during the time period of concern, such ratio errors remain fixed. According to the IEEE C57.13-2016 standard, the ratio errors are as follows:

$$\begin{cases} REV_A = r_{M1} \times e^{jr_{A1} \times \pi/180} \\ REV_B = r_{M2} \times e^{jr_{A2} \times \pi/180} \\ REV_C = r_{M3} \times e^{jr_{A3} \times \pi/180} \end{cases} \tag{2-2}$$

Where, REV_A is the ratio error of phase A voltage measurement; r_{M1} represents the magnitude error, and its lower and upper limits should be $[0.95, 1.05]$; r_{A1} denotes the error angle for phase A, and its lower and upper limits should be $\left[-5^\circ,\ 5^\circ\right]$; The ratio errors of the other two phases are similar to phase A.

The CTs and PTs integrate ratio errors to the three-phase measurements separately. The PMUs take the individual three phase values as input and computes positive sequence values, as well as single-phase values as output data. Therefore, without losing generality, taking the voltage measurement as an example, the positive sequence voltage measurements represented by ratio errors and true values are as follows:

$$V_{PM} = \frac{1}{3}\left(REV_A \cdot V_A + \alpha \cdot REV_B \cdot V_B + \alpha^2 \cdot REV_C \cdot V_C\right) \tag{2-3}$$

where, V_{PM} is the measured positive sequence voltage value; V_A, V_B, and V_C are the true values of three-phase voltages respectively; α is $e^{j2\pi/3}$.

If the three-phase voltage measurements are balanced, the measured positive sequence voltage should be

$$V_{PM} = \left(1/3\right)\left(REV_A + REV_B + REV_C\right) \times V_A \tag{2-4}$$

Therefore, the positive sequence ratio error can be computed as

$$REV_P = \frac{V_{PM}}{V_P} = \left(1/3\right)\left(REV_A + REV_B + REV_C\right) \tag{2-5}$$

where, V_P is the true value of positive sequence voltage.

However, for most field data, the transmission lines are usually un-transposed, which can cause three-phase unbalance in the measurements. Under such circumstances, equation (2-5) is no longer valid. The positive sequence ratio error for unbalanced three-phase data can be shown to be

$$
\begin{aligned}
REV_{P,ut} &= \frac{V_{PM}}{V_P} \\
&= \frac{\left(REV_A \cdot V_A + \alpha \cdot REV_B \cdot V_B + \alpha^2 \cdot REV_C \cdot V_C\right)}{V_A + \alpha \cdot V_B + \alpha^2 \cdot V_C} \\
&= \frac{\beta_A \cdot REV_A + \beta_B \cdot REV_B + \beta_C \cdot REV_C}{\beta_A + \beta_B + \beta_C}
\end{aligned} \tag{2-6}
$$

where, β_A , β_B , and β_C are three numerically complex values indicating the three-phase deviation from the positive sequence voltage, respectively.

As the three phases' ratio errors and the transposing condition of each transmission line remain constant, there is a constant positive sequence ratio error for each PMU measurements.

The quantization behavior of the three-phase PMU output data is described in [49]. All three-phase voltage and current data received by PMUs are quantized by some scale. Since the positive sequence measurements are directly transformed from the quantized three-phase data, the quantization errors are also indiscriminately integrated. For utilities, much attention is paid to the positive sequence measurements. Many of the deployed system estimators are established based on those data. However, the positive sequence measurement errors caused by the three-phase quantization cannot be simply taken as an additive error because of the positive sequence transformation process. Here, an analysis is conducted based on the design of a typical PMU from a major manufacturer, in order to demonstrate the quantization error characteristic of the positive sequence measurements.

According to [50], the three-phase sampling analog signals are processed by the ADC. Since the analog values are downscaled by the transducers, the absolute values are far smaller than the actual voltages and current, and the accuracy loss brought by this conversion is negligible. The converted digital samplings are used to calculate the phasor measurements. In the PMUs used for this study, these phasors are still three-phase at this stage. They are quantized and then transformed into positive sequence values to form the output. The quantization scales of the single-phase voltage and current measurements are associated with the measurement hardware. Based on manufacturer specifications, it is known that this PMU converts the phasors' real and imaginary parts into individual 16-bit digital signals. One of the 16 bits is used as the sign bit, and another is used for overvoltage or overcurrent operation. Therefore, there are only 14 bits to quantize the input signal. The detailed quantization scales for single-phase voltages and currents can then be calculated as follows:

$$v_{qs} = \left\lfloor \frac{V_B}{2^{14} \times \sqrt{3}} \right\rfloor \tag{2-7}$$

$$i_{qs} = \left\lfloor \frac{I_B}{2^{14} \times \sqrt{3}} \right\rfloor \tag{2-8}$$

Where, v_{qs} and i_{qs} are the quantization scales of voltages and currents; V_B and I_B are the base values of voltages and currents.

Based on this model, a simulation is conducted in the following section to demonstrate the erroneous effect of the quantization and positive sequence transformation.

2.4 PMU Measurement Data Simulation

The original voltage and current values are generated based on PSS\E power flow simulations, which serve as true values. The load status on which the power flows are based is acquired from a major utility. Two morning load pick-up hours data are selected. Each is from one summer peak load day and one winter load valley day respectively. The reason why the morning load pick hours are selected is that it is the most load-various hour in one day. This variety can provide the most significant diversity for further estimation applications. In order to simulate the 30Hz reporting rate of normal PMUs, shape-preserving(PCHIP) method with interpolant mode is utilized so that the load variations between existed samples in raw data could be acquired by the curve fitting functions. The interpolation results can be seen in the following figures.

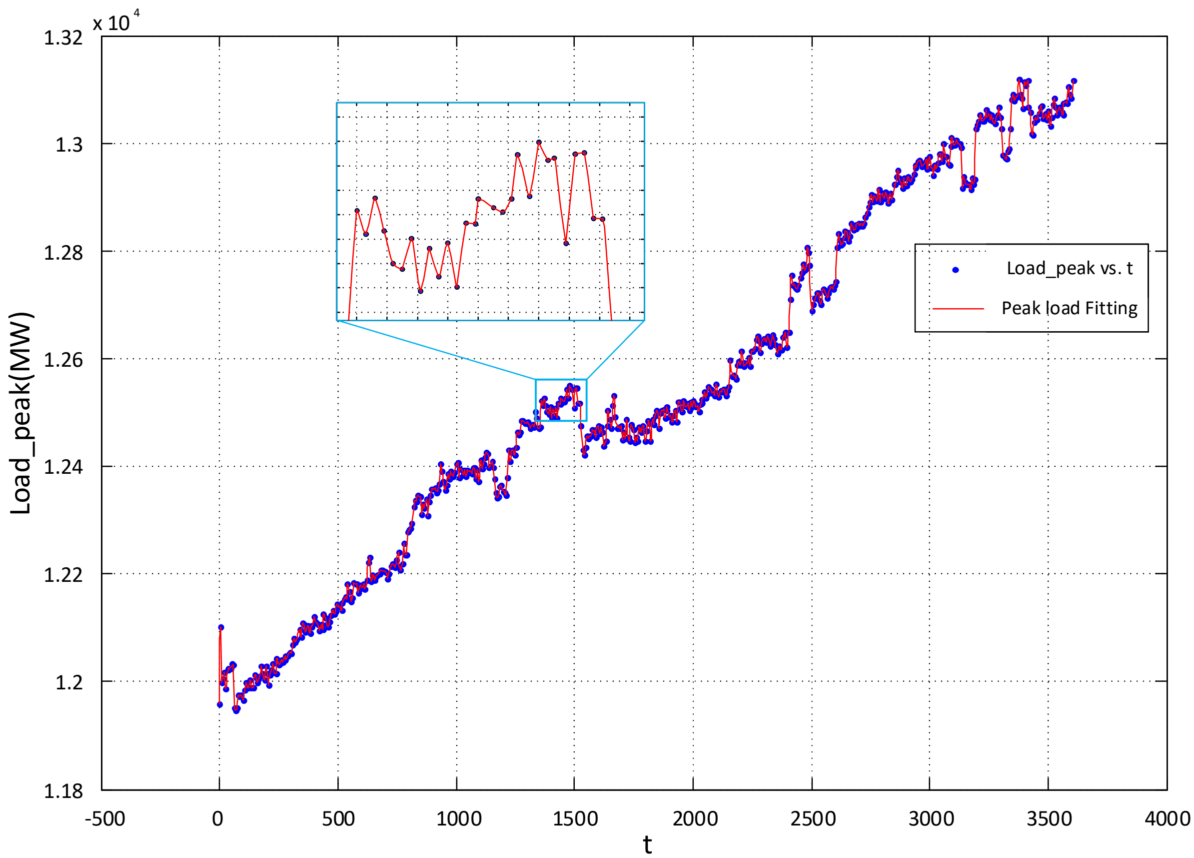

Figure. 5. Interpolant fitting results of the peak day morning pick-up hour load curve.

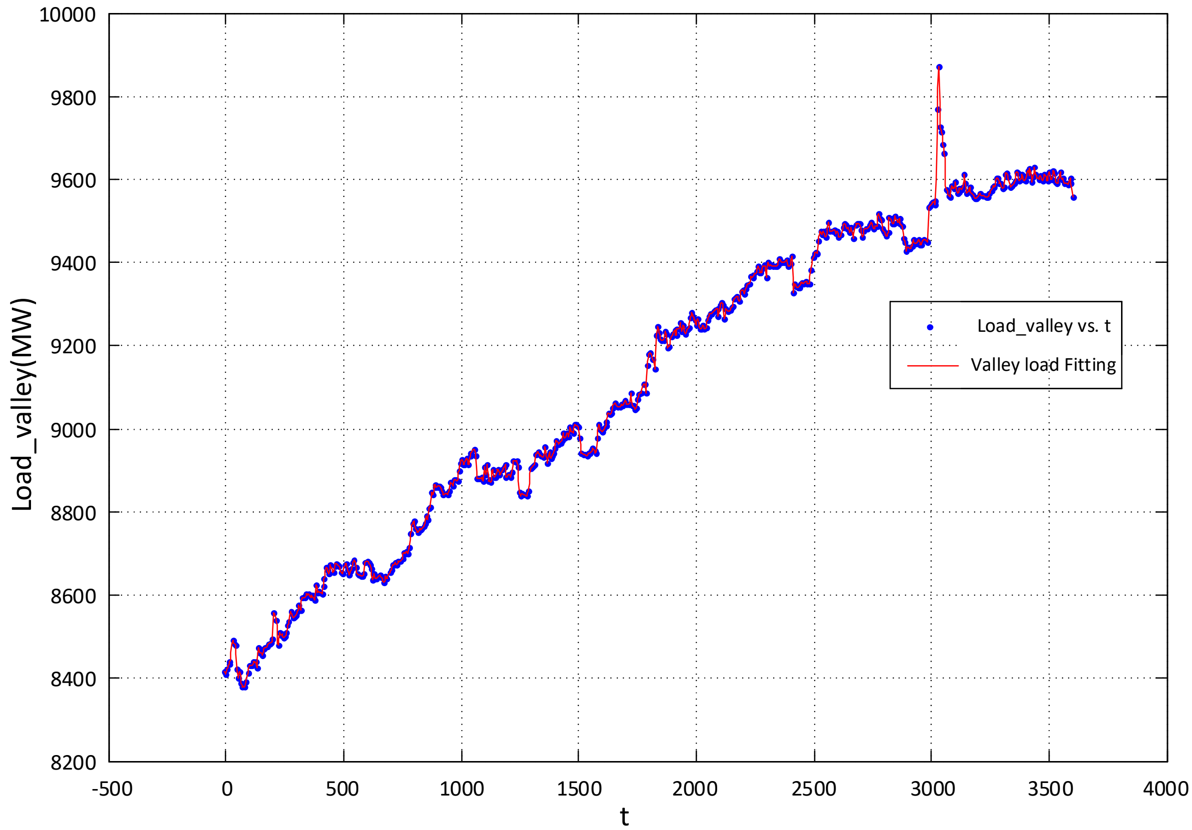

Figure. 6. Interpolant fitting results of the valley day morning pick-up hour load curve.

Here, the simulated three-phase data of one voltage measurement are quantized and taken as an example to demonstrate the effect of the positive sequence transformation after the quantization. The errors between the true values and the quantized ones of the three-phase and the positive sequence voltage data are shown in Figure. 7. The voltage level is 345KV and the histogram bin is set to be 1/20 of the quantization scale which is 12.16V.

As can be seen in Figure. 7, the quantization process causes loss of accuracy within the information of the three-phase measurements. For both real and imaginary parts of the three-phase voltage data ("VA real quant error" and so on), the quantization errors are uniformly distributed in general. As for the positive sequence data ("VP real quant error" and so on), the errors show bell shapes brought by the sum of three uniform distributions[51]. Notably, the expectation of such error is close to zero and therefore unbiased.

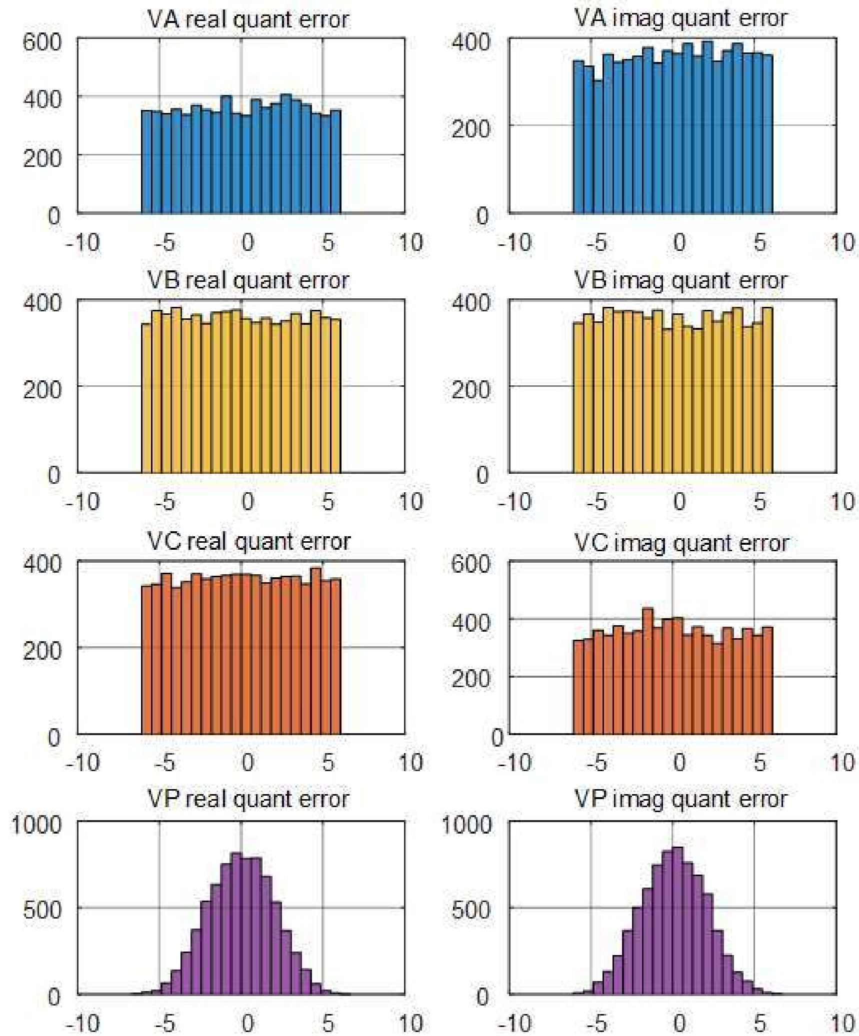

Figure. 7. Simulated Positive sequence and three-phase voltage quantization errors distribution histogram.

CHAPTER 3. TRANSMISSION LINES PARAMETERS ESTIMATION

3.1 Introduction

Under many circumstances in industry practices, it is assumed the transmission line parameters are accurate and invariant from the time of installation. However, the line parameters are significantly influenced by the conductor temperature and air moisture. Even though the power system is in quasi-steady state, the heat brought by the currents can cause the deviation of the line parameters from the default values. With accurate variation values or authentic immediate line parameters, the transmission operator can have a clearer and correct idea of the system's operating status. Additionally, knowledge of the actual system parameters allows researchers to construct more accurate system models for analysis and provide more effective relay settings. Reference [52] introduces a method to estimate one single transmission line's parameters using recursive regression based on a Kalman filter. Wu, Zora, and Phadke [53] have proposed an algorithm that serves a similar purpose to estimate both the three-phase line parameters and the ratio errors of the transducers. However, this method is aimed at the perfectly balanced three-phase system and does not provide a detailed processing method for the topological measurement propagation. More importantly, the paper does not consider the PMU quantization error and simply uses the ratio errors of the transducers as the error of the PMU measurements. An off-line methodology has been proposed in [54], which can estimate the single transmission line parameters with only one side of the line equipped with one PMU. Researchers in [55] focused on the un-transposed transmission line's parameters estimation. They combined the system state estimation and the three-phase line parameters real-time tracking. Gaussian white noise is used to simulate the PMU measurement errors. The transducers calibration and transmission line parameters estimation problem is also considered in [50]. Researchers derived the estimation problem with the perspective of taking CT/PT errors as probabilistic variables. While in the process of extending the estimation to the whole network, the researchers used regular LSE method to find the current measurements errors and did not consider the bounding constraints on ratio errors.

In this document, based on the PMU measurement error model for positive sequence voltages and currents introduced in the previous chapter, a detailed methodology is proposed to estimate the positive sequence transmission line parameters throughout the power system, where only one bus is assumed to be equipped with revenue class CTs and PTs. The algorithm considers each transmission line as a single section and each section's line parameters and ratio errors are estimated at the same time using LSE. The accuracy is then propagated to the consecutive lines following the tree topology of the system acquired through an edge-based search algorithm. The propagation methods utilized are an advancement upon the method introduced in [53]. When the whole process is completed, both the parameter estimation of all the concerned transmission line and the calibration of the corresponding instrument transducers are obtained at the same time.

3.2 Transmission Line Model

For a balanced transmission line, the single-phase π-section model can be utilized to model its electrical characteristics. The model consists of series resistance, reactance, and a shunt susceptance which is shown in Figure. 8, where V_i, I_i, V_j, and I_j represent the true voltages and currents on bus i and bus j, respectively; Z is the line impedance and y denotes the line susceptance; V_{im}, I_{im}, V_{jm}, and I_{jm} represent the voltages and currents measured by CTs and PTs installed on the corresponding buses.

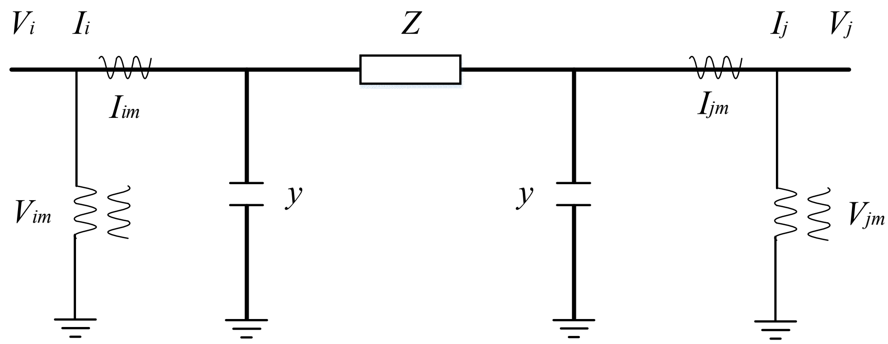

Figure. 8. Transmission line π-section model and CT/PT measurements.

3.3 Single Transmission Line Parameters Estimation

With the knowledge of the PMU measurement errors characteristics, in this section, a linear state estimation methodology based on the LSE is proposed to estimate the line parameters, including resistance R, reactance X, and shunt susceptance y, and the ratio errors of the CTs or PTs.

The methodology consists of two parts, single transmission line estimation and accuracy propagation. The process starts with one single transmission line. One of its two buses is equipped with a set of revenue class CTs and PTs, which means that the voltage and current measurements on this bus are highly accurate and are taken as the reference for the whole estimation process. Given the accurate measurements on the starting bus or "From bus", one can estimate its line parameters and the ratio errors of the measurements on the next bus ("To bus").

Different from [53], for this single line estimation, the PMU quantization errors are considered. Therefore, multiple times of LSE are performed using different sets of the original PMU data, instead of using the complete data set at once. Taking advantage of the error's unbiased characteristic, the average of the multiple estimation results is used to reach the final results, and the quantization error is thus reduced. Notably, the measurement quantity should be large enough and the measuring time period should be adequately long. So that the estimation processes will not be interfered by the singularity caused by the small data variance.

Since the "To bus" of the current concerned line is also the "From bus" of the consecutive line, if the accuracy can be propagated to the consecutive line, with the method discussed in this section, the consecutive line parameters can also be estimated and CT/PT calibrated. These steps can be extended throughout the system, and the parameters of all the lines in the system can be thus estimated. In this section, the content is focused on the single transmission line parameters estimation. The detailed propagation procedures will be described in the following section.

3.3.1 Transposed and Un-Transposed Transmission Line Parameters Estimation

Based on the π-section model shown in Figure. 8, one can find the relationship between the true positive sequence voltages/currents and the line parameters as shown in (3-1).

$$\begin{bmatrix} V_i \\ V_j \end{bmatrix} = \frac{1}{y\left(2+Zy\right)} \begin{bmatrix} 1+Zy & 1 \\ 1 & 1+Zy \end{bmatrix} \begin{bmatrix} I_i \\ I_j \end{bmatrix} \tag{3-1}$$

Take the impedance matrix $\mathbf{Z}$ as

$$\mathbf{Z} = \frac{1}{y\left(2+Zy\right)} \begin{bmatrix} 1+Zy & 1 \\ 1 & 1+Zy \end{bmatrix} \tag{3-2}$$

For the simplicity of the expression, the correction factors KV_i, KI_i, KV_j, and KI_j are introduced. These variables are the reciprocals of the aforementioned ratio errors and thus equivalent to these ratio errors. Using the products of the CT/PT measurements and correction factors to substitute the true values, (3-1) can be reformulated to be (3-3).

$$\begin{bmatrix} KV_i \times V_{iM} \\ KV_j \times V_{jM} \end{bmatrix} = \mathbf{Z} \cdot \begin{bmatrix} KI_i \times I_{iM} \\ KI_j \times I_{jM} \end{bmatrix} \tag{3-3}$$

where V_{iM}, V_{jM}, I_{iM}, and I_{jM} are the voltages and currents of bus i and bus j, respectively.

However, the positive sequence data send by PMUs are transformed from quantized three-phase data. The positive sequence quantization errors are as shown in (3-4).

$$\begin{cases} \varepsilon_{V_{iM}} = V_{iM} - V_{iM,q} \\ \varepsilon_{V_{jM}} = V_{jM} - V_{jM,q} \\ \varepsilon_{I_{iM}} = I_{iM} - I_{iM,q} \\ \varepsilon_{I_{jM}} = I_{jM} - I_{jM,q} \end{cases} \tag{3-4}$$

where, $V_{iM,q}$, $V_{jM,q}$, $I_{iM,q}$, and $I_{jM,q}$ are the positive sequence measurements transformed from the quantized three-phase data.

Therefore, substitute (3-4) into (3-3)

$$\begin{bmatrix} KV_i \times \left(V_{iM,q} + \varepsilon_{V_{iM}}\right) \\ KV_j \times \left(V_{jM,q} + \varepsilon_{V_{jM}}\right) \end{bmatrix} = \mathbf{Z} \cdot \begin{bmatrix} KI_i \times \left(I_{iM,q} + \varepsilon_{I_{iM}}\right) \\ KI_j \times \left(I_{jM,q} + \varepsilon_{I_{jM}}\right) \end{bmatrix} \tag{3-5}$$

In matrix form

$$\begin{bmatrix} V_{iM,q} + \varepsilon_{V_{iM}} \\ V_{jM,q} + \varepsilon_{V_{jM}} \end{bmatrix} = \begin{bmatrix} KV_i & 0 \\ 0 & KV_j \end{bmatrix}^{-1} \mathbf{Z} \begin{bmatrix} KI_i & 0 \\ 0 & KI_j \end{bmatrix} \begin{bmatrix} I_{iM,q} + \varepsilon_{I_{iM}} \\ I_{jM,q} + \varepsilon_{I_{jM}} \end{bmatrix} \tag{3-6}$$

By introducing a new variable $W = 1 + Z \cdot y$, (3-6) can be transformed into

$$\begin{bmatrix} V_{iM,q} + \varepsilon_{V_{iM}} \\ V_{jM,q} + \varepsilon_{V_{jM}} \end{bmatrix} = \hat{\mathbf{Z}} \cdot \begin{bmatrix} I_{iM,q} + \varepsilon_{I_{iM}} \\ I_{jM,q} + \varepsilon_{I_{jM}} \end{bmatrix} \tag{3-7}$$

where,

$$\hat{\mathbf{Z}} = \frac{1}{y(W+1)} \begin{bmatrix} W\dfrac{KI_i}{KV_i} & \dfrac{KI_j}{KV_i} \\ \dfrac{KI_i}{KV_j} & W\dfrac{KI_j}{KV_j} \end{bmatrix} \tag{3-8}$$

By reformulating (3-7), one has

$$\begin{bmatrix} V_{iM,q} \\ V_{jM,q} \end{bmatrix} = \hat{\mathbf{Z}} \cdot \begin{bmatrix} I_{iM,q} \\ I_{jM,q} \end{bmatrix} \underbrace{- \begin{bmatrix} \varepsilon_{V_{iM}} \\ \varepsilon_{V_{jM}} \end{bmatrix} + \hat{\mathbf{Z}} \cdot \begin{bmatrix} \varepsilon_{I_{iM}} \\ \varepsilon_{I_{jM}} \end{bmatrix}}_{\boldsymbol{\varepsilon}} \tag{3-9}$$

Based on the previous analysis, the quantization errors are unbiased. Therefore, the expectation of the quantization errors part, $\boldsymbol{\varepsilon}$, in the RHS of (3-9) should be a zero vector, which means

$$mean(\boldsymbol{\varepsilon}) \to - \begin{bmatrix} E\left[\varepsilon_{V_{iM}}\right] \\ E\left[\varepsilon_{V_{jM}}\right] \end{bmatrix} + \hat{\mathbf{Z}} \cdot \begin{bmatrix} E\left[\varepsilon_{I_{iM}}\right] \\ E\left[\varepsilon_{I_{jM}}\right] \end{bmatrix} = \begin{bmatrix} 0 \\ 0 \end{bmatrix} \tag{3-10}$$

Thus, with adequate measurements data to eliminate the quantization errors, the linear estimation problem can be formed as shown in (3-11).

$$\begin{bmatrix} \mathbf{I}_{iM,q} & \mathbf{I}_{jM,q} \end{bmatrix} \cdot \hat{\mathbf{Z}}^{\mathrm{T}} = \begin{bmatrix} \mathbf{V}_{iM,q} & \mathbf{V}_{jM,q} \end{bmatrix} - \boldsymbol{\varepsilon}^{\mathrm{T}} \tag{3-11}$$

where, $\mathbf{V}_{iM,q} = \begin{bmatrix} V_{iM,q}^{(1)} & V_{iM,q}^{(2)} & \cdots & V_{iM,q}^{(N)} \end{bmatrix}^{\mathrm{T}}$, which is the vector of the quantized voltage measurements provided by the PMU installed on bus i from N corresponding time stamps. The $\mathbf{V}_{jM,q}$, $\mathbf{I}_{iM,q}$, and $\mathbf{I}_{jM,q}$ are similar.

Using LSE and the single line parameters model formed as in (3-11), one can get the estimated impedance matrix:

$$\hat{\mathbf{Z}}^{\mathrm{T}} = \left(\mathbf{I}_{M,q}^{\mathrm{T}}\mathbf{I}_{M,q}\right)^{-1}\mathbf{I}_{M,q}^{\mathrm{T}}\mathbf{V}_{M,q} - \left(\mathbf{I}_{M,q}^{\mathrm{T}}\mathbf{I}_{M,q}\right)^{-1}\mathbf{I}_{M,q}^{\mathrm{T}}\boldsymbol{\varepsilon}^{\mathrm{T}} \tag{3-12}$$

where, $\mathbf{I}_{M,q} = \begin{bmatrix} \mathbf{I}_{iM,q} & \mathbf{I}_{jM,q} \end{bmatrix}$ and $\mathbf{V}_{M,q} = \begin{bmatrix} \mathbf{V}_{iM,q} & \mathbf{V}_{jM,q} \end{bmatrix}$.

By taking the average of results of multiple estimations, the second part on the right-hand side can be eliminated and the final estimation results can be reached using only the quantized data, as shown in (3-13).

$$\hat{\mathbf{Z}}_{final}^{\mathrm{T}} = \sum_{i=1}^{P} \hat{\mathbf{Z}}_i^{\mathrm{T}} \Big/ P \tag{3-13}$$

where,

$$\hat{\mathbf{Z}}_i^{\mathrm{T}} = \left[\left(\mathbf{I}_{M,q}^{(i)} \right)^{\mathrm{T}} \mathbf{I}_{M,q}^{(i)} \right]^{-1} \left(\mathbf{I}_{M,q}^{(i)} \right)^{\mathrm{T}} \mathbf{V}_{M,q}^{(i)} \tag{3-14}$$

which is the estimation results based on the i-th portion of the data when the original data set is separated into P portions.

It is to be noted that much attention should be paid to the measurement data selection and estimation dataset partition to avoid singularity and at the same time, to assure that the differences between portions of the measurements are not remarkable. Therefore, the average 'weighted' by data portions are almost equivalent to normal averages of the aforementioned part. Details about estimation dataset formulation will be discussed in the following subsection.

With the entries of $\hat{\mathbf{Z}}_{final}$: $\hat{Z}_{11}$, $\hat{Z}_{12}$, $\hat{Z}_{21}$, and $\hat{Z}_{22}$, the estimated impedance and susceptance can be calculated by first computing the estimated $\hat{W}$:

$$\hat{W} = \sqrt{\left(\hat{Z}_{11} \times \hat{Z}_{22} \right) \Big/ \left(\hat{Z}_{21} \times \hat{Z}_{12} \right)} \tag{3-15}$$

Given the correction factors of the voltage and current measurements of the bus i, namely KV_i and KI_i, the correction factors on bus j can be estimated as follow.

$$\begin{cases} KV_j = \left(1 \Big/ \hat{W} \right) \left(\hat{Z}_{11} \Big/ \hat{Z}_{21} \right) KV_i \\ KI_j = \hat{W} \left(\hat{Z}_{21} \Big/ \hat{Z}_{12} \right) KI_i \end{cases} \tag{3-16}$$

Then the estimated line impedance and susceptance can be calculated as shown in (3-17) and (3-18).

$$\hat{y} = \sqrt{\frac{1}{\det\left(\hat{\mathbf{Z}}_{final}\right)} \cdot \frac{KI_i KI_j}{KV_i KV_j} \cdot \frac{\left(\hat{W} - 1\right)}{\left(\hat{W} + 1\right)}} \tag{3-17}$$

$$\hat{Z} = \frac{1}{\hat{y}} \left(\hat{W} - 1 \right) \tag{3-18}$$

Notably, line susceptance should always be positive. Hence, in (3-17), the positive imaginary part of the square roots should be taken as the estimated susceptance. Based on the error characteristics discussed in Chapter II, it is easy to see that this line parameters estimation method can be used in both cases of transposed and un-transposed transmission lines.

3.3.2 Estimation Data Specification

The way to select measurement data and to partition it for estimation is required to satisfy several conditions as aforementioned. One factor that affects the estimation accuracy is the lack of variance on the PMU measurements when collected within a continuous time period. Under normal operating conditions, the equilibrium of the system is reached. Generally, the loads on the buses fluctuate smoothly. Thus, the fluctuation of the voltage and current measurements is not large in a short period. Such numerical characteristics could easily result in singularity during the computation process. Therefore, the data measured in the first second of each minute in one hour are chosen other than the data collected in consecutive minutes. The PMU output frame rate is set to be 30 frames/sec. So the measurement data set contains 1800 time instances in total. By selecting the measurements of one hour during morning load pick-up, considerable variation was introduced into the dataset and provided the option to conduct the estimation multiple times in one single day. As for the data partitioning for the results averaging process, all the first measurement frames of each second are used to form the first portion, all the second frames to form the 2nd portion, and so on so forth. Hence, there are 30 datasets in total for each transmission line and the estimation will be conducted 30 times with 60 time frames' data each time.

3.4 System Line Parameters Estimation

According to the single line estimation method, for each transmission line, it is critical to know the correction factors of the voltage and current values measured on one bus to conduct the line parameters estimation and to compute the correction factors of those measured on the other bus. At the same time, one reference bus has to be selected at the beginning of the whole process. One set of revenue CT and PT, that provides accurate measurements, should be installed on the reference bus. With these accurate data, the estimation on the parameters for the first transmission line can be performed and the CT and PT on the 'To Bus' can be calibrated. After the first line is estimated, the accuracy of the voltage and current measurements can be propagated to the consecutive lines with the following methods.

3.4.1 Voltage Measurement Accuracy Propagation

The voltage measurements on one bus always remain the same regardless of the measurements of the lines that connect to it. Based on this fact, if there are n lines that connected to bus i as shown in Figure. 9, the voltages measured by different PTs on those lines should satisfy (3-19):

$$V_i^{(true)} = KV_i^{(1)} \times V_{iM}^{(1)} = KV_i^{(2)} \times V_{iM}^{(2)} = \cdots = KV_i^{(n)} \times V_{iM}^{(n)} \tag{3-19}$$

where, $V_i^{(true)}$ is the true value of the voltage on bus i; $KV_i^{(j)}$ is the voltage correction factor of the PT measuring the voltage of bus i on line j; $V_{iM}^{(j)}$ is the voltage measurement on line j and $j \in \{1,\ 2,\ \ldots,\ n\}$.

Considering the quantization effect, the quantized measurements can be found following this relationship:

$$\begin{aligned} V_i^{(true)} &= KV_i^{(1)} \times \left(V_{iM,q}^{(1)} - \varepsilon_{V_{iM}}^{(1)} \right) = KV_i^{(2)} \times \left(V_{iM,q}^{(2)} - \varepsilon_{V_{iM}}^{(2)} \right) \\ &= \cdots = KV_i^{(n)} \times \left(V_{iM,q}^{(n)} - \varepsilon_{V_{iM}}^{(n)} \right) \end{aligned} \tag{3-20}$$

If one of the correction factors, $KV_i^{(j)}$, from the calibration of the previous line is given, for any of the other correction factors, $KV_i^{(k)}$, then

$$KV_i^{(j)} \times V_{iM,q}^{(j)} = KV_i^{(k)} \times V_{iM,q}^{(k)} \underbrace{- KV_i^{(k)} \times \varepsilon_{V_{iM}}^{(k)} + KV_i^{(j)} \times \varepsilon_{V_{iM}}^{(j)}}_{\varepsilon_V} \tag{3-21}$$

Because of the unbiased characteristic of the quantization error, i.e. $\mathrm{E}\left[\varepsilon_V\right] = 0$, one can use a similar method as in section 3.3 to average it out and find $KV_i^{(k)}$.

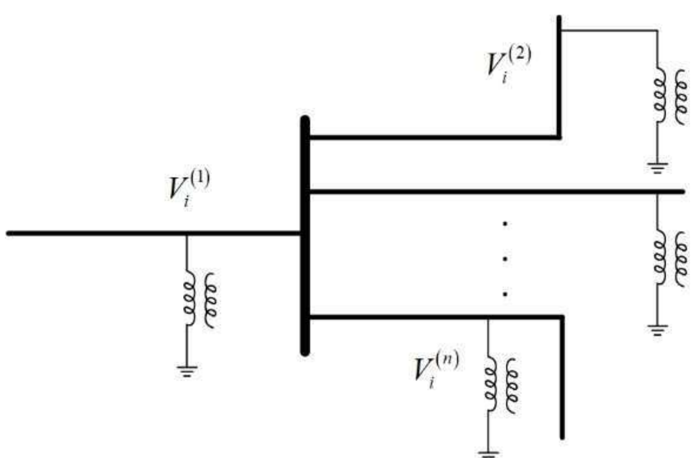

Figure. 9. Voltage Measurements on One Bus.

3.4.2 *Current Measurement Accuracy Propagation*

Apart from the accurate voltage measurement, the accurate current measurements on the same bus also need to be propagated to conduct an analysis of the consecutive line.

Based on Kirchhoff's current law (KCL), the currents injections on the bus i shown in Figure. 10 can be expressed as (3-22):

$$KI_i^{(1)} \times I_{iM}^{(1)} + KI_i^{(2)} \times I_{iM}^{(2)} + \cdots + KI_i^{(n)} \times I_{iM}^{(n)} = 0 \tag{3-22}$$

Given that one of the correction factors, $KI_i^{(1)}$, is known, (3-22) can be rewritten as (3-23). Such model forms another LSE problem that can be solved.

$$\begin{bmatrix} I_{iM}^{(2)} & I_{iM}^{(3)} & \cdots & I_{iM}^{(n)} \end{bmatrix} \begin{bmatrix} KI_i^{(2)} \\ KI_i^{(3)} \\ \vdots \\ KI_i^{(n)} \end{bmatrix}_{(n-1)\times 1} = \begin{bmatrix} -KI_i^{(1)} \cdot I_{iM}^{(1)} \end{bmatrix} \tag{3-23}$$

Because of the linearity of the estimation problem and the unbiased characteristic of the quantization errors, an averaging method similar to the one derived in the previous subsections can be used to deal with these errors. Therefore, one can directly reformulate (3-23) to be (3-24) and

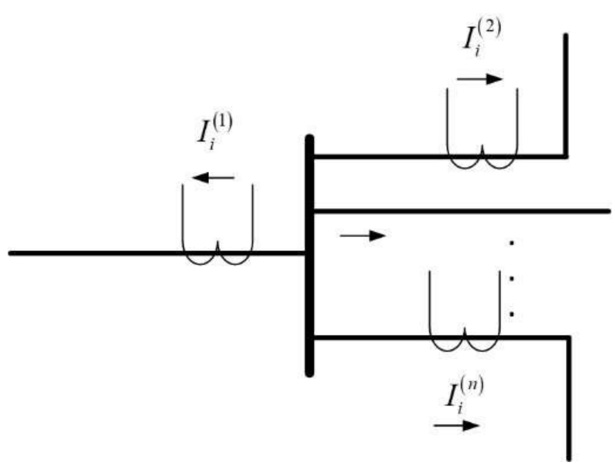

Figure. 10. Injection Currents Measurements on One Bus.

use different portions of the original quantized data to conduct the following optimization process. The final results will be the average of the optimums.

$$\begin{bmatrix} I_{iM,q}^{(2)} & I_{iM,q}^{(3)} & \cdots & I_{iM,q}^{(n)} \end{bmatrix} \begin{bmatrix} KI_i^{(2)} \\ KI_i^{(3)} \\ \vdots \\ KI_i^{(n)} \end{bmatrix}_{(n-1)\times 1} = \begin{bmatrix} -KI_i^{(1)} \cdot I_{iM,q}^{(1)} \end{bmatrix} \tag{3-24}$$

As stated in Section 2.2.1, the ratio errors have limits defined by the IEEE standard. Therefore, the correction factors values should be bounded constrained. Due to their definition, the constraints are in the form of magnitude and angles, but within the computation process, the ratio errors are calculated in the form of complex numbers. The constraints are projected from the polar coordinate plane into the complex plane and transferred from three single-phases into a positive sequence. The calculated constraints of the correction factors are shown in (3-25).

$$\begin{cases} K_{real} \in & [0.9452, \quad 1.0526] \\ K_{imag} \in & [-0.1005, \quad 0.1005] \end{cases} \tag{3-25}$$

where, K_{real} indicates the real parts of both the correction factors of current and voltage measurements and K_{imag}, the imaginary parts.

However, the constraints derived are in the real plane, while the estimation model as shown in (3-23) is in the complex plane. In order to consider the limits on the estimated results, the model is reformulated as (3-26), (3-27), and (3-28).

$$\mathbf{I}_{reshape} = \left[real\left(I_{iM,q}^{(2)}\right) \quad imag\left(I_{iM,q}^{(2)}\right) \quad \cdots \quad real\left(I_{iM,q}^{(n)}\right) \quad imag\left(I_{iM,q}^{(n)}\right) \right] \tag{3-26}$$

$$\mathbf{I}_{reshape}\begin{bmatrix} real\left(KI_i^{(2)}\right) \\ -imag\left(KI_i^{(2)}\right) \\ \vdots \\ real\left(KI_i^{(n)}\right) \\ -imag\left(KI_i^{(n)}\right) \end{bmatrix}=\left[real\left(-KI_i^{(1)}\cdot I_{iM,q}^{(1)}\right)\right] \tag{3-27}$$

$$\mathbf{I}_{reshape}\begin{bmatrix} imag\left(KI_i^{(2)}\right) \\ real\left(KI_i^{(2)}\right) \\ \vdots \\ imag\left(KI_i^{(n)}\right) \\ real\left(KI_i^{(n)}\right) \end{bmatrix}=\left[imag\left(-KI_i^{(1)}\cdot I_{iM,q}^{(1)}\right)\right] \tag{3-28}$$

where, $real\left(I_{iM,q}^{(j)}\right)$ and $imag\left(I_{iM,q}^{(j)}\right)$ are the column vectors contain real and imaginary parts of the quantized measurements of the currents flowing out of bus i through line j within the concerned time duration, respectively; $real\left(KI_i^{(j)}\right)$ and $imag\left(KI_i^{(j)}\right)$ are the real and imaginary parts of the corresponding correction factors; $real\left(-KI_i^{(1)}\cdot I_{iM,q}^{(1)}\right)$ and $imag\left(-KI_i^{(1)}\cdot I_{iM,q}^{(1)}\right)$ are the real and imaginary parts of calibrated current measurements.

The propagation process can be conducted on the whole transmission subsystem in systems with a mesh network structure. Chances are that multiple lines connecting the current bus be estimated and the currents flowing through them out of the bus are known. Under these circumstances, the known currents can be simply moved to the right-hand side of the equations so that all the correction factors of the other lines can be estimated.

There are also some scenarios where there are double parallel lines or even triple parallel lines connecting two buses. There is a large probability that the currents flowing through such multiple lines are similar or even the same, i.e. the difference of the measurements are small or close to zero, which severely influences the estimation accuracy. For example, if $I_{iM,q}^{(2)}$ and $I_{iM,q}^{(3)}$ are the two currents flowing out of bus i through line 2 and line 3 respectively and those two lines are two parallel lines connecting bus i and bus j, then the true values of those two currents are the same. Without pre-processing, even with constraints on the correction factors, the least squares optimization results could possibly be that $KI_i^{(2)}$ is around $1.0526 + j0.1005$ and $KI_i^{(3)}$ is around $0.9452 - j0.1005$. The correction factors' values are pushed to the limits and the accurate results are covered. Furthermore, part of the contribution of $I_{iM,q}^{(3)}$ to $I_{iM,q}^{(1)}$ is counted as $I_{iM,q}^{(2)}$'s. The solution to this issue is finding all the measurements of parallel lines and sum them together. The correction factors will also be summed up to one. The estimation process, in this case, is not aimed to find each accurate current but to find one accurate summation. Theoretically, with the same length, material, and operation environment, the currents flowing through those parallel lines should be the same. Therefore, with the accurate summation divide by the number of parallel lines, the accurate current flow through one line can be reached. With the measurements on other lines, the correction factors can be calculated by taking the ratio of the true value and measurements respectively.

The estimation model formed previously can be simply transferred into a typical quadratic optimization problem with the bounded constraints listed in (3-25). The problem can be expressed as follows:

$$\begin{aligned} \min \quad & \left\| \mathbf{I}_{reshape} \mathbf{A}_1 \mathbf{k} - \mathbf{I}_{true,real} \right\|_2^2 + \left\| \mathbf{I}_{reshape} \mathbf{A}_2 \mathbf{k} - \mathbf{I}_{true,imag} \right\|_2^2 \\ s.t. \quad & l_{real} \le \mathbf{k}_{real} \le u_{real} \\ & l_{imag} \le \mathbf{k}_{imag} \le u_{imag} \end{aligned} \tag{3-29}$$

where,

$$\mathbf{k} = \left[real\left(KI_i^{(2)}\right) \quad imag\left(KI_i^{(2)}\right) \quad \cdots \quad real\left(KI_i^{(n)}\right) \quad imag\left(KI_i^{(n)}\right) \right]^{\mathrm{T}} \tag{3-30}$$

$$\mathbf{A}_1 = \begin{bmatrix} \mathbf{B}_1 & & \underline{\mathbf{0}} \\ & \ddots & \\ \underline{\mathbf{0}} & & \mathbf{B}_1 \end{bmatrix}, \ \mathbf{B}_1 = \begin{bmatrix} 1 & 0 \\ 0 & -1 \end{bmatrix} \tag{3-31}$$

$$\mathbf{A}_2 = \begin{bmatrix} \mathbf{B}_2 & & \underline{\mathbf{0}} \\ & \ddots & \\ \underline{\mathbf{0}} & & \mathbf{B}_2 \end{bmatrix}, \ \mathbf{B}_2 = \begin{bmatrix} 0 & 1 \\ 1 & 0 \end{bmatrix} \tag{3-32}$$

$\mathbf{I}_{true,real}$ is the vector that contains the real parts of the accurate current measurements and $\mathbf{I}_{true,imag}$ contains the imaginary parts; $\mathbf{k}_{real}$ and $\mathbf{k}_{imag}$ are vectors that contain real and imaginary parts of the correction factors, respectively; l_{real}, u_{real}, l_{imag}, and u_{imag} are the corresponding lower and upper limits vectors.

With the bounded constrained trust-region-reflective quadratic optimization method and the current injections measurements, the correction factors of all the other lines connected to the concerned bus can be estimated. Provided that the calculated voltage correction factor and estimated current correction factor are known, the estimation on the consecutive transmission line can be performed.

3.4.3 Edge-Based Breadth-First Search Method

Based on the former propagation methods, the accuracy of the reference bus can be passed to the consecutive lines through the interconnected topology of the system. Given that transmission systems usually form mesh-structured networks, the edge-based Breadth-first Search (BFS) algorithm is utilized in this work to construct the tree topology with the reference bus as the root. The flow chart of this algorithm can be found in Figure. 11.

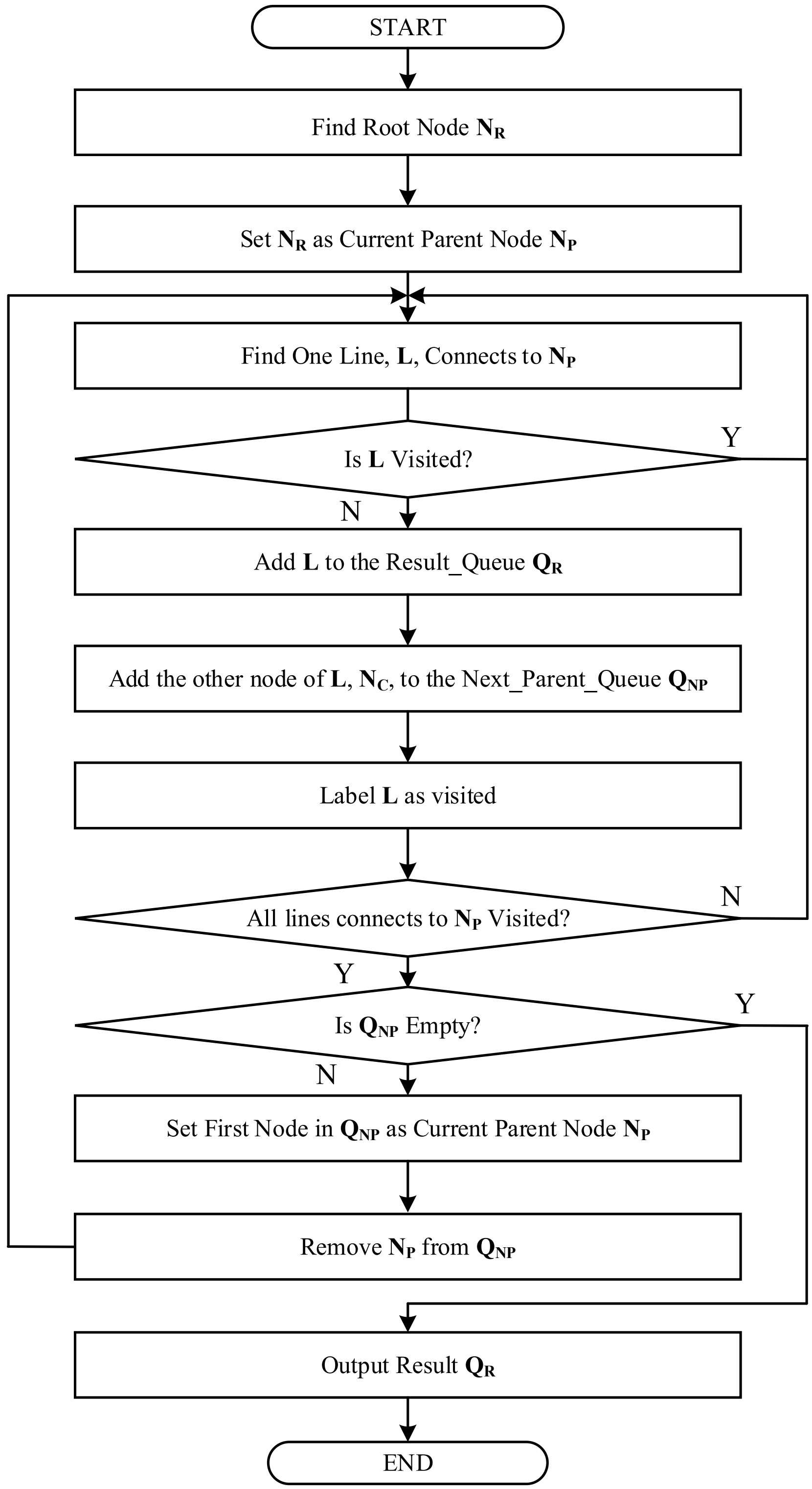

Figure. 11. The Edge-based Breadth-first Search Algorithm Flowchart.

The typical search process can be seen in Figure. 12. The numbers in the small circles indicate the order in which the line is evaluated.

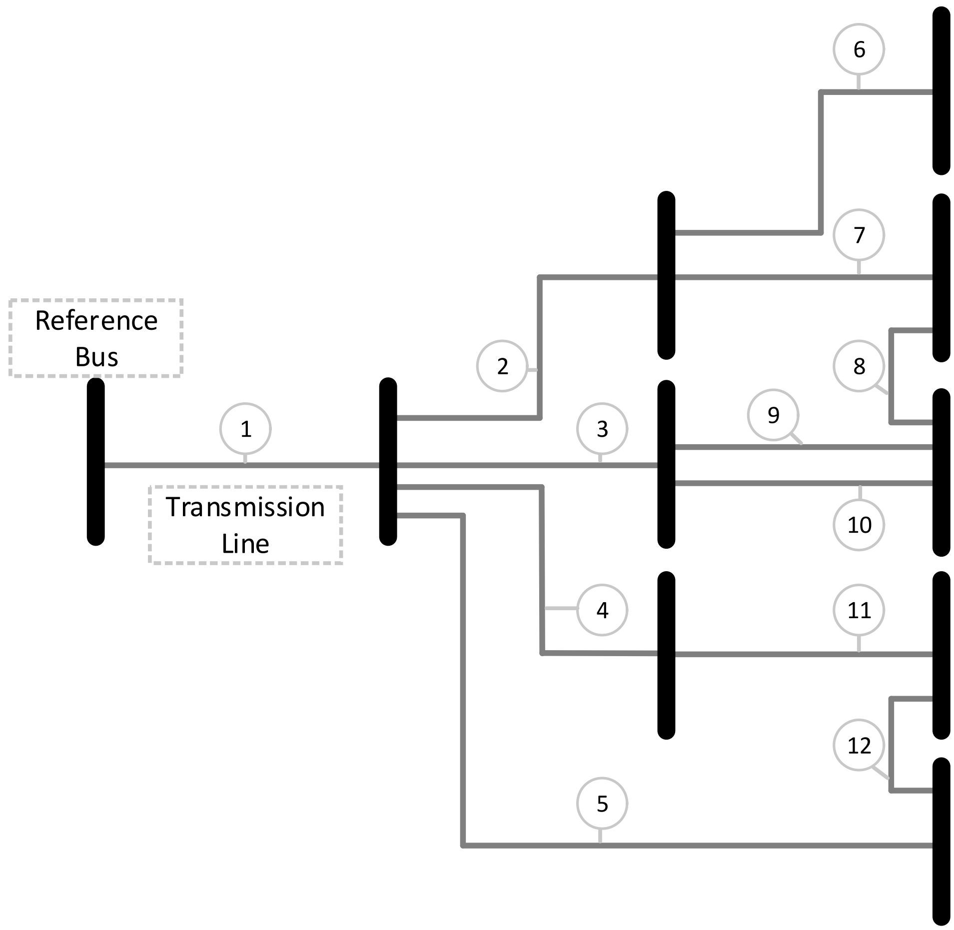

Figure. 12. The Edge-based Breadth-first Search traverse order.

The edge-based BFS can traverse all the concerned transmission lines in the system. When one line errors are found by the algorithm, the correction factors of the “From bus” of a line must have been estimated during the processing of the previous lines. These methods can assure that all the concerned lines will be analyzed. At the same time, the BFS keeps the tree’s height as small as possible so that the accuracy has the slowest decay rate.

The flow chart in Figure. 13 demonstrates the complete system positive sequence parameters estimation process.

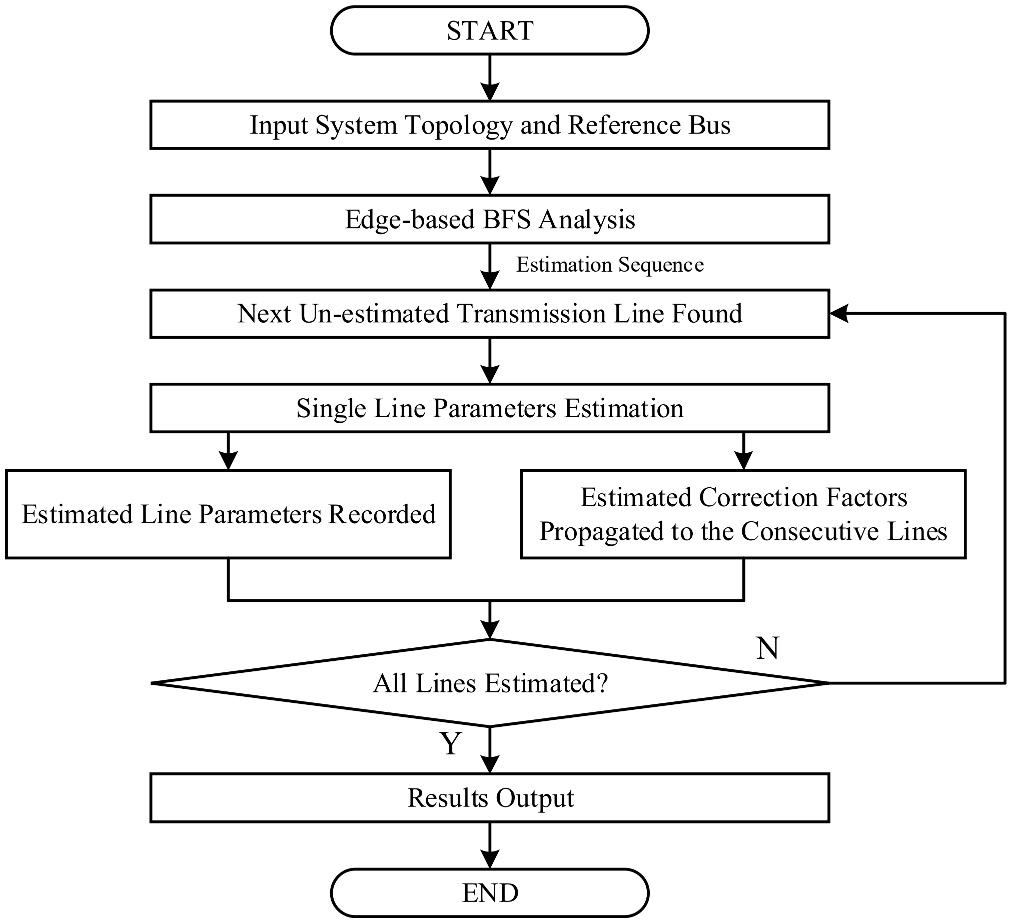

Figure. 13. The complete process of the line parameter estimation.

3.5 Case Study

Two test cases, the IEEE 118-bus system and the Texas 2000-bus system, have been used to validate the proposed methodology. The PMU measurements were generalized based on the aforementioned error model. The ratio errors and the positive sequence parameters of the 345KV lines were estimated based on the generalized data. The estimation errors were then analyzed.

3.5.1 Ieee 118-Bus System

1) System and PMU measurements generation

The IEEE 118-bus system model was used as the study case to validate and demonstrate the effectiveness of the estimation process. The system diagram can be found in Figure. 14. There are two voltage levels in the system: Buses 8, 9, 10, 26, 30, 38, 63, 64, 65, 68, 81 are 345 KV buses (blue buses and lines in the system diagram); The others are 138 KV buses (black buses and lines). The analysis was conducted on the high voltage level (345 KV) buses. Notably, the methodology is also suitable to power systems of other voltage levels given proper information and measurement data.

Based on this system, positive sequence voltages and currents were acquired for all 345kV buses through a series of AC power flow calculations. Even though estimation was only performed on the lines connecting the 345kV buses, the currents injections from lower voltage levels are also collected due to the data requirements of the current accuracy propagation method. All 24 relevant lines can be easily identified through the system diagram. The load curve of the power flows was simulated based on the variation of one summer day morning-load-pick-up hour data of the Dominion Energy Virginia system. The reporting frame rate of simulated PMU is 30 frames/second. Hence, the total number of the time instances is "30×60×60=108,000". According to the sampling strategy stated in section 3.3.2, data selected was from the first second of each minute within an hour (i.e. 1,800 instances).

The data collected from the power flow calculation are treated as the perfect voltages and currents. Without losing generality, Bus 81 was chosen as the reference bus and the line connecting Bus 81 and Bus 68 as the first to be estimated, which means the voltage measurements on Bus 81 and the currents measurements flowing out of Bus 81 towards Bus 68 are the accurate ones. For other voltage and current measurements, the PMU measurement error model derived in section 2.3 was employed to simulate the measurements provided by the local PMUs with ratio errors.

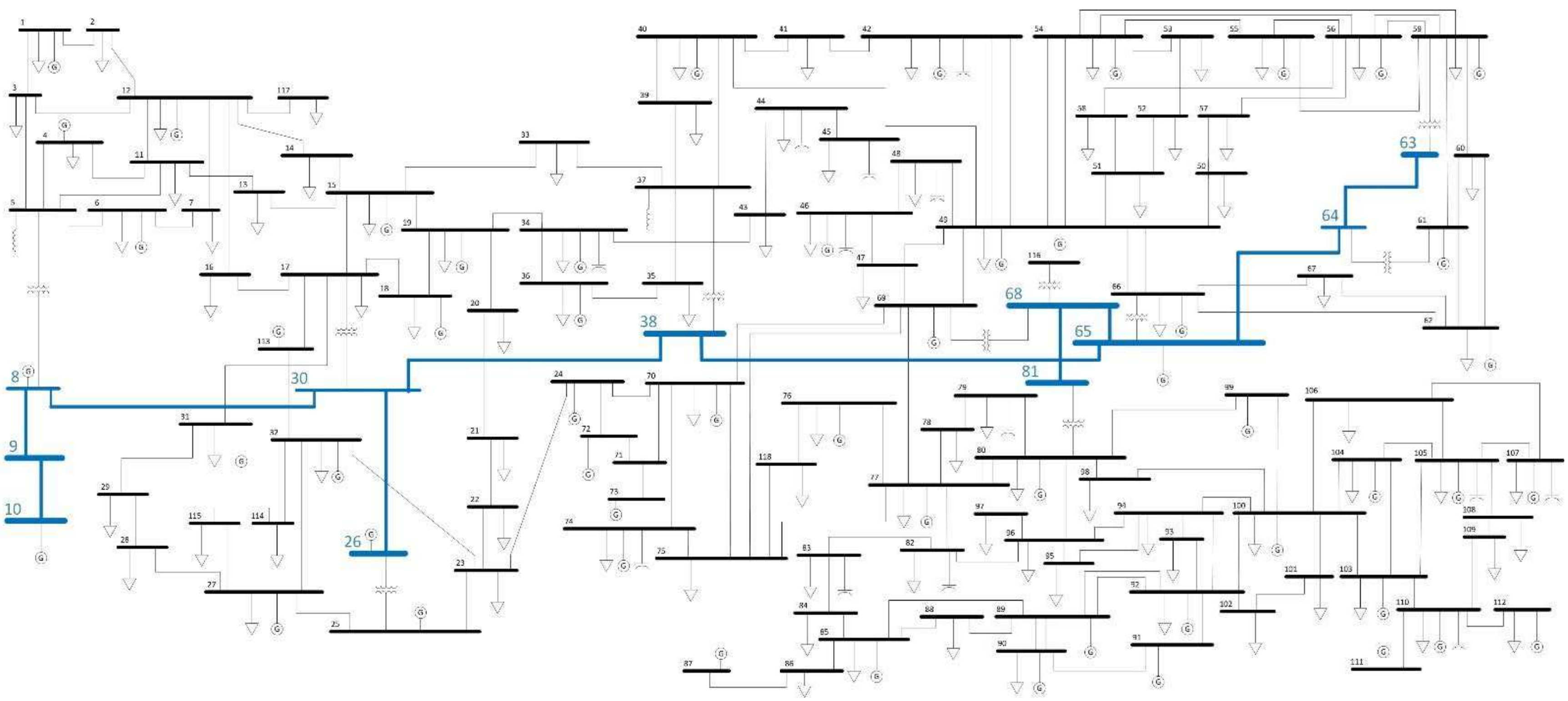

Figure. 14. The IEEE 118-bus system diagram.

For transposed lines, it was assumed that the system remained three-phase balanced over the operation time. The single-phase power flow results were taken as the Phase A data, and data in the other two phases are generated through ±120° phase angle shifts. One single un-transposed line was taken as an example to demonstrate the effectiveness of the estimation algorithm on this circumstance. The three-phase voltages and currents of the reference bus were generated similarly as the transposed case based on the power flow results. However, those of the other bus were calculated using the provided impedance and susceptance matrices[56].

Different ratio errors were then generated randomly for different phases and measurements. However, such ratio errors were invariant during the studied period. The positive sequence ratio errors were thus calculated with (5) and recorded as part of the true values to be estimated. The simulated three-phase measurements are created using the accurate three-phase voltages and currents as well as the generated three-phase ratio errors based on the PMU measurement error model introduced in the previous chapter. The simulated positive sequence measurements were obtained from the processed three-phase data and quantized the voltages by 12 V and the currents by 0.65 A. These generated measurements are used as the input of the estimation procedure.

2) Single line parameters estimation results

For transposed lines, the method developed in section 2.3.1 was used to estimate the parameters of the line connecting Bus 81 and Bus 68. With the knowledge of accurate voltage and current measurements on Bus 81, its correction factors are $KV_1 = 1 + j0$ and $KV_2 = 1 + j0$. The correction factors of the voltage on and the current flowing out of Bus 68, KV_2 and KI_2 are also estimated. The computation results are shown in Table 1.

TABLE 1. SINGLE TRANSPOSED LINE PARAMETERS ESTIMATION RESULTS

			True Value ($\times 10^{-7}$)	Estimated Value ($\times 10^{-7}$)	Error ($\times 10^{-7}$)
Bus 1	81	KV_1	$1\times 10^7 + 0i$	N/A	N/A
		KI_1	$1\times 10^7 + 0i$	N/A	N/A
Bus 2	68	KV_2	10266464.9898 - 19846.0026i	10266465.8004 - 19861.1088i	-0.8106 – 15.1062i
		KI_2	9932573.4041 + 115061.5151i	9931962.5986 + 116872.5726i	610.8055 + 1811.0575i
R (pu)			17500.0044	17510.7698	-10.7654
X (pu)			202000.0090	202001.4563	-1.4473
y (pu)			4040000.1451	4037366.4274	-2633.7177

The estimation results indicate good accuracy. The respective error rates of the correction factors are 7.8956E-06 % for KV_2 real part, 7.6117E-02% for KV_2 imaginary part, 6.1495E-03% for KI_2 real part, and 1.5740% for KI_2 imaginary part. The errors of imaginary parts are larger than that of the corresponding real parts. The main reason is that the absolute values of the imaginary parts of the correction factors are much smaller than the real parts by nature, which is brought by the ratio errors angle limits defined by the standards. This numeric characteristic highly influenced the precision of estimating the imaginary parts. However, based on the same numeric feature, the accuracy of the line parameters estimation is remarkable, which is not interfered by the imaginary parts of the correction factors. The error rate of the resistance, reactance, and susceptance estimation are 6.1517E-02%, 7.1649E-04%, and 6.5191E-02% respectively.

For the un-transposed line, the impedance matrix and the susceptance matrix used to generate three-phase data are as follows:

$$\mathbf{Z}_{abc} = \begin{bmatrix} 8.5922 + 61.0128\text{i} & 4.1208 + 27.6955\text{i} & 4.0940 + 23.9696\text{i} \\ 4.1208 + 27.6955\text{i} & 8.5131 + 61.0865\text{i} & 4.0932 + 27.7693\text{i} \\ 4.0940 + 23.9696\text{i} & 4.0932 + 27.7693\text{i} & 8.4612 + 61.1171\text{i} \end{bmatrix} \tag{3-33}$$

$$\mathbf{y}_{abc} = \begin{bmatrix} 1.0913\text{E-04i} & -1.6076\text{E-05i} & -1.6076\text{E-05i} \\ -1.6076\text{E-05i} & 1.0544\text{E-04i} & -2.4244\text{E-05i} \\ -1.6076\text{E-05i} & -2.4244\text{E-05i} & 1.0544\text{E-04i} \end{bmatrix} \tag{3-34}$$

The estimation results are listed in Table 2.

TABLE 2. SINGLE UN-TRANSPOSED LINE PARAMETERS ESTIMATION RESULTS

Positive Sequence Parameters	True Value	Estimated Value	Error	Error Rate (%)
R(Ω)	4.4195	4.3377	-0.0818	-1.8509
X(Ω)	34.5940	34.7055	0.1115	0.3223
y(S)	1.2547E-04	1.2375E-04	-1.7155E-06	-1.3708

The error rate of the three line parameters is all smaller than 2%. For the most important parameter, the positive sequence line reactance, the error rate is smaller than 0.5%. Even though the overall accuracy of the estimation is lower than the transposed case, due to the unbalance brought by the un-transposed structure, it is still satisfactory. These results clearly demonstrate the validity and effectiveness of the single transmission line parameters estimation method.

3) System lines parameters estimation

Since the estimation accuracy difference between the transposed and un-transposed lines is small, the three-phase balanced system cases are utilized to illustrate the capability of the proposed algorithm for simplicity. Given the effectiveness of the single line parameter estimation algorithm,

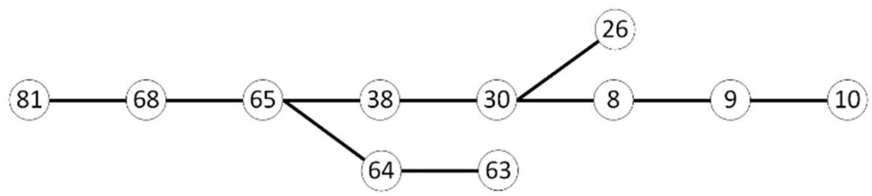

Figure. 15. The 345 KV subsystem diagram.

with the methods mentioned in section 2.3, the estimation process is propagated towards the 345 KV subsystem. The subsystem diagram is shown in Figure. 15. The numbers in circles indicate bus numbers. Propagation order provided by edge-based BFS is from left to right. The reference bus and line remain the same as the single line estimation process.

The estimation results are shown in Table 3. It can be seen that the estimation is generally accurate. Most of the error rates of the estimated line parameters are smaller than or around 1%. However, comparatively larger errors on several lines are also present. The error rate of the resistance and susceptance of the line between Bus 64 and Bus 63 are 12.8980% and 8.6431% respectively.

The possible reasons for this phenomenon include: 1) this line is a shorter transmission line compared with others. The susceptance of this line is far smaller than the other lines, which can cause numerical errors during calculation with (3-17). Because the line impedance is estimated based on the knowledge of susceptance as shown in (3-18), the error of susceptance estimation can be easily passed to the line impedance. 2) this line is comparatively far from the reference bus. Such distance can result in the accumulative effect of the ratio errors, according to the propagation processes. Without the propagation of accurate measurements, the estimation process of this line can be easily influenced. One can also observe around 2% error rates of the estimation of the lines connecting Bus 30 with Bus 26, Bus 8 with Bus 9, and Bus 9 with Bus 10. These larger error rates were likewise brought by the distances from the reference bus. The table is arranged based on the visited order of the lines in the subsystem. A pattern can be summarized indicating the increase of the errors along with the consecutive visits of the lines.

TABLE 3. SYSTEM LINES PARAMETERS ESTIMATION RESULTS

From Bus	KV_1 Error	KI_1 Error	To Bus	KV_2 Error	KI_2 Error	R		X		y	
						Error	Error Rate (%)	Error	Error Rate (%)	Error	Error Rate (%)
81	N/A	N/A	68	-8.1052E-08 -1.5106E-06i	6.1081E-05 -1.8111E-04i	1.08E-06	0.0616	1.44E-07	0.0007	2.63E-04	0.0652
68	1.8552E-07 +9.9730E-07i	-2.5809E-03 2.2055E-02i	65	-1.8756E-06 +4.4313E-07i	-1.2458E-03 +2.1474E-02i	3.55E-06	0.2570	2.59E-05	0.1619	0.00033	0.1027
65	-2.3162E-06 +6.4019E-07i	9.7546E-03 +3.9078E-02i	38	4.3103E-05 -8.7327E-05i	1.2062E-02 +4.1090E-02i	1.39E-04	1.5530	9.95E-04	1.0088	0.00828	1.5832
65	-1.8341E-06 +3.2975E-07i	-1.5036E-02 +2.2295E-02i	64	7.3974E-06 -3.6754E-06i	-1.5872E-02 +2.5203E-02i	1.16E-05	0.4321	4.61E-04	1.5270	0.00088	0.4645
38	4.6445E-05 -8.3559E-05i	1.2282E-02 -4.0879E-02i	30	4.0532E-05 -7.9476E-05i	1.1226E-02 +4.1224E-02i	5.59E-05	1.2041	5.51E-04	1.0204	0.00251	1.1922
64	7.0899E-06 -4.1999E-06i	-1.6471E-02 +2.4791E-02i	63	6.8327E-06 -8.7721E-05i	2.3150E-02 +4.0754E-02i	2.22E-04	12.8980	4.19E-04	2.0957	0.00933	8.6431
30	4.2255E-05 -7.4048E-05i	1.6471E-03 +5.7800E-02i	8	7.6776E-05 +1.0365E-04i	4.8530E-03 +5.7460E-02i	6.33E-05	1.4697	1.54E-04	0.3052	0.00024	0.0948
30	3.8312E-05 -7.5784E-05i	3.2837E-02 +1.5116E-02i	26	1.5661E-04 +1.0000E-05i	3.2773E-02 +1.3359E-02i	3.71E-04	4.6407	2.86E-03	3.3271	0.01675	3.6905
8	7.4647E-05 +1.0822E-04i	2.2547E-02 +7.9627E-03i	9	5.0781E-05 -8.8060E-05i	2.2142E-02 -7.4259E-03i	7.21E-05	2.9545	7.08E-04	2.2314	0.01436	2.4729
19	5.1020E-05 -8.9386E-05i	2.2917E-02 -6.3834E-03i	10	4.4876E-05 -1.0376E-04i	2.3270E-02 -6.0184E-03i	4.88E-05	1.8929	7.59E-04	2.3561	0.01551	2.5224

3.5.2 Texas 2000-Bus System

The Texas 2000-bus system, available in [57] contains 2007 buses and 2481 lines with three voltage levels: 13.8KV, 115KV, and 345KV. The 345KV subsystem is composed of 224 buses and interconnected by 335 transmission lines. The voltage and current data were generalized in the same manner as described in section 3.5.1. Only one bus was selected as the reference bus and equipped with accurate voltage and current data.

The estimation results using the three-phase balanced data are shown in the following figures. For the reactances estimation results are shown in Figure. 16, most of the lines' error rates are within [-4%, 2%] and the largest does not exceed -7%. For the susceptances, Figure. 17, most of the lines' error rates lay in the range of [-5%, 5%].

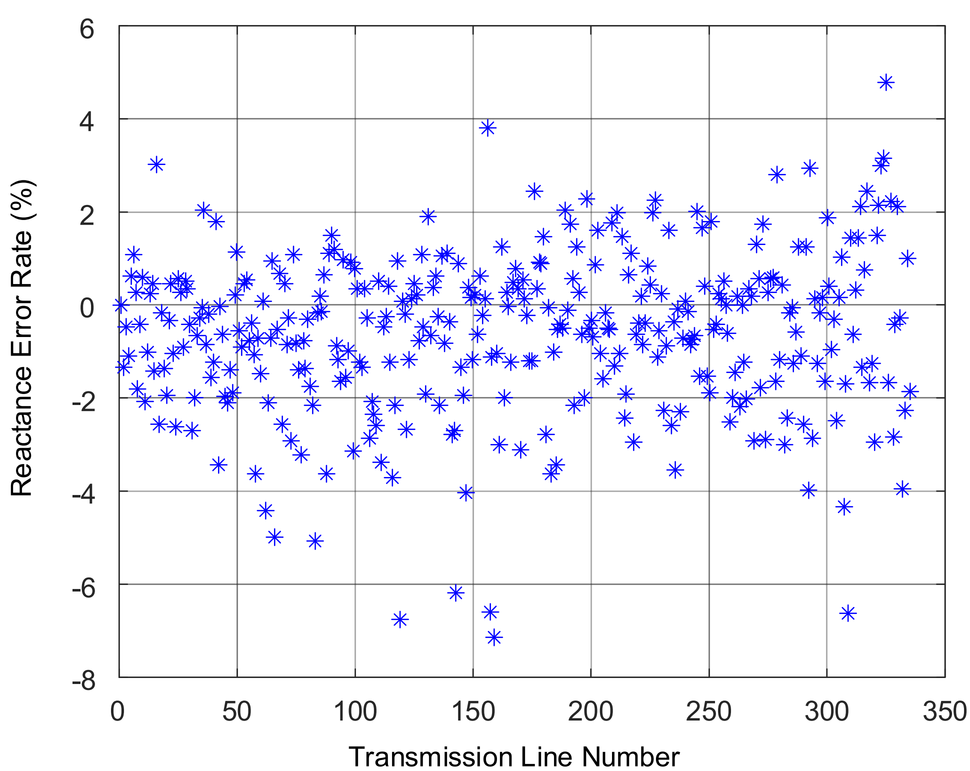

Figure. 16. Estimation error rate of reactances in Texas 2000-bus system.

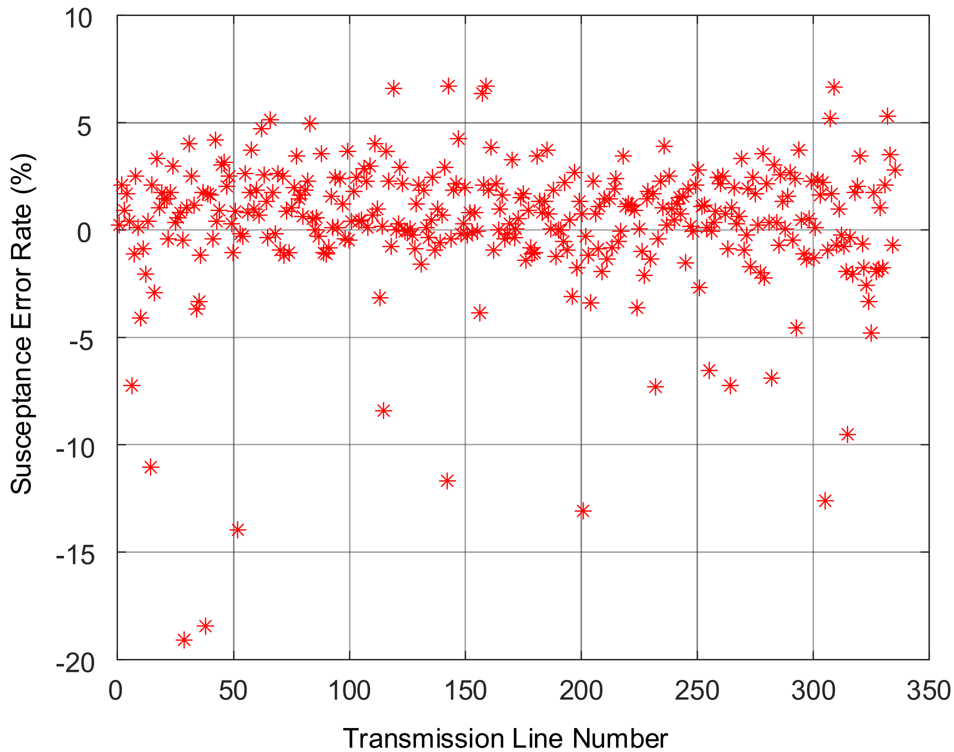

Figure. 17. Estimation error rate of susceptances in Texas 2000-bus system.

However, there do exist several cases where the error rates are larger than 10%. The comparison is made between the lines with larger error rates and the whole group of the lines. The box plots[58] are shown in Figure. 18. The left box plot shows the distribution of the susceptances of lines with more than 5% estimation error rates. The right one demonstrates the distribution of all the 335 susceptances within the concerned 345KV subsystem. As one can see in the figure, the lines with larger estimation errors generally are far smaller than the other lines. This confirms the reason described in section 2.4.1 that shorter transmission lines with smaller parameters might influence the estimation accuracy.

The possible solution to the comparatively large errors can be obtained by integrating more reference measurements into the system. Especially for those short transmission lines that have significantly small parameters, installation of the revenue CTs and PTs will effectively relieve

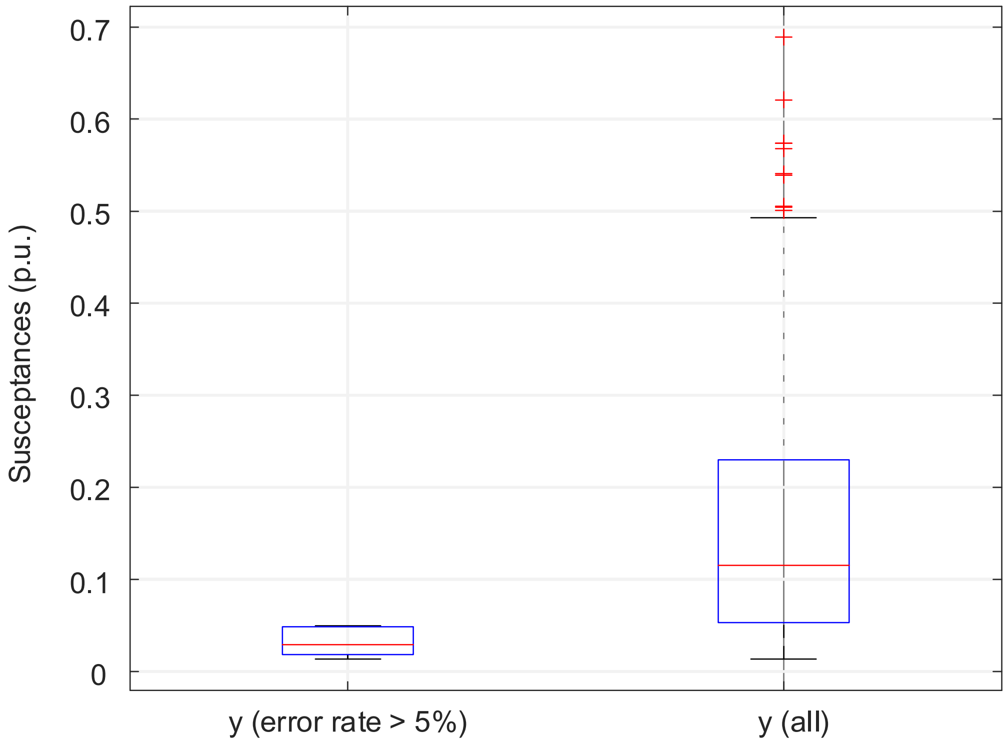

Figure. 18. Comparison of the distribution of lines susceptances in Texas 2000-bus system.

them of the cumulative errors propagated from former lines and provide more accurate initial data for estimation. Nonetheless, the installation will also increase the economic cost.

Although the estimation results of several parameters are comparatively large, most of the error rates are limited to within 3%. This level of the accuracy demonstrates that the system lines parameters estimation methodology is valid and effective for most cases. At the same time, the requirements of the algorithm are not customized. With proper measurements and system topology information, the method is applicable to any other balanced power systems.

3.6 Discussions

In this chapter, a methodology is proposed to estimate the transposed/un-transposed transmission line positive sequence parameters of a power system based on a PMU measurement error model. With the reference bus selected, Least Squares Estimation is utilized to estimate the line resistance, reactance, and susceptance, as well as to calibrate the measuring devices, CTs and PTs, installed on one single transmission line. The accuracy is then propagated to the whole system with Edge-based Breadth-first search and quadratic optimization algorithms.

Both the single transmission line and the system lines parameters estimation are verified through the IEEE 118-bus standard system and the algorithm was also utilized to larger scale Texas 2000-bus system. The results show satisfactory accuracy. Most of the estimation errors are around 1%, and very few of them are comparatively large. The possible reasons are also proposed and analyzed. The estimation conducted on short transmission lines with exceptional small parameters needs further investigation. However, the methodology proposed is effective and almost based entirely on the software which can save utilities much field work efforts. Extension to other systems is also easy with sufficient PMU measurements and system topology information. Given the positive sequence data acquisition reality during common utilities' operation, this method can satisfy most utilities' requirements and therefore can be widely deployed.

CHAPTER 4. LVRT CONSTRAINED TRANSIENT STABILITY ASSESSMENT WITH LYAPUNOV FUNCTIONS FAMILY

4.1 Introduction

Renewable generations (RG) can no longer be taken as a deterministic injection as it brings a level of uncertainty to the system operation [59]. One of the recent significant challenges faced by systems with large RG penetration is that RGs are made to trip offline during system disturbances in order to stop feeding in an islanding situation. A major issue is that the trip logic is based on local measurements of voltage and frequency at the point of interconnection which may not truly observe the islanding event. This means that there are significant chances of loss of this generation during non-islanding situations. Accordingly, the system should be constrained to operate in the region in state space referred to as the feasibility region (FR) in order to minimize these undesirable events. This makes the power system a constrained non-linear dynamical system.

Conventional direct methods for system transient stability assessment (TSA) aim at estimating the whole or relevant portion of the stability region of a power system. The purpose is to capture instability phenomenon like loss of synchronism, voltage collapse, etc [60] [61] which is characterized by the fault on trajectory exiting the stability region of the post-fault stable equilibrium point (SEP). However, due to the tripping of RGs resulting from breaking operation limits like LVRT constraint violation, the system is under a serious threat of collapse. Therefore, the phenomenon of a post-fault trajectory exiting the FR should also be captured by these approaches. However, traditional direct methods are not designed to deal with such systems.

The stability region (SR) characterization for constrained dynamical systems was introduced in [62]. Mishra et.al. proposed using the sum of squares programming [31] to estimate this region for direct stability assessment of power systems under low voltage ride through constraints. However, this approach faces serious computational limitations and therefore not scalable to large systems. Alberto et.al [63] proposed using Potential Energy Boundary Surface (PEBS) method for TSA of such LVRT constrained systems which is known to have reliability concerns when used for multi-machine systems [64]. Turitsyn et.al [65] proposed an approach that uses a family of Lyapunov functions sharing the same structure as the energy function to get a decent estimate of the stability region. This approach is scalable to large systems. This section will be exploiting this approach along with advances in convex optimization for estimating the stability region considering constraints owing to the LVRT curves which is referred to as the LVRT constrained stability region (CSR).

4.2 System State Space Model For Transient Stability Assessment

Generally, most of the TSA methods take a deferential-algebra equations (DAEs) model [26] to express the electro-mechanical behaviors of the power system which is called the system state space model and has the following form.

$$\begin{cases} \dot{\mathbf{x}} = f(\mathbf{x},\ \mathbf{y}), & f : \mathbf{R}^{n+m} \to \mathbf{R}^{n} \\ 0 = g(\mathbf{x},\ \mathbf{y}), & g : \mathbf{R}^{n+m} \to \mathbf{R}^{m} \end{cases} \tag{4-1}$$

where $\mathbf{x} \in \mathbf{R}^{n}$ represents the vector of dynamic states and $\mathbf{y} \in \mathbf{R}^{m}$ represents the vector of algebraic variables.

The system state space model is based on the states of the power system, which is composed of generators phase angles, δ, and corresponding angular speeds, ω or $\dot{\delta}$. Therefore, in order to construct the model, the first step is to reduce the normal system model built upon branches and buses to find the relationship between generators which mainly reflects the transient happens in the system. Kron reduction is used here to help build up the system state space model so that all the variables relevant to load are substituted by those relevant to generators.

4.2.1 Algebraic Equations Based on Kron-reduction

The algebraic equations generally refer to the power flow equations of the concerned system which functions similarly with equality constraints [26]. However, the normal power flow equations mainly concern with load buses and generator bus interfaces. The dynamic states in the DAE system are only concerned with generators. So there is a need to use Kron-reduction method [66] to reduce the original power flow equations to the internal node model which only considers generators states as arguments. The most fundamental relationship represented by the power flow equations can be traced back to voltage and current relationships using system admittance matrix $\mathbf{Y}_{Bus}$ as a medium, which can be shown as follows:

$$\mathbf{I}_{N\times 1} = \mathbf{Y}_{Bus}\mathbf{V}_{N\times 1} \tag{4-2}$$

where,

$$\mathbf{Y}_{Bus} = \begin{array}{cc} \overbrace{\begin{array}{cc} n & N-n \end{array}} & \\ \begin{bmatrix} \mathbf{Y}_1 & \mathbf{Y}_2 \\ \mathbf{Y}_3 & \mathbf{Y}_4 \end{bmatrix} & \begin{array}{l} n \\ N-n \end{array} \end{array} \tag{4-3}$$

n is the number of generator buses, N is the number of all buses; $\mathbf{I}_{N\times 1}$ indicates the vector of current injections in the buses; $\mathbf{V}_{N\times 1}$ indicates the vector of voltages on the buses. It can be easily seen that the equation set is arranged so that generator interfacing buses are listed firstly. With estimated line parameters in the previous chapter, a more accurate system model, or admittance matrix, is available for real-world implementation of this TSA method.

For each generator in the system, the internal node can be shown as in Figure. 19. Here E is the generator terminal voltage magnitude; δ is the generator rotor angle; x'_d is the transient reactance; $V\angle\alpha$ is the bus voltage.

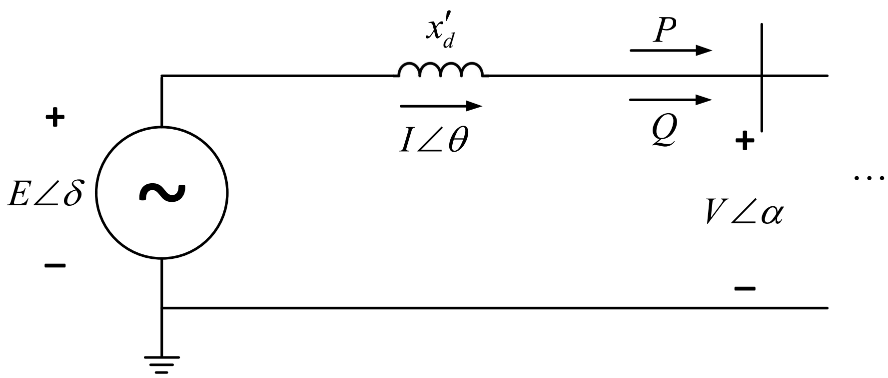

Figure. 19. Relationship between generator terminal voltage and bus voltage.

Taking the generator reactances and transferring loads into line impedances, we have the reduced model admittance matrix:

$$\hat{\mathbf{Y}}_{Bus} = \begin{array}{c} \overbrace{\begin{matrix} \quad n \quad & \quad n \quad & \quad N-n \quad \end{matrix}} \\ \begin{bmatrix} \mathbf{y}_g & -\mathbf{y}_g & \mathbf{0} \\ -\mathbf{y}_g & \mathbf{y}_g + \mathbf{Y}_1 + \mathbf{y}_{lg} & \mathbf{Y}_2 \\ \mathbf{0} & \mathbf{Y}_3 & \mathbf{Y}_4 + \mathbf{y}_{ll} \end{bmatrix} \end{array} \begin{array}{l} \\ n \\ n \\ N-n \end{array} \tag{4-4}$$

where,

$$\mathbf{y}_g = \begin{bmatrix} 1/jx'_{d1} & & \underline{0} \\ & \ddots & \\ \underline{0} & & 1/jx'_{dn} \end{bmatrix}_{n\times n} \tag{4-5}$$

which indicates admittances created by generators transient reactances that connect the internal nodes and their system interface buses;

$$\mathbf{y}_{lg} = \begin{bmatrix} y_{lg,1} & & \underline{0} \\ & \ddots & \\ \underline{0} & & y_{lg,n} \end{bmatrix}_{n\times n} \tag{4-6}$$

and

$$y_{lg,i} = \frac{P_{L,i} - jQ_{L,i}}{\left|v_i\right|^2} \tag{4-7}$$

which are the equivalent admittance of the loads on the generator buses, $P_{L,i}$ and $Q_{L,i}$ refers to the active and reactive load on bus i, and v_i refers to the voltage on bus i;

$$\mathbf{y}_{ll} = \begin{bmatrix} y_{ll,n+1} & & \underline{0} \\ & \ddots & \\ \underline{0} & & y_{ll,N} \end{bmatrix}_{(N-n)\times(N-n)} \tag{4-8}$$

$$y_{ll,j} = \frac{P_{L,j} - jQ_{L,j}}{\left|v_j\right|^2} \tag{4-9}$$

which are the equivalent impedances of the load on pure load buses.

Then we have the following equation set:

$$\begin{bmatrix} \mathbf{I}_g \\ \mathbf{0} \end{bmatrix} = \begin{bmatrix} \mathbf{y}_g & \mathbf{Y}_{12} \\ \mathbf{Y}_{21} & \mathbf{Y}_{bus}^{new} \end{bmatrix} \begin{bmatrix} \mathbf{E} \\ \mathbf{V} \end{bmatrix} \tag{4-10}$$

where

$$\mathbf{Y}_{bus}^{new} = \begin{bmatrix} \mathbf{y}_g + \mathbf{Y}_1 + \mathbf{y}_{lg} & \mathbf{Y}_2 \\ \mathbf{Y}_3 & \mathbf{y}_{ll} \end{bmatrix}_{N\times N} \tag{4-11}$$

and $\mathbf{E}$ is the generator terminal voltage vector, $\mathbf{I}_g$ is the vector of currents flowing out of the generator terminals; $\mathbf{V}$ refers to the vector of voltages on original buses in the system.

Based on (4-10) we have

$$\mathbf{V} = -\left(\mathbf{Y}_{bus}^{new}\right)^{-1} \mathbf{Y}_{21}\mathbf{E} \tag{4-12}$$

$$\begin{aligned} \mathbf{I}_g &= \mathbf{y}_g\mathbf{E} + \mathbf{Y}_{12}\mathbf{V} \\ &= \left[\mathbf{y}_g - \mathbf{Y}_{12}\left(\mathbf{Y}_{bus}^{new}\right)^{-1}\mathbf{Y}_{21}\right]\mathbf{E} \end{aligned} \tag{4-13}$$

4.2.2 Differential Equations

The differential part is mainly concerned with synchronous generators' swing equations which indicate the relationship between generator electric power output and mechanical power input.

The conventional generator swing equation for the kth generator is shown as following:

$$m_k \ddot{\delta}_k + d_k \dot{\delta}_k + \sum_j B_{kj} E_k E_j \sin\left(\delta_k - \delta_j\right) - P_k = 0 \tag{4-14}$$

where, m_k is the inertia constant; δ_k is the rotor angle which is part of the dynamic states to be considered; d_k is the damping coefficient; B_{kj} is the entry in the Kron-reduced model conductance matrix; E_k is the generator terminal voltage; P_k is the mechanical power input into the generator.

Equilibrium point, $\begin{bmatrix}\delta_1^* & \cdots & \delta_n^* & 0 & \cdots & 0\end{bmatrix}^{\mathrm{T}}$, is reached by solving the following equation set:

$$\sum_j B_{kj} E_k E_j \sin\left(\delta_k^* - \delta_j^*\right) = P_k \tag{4-15}$$

The left-hand side of the equation refers to the electric power. This equality represents the balance between mechanical input power and the electric output power.

For the convenience for future direct methods calculation, the SEP is shifted to 0. Therefore, without losing generality, take the system states as the deviation from the SEP as following

$$\mathbf{x} = \left[\mathbf{x}_1 , \quad \mathbf{x}_2\right]^{\mathrm{T}} \tag{4-16}$$

where,

$$\mathbf{x}_1 = \begin{bmatrix}\delta_1 - \delta_1^* & \delta_2 - \delta_2^* & \cdots & \delta_n - \delta_n^*\end{bmatrix}^{\mathrm{T}} \tag{4-17}$$

$$\mathbf{x_2} = \left[\dot{\delta}_1 - 0 \quad \dot{\delta}_2 - 0 \quad \cdots \quad \dot{\delta}_n - 0\right]^{\mathrm{T}} = \left[\dot{\delta}_1 \quad \dot{\delta}_2 \quad \cdots \quad \dot{\delta}_n\right]^{\mathrm{T}} \tag{4-18}$$

Separating the linear and non-linear parts, the dynamic system model can be expressed in the state space as follows:

$$\dot{\mathbf{x}} = \mathbf{A}\mathbf{x} - \mathbf{B}F\left(\mathbf{C}\mathbf{x}\right) \tag{4-19}$$

where,

$$\mathbf{A} = \begin{bmatrix} \mathbf{O}_{n\times n} & \mathbf{I}_{n\times n} \\ \mathbf{O}_{n\times n} & -\mathbf{M}^{-1}\mathbf{D} \end{bmatrix} \tag{4-20}$$

$$\mathbf{M} = \begin{bmatrix} m_1 & & 0 \\ & \ddots & \\ 0 & & m_n \end{bmatrix} \tag{4-21}$$

$$\mathbf{D} = \begin{bmatrix} d_1 & & 0 \\ & \ddots & \\ 0 & & d_n \end{bmatrix} \tag{4-22}$$

$$\mathbf{B} = \begin{bmatrix} \mathbf{O}_{n\times|\boldsymbol{\varepsilon}|} \\ \mathbf{M}^{-1}\mathbf{E}_B^{\mathrm{T}} \end{bmatrix} \tag{4-23}$$

$$\mathbf{C} = \begin{bmatrix} \mathbf{E} & \mathbf{O}_{|\boldsymbol{\varepsilon}|\times n} \end{bmatrix} \tag{4-24}$$

$$\mathbf{F} = F\left(\mathbf{C}\mathbf{x}\right) = \left[\left(\sin\delta_{kj} - \sin\delta_{kj}^{*}\right)_{\{k,j\}\in\boldsymbol{\varepsilon}}\right]^{\mathrm{T}} \tag{4-25}$$

where, $\boldsymbol{\varepsilon}$ is the set of branches including all the possible combinations of the internal node pairs which are corresponding to the non-diagonal entries of the admittance matrix of the Kron-reduced internal node model, for example, for the three-generator system, $\boldsymbol{\varepsilon}$ should be [1-2, 1-3, 2-1, 2-3, 3-1, 3-2], and

$$\mathbf{E}\begin{bmatrix}\delta_1 & \delta_2 & \cdots & \delta_n\end{bmatrix}^{\mathrm{T}} = i^{th}\, branch \begin{bmatrix} \vdots \\ \delta_{kj} - \delta_{kj}^{*} \\ \vdots \end{bmatrix}_{|\boldsymbol{\varepsilon}|\times 1} \tag{4-26}$$

$$\mathbf{E}_B = i^{th}\, branch \begin{array}{c} \begin{array}{ccccc} & k & & j & \end{array} \\ \begin{bmatrix} & & \vdots & & \\ 0\cdots0 & B_{kj}E_kE_j & 0\cdots0 & -B_{kj}E_kE_j & 0\cdots0 \\ & & \vdots & & \end{bmatrix}_{|\boldsymbol{\varepsilon}|\times n} \end{array} \tag{4-27}$$

So that we have

$$\mathbf{BF} = \begin{bmatrix} \mathbf{O}_{n\times|\boldsymbol{\varepsilon}|} \\ \mathbf{M}^{-1}\mathbf{E}_B^{\mathrm{T}} \end{bmatrix} \mathbf{F}_{|\boldsymbol{\varepsilon}|\times 1} = \begin{bmatrix} \mathbf{O}_{n\times 1} \\ \mathbf{M}^{-1}\mathbf{E}_B^{\mathrm{T}}\mathbf{F}_{|\boldsymbol{\varepsilon}|\times 1} \end{bmatrix} \tag{4-28}$$

where,

$$\mathbf{M}^{-1}\mathbf{E}_B^{\mathrm{T}}\mathbf{F}_{|\boldsymbol{\varepsilon}|\times 1} = \begin{bmatrix} \vdots \\ \dfrac{1}{m_k}\left[B_{kj}E_kE_j\left(\sin\delta_{kj} - \sin\delta_{kj}^{*}\right) + \cdots\right] \\ \vdots \\ \dfrac{1}{m_j}\left[\left(-B_{kj}E_kE_j\right)\left(\sin\delta_{kj} - \sin\delta_{kj}^{*}\right) + \cdots\right] \\ \vdots \end{bmatrix} = \begin{bmatrix} \vdots \\ \dfrac{1}{m_k}\left[B_{kj}E_kE_j\left(\sin\delta_{kj} - \sin\delta_{kj}^{*}\right) + \cdots\right] \\ \vdots \\ \dfrac{1}{m_j}\left[B_{jk}E_jE_k\left(\sin\delta_{jk} - \sin\delta_{jk}^{*}\right) + \cdots\right] \\ \vdots \end{bmatrix}$$

(4-29)

4.3 Direct Methods For Power System Transient Stability Assessment

Direct methods for power system TSA is an efficient way which bypasses the long simulation time for the system trajectories after various faults. The typical direct method or referred to as the Lyapunov's second method can be summarized as following [67]:

For a system like (4-1) having an equilibrium point at $\mathbf{x} = 0$, if there exists an energy function (Lyapunov function), $V(\mathbf{x}) : \mathbf{R}^n \to \mathbf{R}$, such that

- $V\left(\mathbf{x}\right) = 0$, iff $\mathbf{x} = \mathbf{0}$
- $V\left(\mathbf{x}\right) > 0$, iff $\mathbf{x} \neq \mathbf{0}$
- $\dot{V}\left(\mathbf{x}\right) = \frac{d}{dt}V\left(\mathbf{x}\right) = \sum_i \frac{\partial V\left(\mathbf{x}\right)}{\partial x_i} f_i\left(\mathbf{x}\right) \leq 0$, iff $\mathbf{x} \neq \mathbf{0}$

then, $V\left(\mathbf{x}\right)$ is called a candidate Lyapunov function and the system is stable. More intuitively the energy of the system is analogized by the Lyapunov function. If, by nature, the energy of the system can only decrease or not increase before reaching the equilibrium point, the system can be taken as stable.

Based on this theory, if one would like to find the stability of a power system after suffering from a disturbance, he can try to find a proper energy function. If substituting the post-fault system states into this Lyapunov function can satisfy the aforementioned conditions, it can be concluded that the stability of this particular system post-fault state is certified and this point in the state space is inside the system stability region.

However, it is usually difficult to find a suitable Lyapunov function for the studied system. For power systems TSA, the conventional energy function is widely used, which is shown in (4-30).

$$E = \sum_k \frac{m_k \dot{\delta}_k^2}{2} - \sum_{\{k,j\}\in\varepsilon} B_{kj} E_k E_j \cos\delta_{kj} - \sum_k P_k \delta_k \tag{4-30}$$

In [65], researchers proposed a method to find a family of Lyapunov functions using linear matrix inequalities (LMIs), using their properties to provide less conservative stability region assessments. This method will be taken as a basis here to integrate renewable energy LVRT constraints.

4.3.1 Lyapunov Function Family In Center Of Angle Frame

Imitating the conventional energy function, a family of Lyapunov functions can be formulated as follows:

$$V_l(\mathbf{x}) = \frac{1}{2}\mathbf{x}^{\mathrm{T}}\mathbf{Q}_l\mathbf{x} - \sum_{\{k,j\}\in\varepsilon} K_{\{k,j\},l}\left(\cos\delta_{kj} + \delta_{kj}\sin\delta_{kj}^{*}\right), \quad l \in \{Lyapunov\ Functions\ Family\} \tag{4-31}$$

where, matrices $\mathbf{Q}_l$ and $\mathbf{K}_l$ forms a pair of coefficient matrices which characterize the specific Lyapunov function; $\mathbf{Q}_l$ is symmetric positive definite; $\mathbf{K}_l$ is diagonal positive definite. Since the energy function as (4-30) also belongs to this family, it can serve as a good example where $\mathbf{Q}$ is the inertia constants matrix and $K_{\{k,j\}} = B_{kj}E_kE_j$ is one of the diagonal entry in $\mathbf{K}$ which corresponds to the branch between bus k and bus j.

Until now, the problem is discussed under the absolute angle frame. A major issue with analyzing the power system model in absolute angles is that the vector field is a function of differences of angles which means if $(\delta^{*}, 0)$ is an equilibrium point, so is $(\delta^{*} + \text{constant}, 0)$. This yields a single dimensional boundary-less manifold of equilibrium points having the exact same characteristics. From the power systems point of view, all of these points result in the same operating conditions which are effectively defined in terms of power flows. This means that the SR needs to be estimated for a boundary-less surface of desired SEPs instead of a single one. Furthermore, using a Lyapunov function in which the angle terms are defined not just in angle differences as done in [65] will have a level set having a closure and therefore unable to contain that whole surface of desirable SEPs. Thus, a formulation of the LFF approach in the widely known center of angle (COA) reference frame [68] is proposed here.

The COA reference is defined as the mean of angles or angular velocities weighted by respective generators' inertia constants:

$$\begin{cases} \delta_{\mathrm{COA}} = \sum_i m_i \delta_i \Big/ M_t \\ \omega_{\mathrm{COA}} = \dot{\delta}_{\mathrm{COA}} = \sum_i m_i \dot{\delta}_i \Big/ M_t = \sum_i m_i \omega_i \Big/ M_t \\ M_t = \sum_j m_j \end{cases} \tag{4-32}$$

where, δ_{COA} refers to the COA reference rotor angle and ω_{COA} refers to the COA reference angular velocity.

Shifting the absolute angles and angular velocities to the COA reference space, the system states are as shown in (4-33). Here, states of the generator i are taken as an example.

$$\begin{cases} \tilde{\delta}_i = \delta_i - \delta_{\mathrm{COA}} \\ \tilde{\omega}_i = \omega_i - \omega_{\mathrm{COA}} \end{cases} \tag{4-33}$$

where $\tilde{\delta}_i$ refers to the rotor angle in the COA reference frame and $\tilde{\omega}_i$ refers to the angular velocity in the COA reference frame.

The system state model is thus transferred as follows. The two equations (c) and (d) serves as equality constraints brought by the COA frame transformation.

$$\begin{cases} \dot{\tilde{\delta}}_i = \tilde{\omega}_i & (\mathrm{a}) \\ m_i \dot{\tilde{\omega}}_i = m_i \dot{\omega}_i - m_i \dot{\omega}_{\mathrm{COA}} & (\mathrm{b}) \\ \sum_i m_i \tilde{\delta}_i = \sum_i m_i \delta_i - \dfrac{M_t}{M_t} \sum_i m_i \delta_i = 0 & (\mathrm{c}) \\ \sum_i m_i \tilde{\omega}_i = \sum_i m_i \omega_i - \dfrac{M_t}{M_t} \sum_i m_i \omega_i = 0 & (\mathrm{d}) \end{cases} \tag{4-34}$$

Substitute more detailed power relationship into the second equation, we have

$$m_i\dot{\tilde{\omega}}_i = m_i\dot{\omega}_i - m_i\dot{\omega}_{\mathrm{COA}} = P_{m,i} - P_{e,i} - d_i\omega_i - \frac{m_i}{M_t}\sum_k m_k\dot{\omega}_k$$
$$= \left(P_{m,i} - \frac{m_i}{M_t}\sum_k P_{m,k}\right) - \left(P_{e,i} - \frac{m_i}{M_t}\sum_k P_{e,k}\right) - \left(d_i\omega_i - \frac{m_i}{M_t}\sum_k d_k\omega_k\right) \quad (4\text{-}35)$$

where, $P_{m,i}$ refers to the mechanical power input into generator i; $P_{e,i}$ refers to the electric power output from generator i.

Similarly, shifting the SEP to 0, namely, taking the deviation from the actual SEP as the system states, we have

$$\begin{cases} \Delta\tilde{\delta}_i = \tilde{\delta}_i - \tilde{\delta}_i^* \\ \Delta\tilde{\omega}_i = \tilde{\omega}_i - \tilde{\omega}_i^* = \tilde{\omega}_i \end{cases} \quad (4\text{-}36)$$

where, $\tilde{\delta}_i^*$ and $\tilde{\omega}_i^*$ are the states of the SEP in COA frame.

Therefore the new states in the COA frame can be summarized as shown in (4-37).

$$\tilde{\mathbf{x}} = \begin{bmatrix} \Delta\tilde{\delta}_1 & \cdots & \Delta\tilde{\delta}_n & \Delta\tilde{\omega}_1 & \cdots & \Delta\tilde{\omega}_n \end{bmatrix}^{\mathrm{T}} \quad (4\text{-}37)$$

Further, the equation (4-34) is derived to be

$$\begin{cases} \Delta\dot{\tilde{\delta}}_i = \Delta\tilde{\omega}_i \\ m_i\Delta\dot{\tilde{\omega}}_i = \left(P_{m,i} - P_{m,i}^* - \frac{m_i}{M_t}\sum_k\left(P_{m,k} - P_{m,k}^*\right)\right) - \left(P_{e,i} - P_{e,i}^* - \frac{m_i}{M_t}\sum_k\left(P_{e,k} - P_{e,k}^*\right)\right) - \left(d_i\omega_i - \frac{m_i}{M_t}\sum_k d_k\omega_k\right) \\ \sum_i m_i\Delta\tilde{\delta}_i = 0 \\ \sum_i m_i\Delta\tilde{\omega}_i = 0 \end{cases}$$

(4-38)

Mechanical power is assumed to be constant.

$$\begin{cases} \Delta\dot{\tilde{\delta}}_i = \Delta\tilde{\omega}_i \\ m_i\Delta\dot{\tilde{\omega}}_i = -\left(P_{e,i} - P_{e,i}^* - \frac{m_i}{M_t}\sum_k\left(P_{e,k} - P_{e,k}^*\right)\right) - \left(d_i\omega_i - \frac{m_i}{M_t}\sum_k d_k\omega_k\right) \\ \sum_i m_i\Delta\tilde{\delta}_i = 0 \\ \sum_i m_i\Delta\tilde{\omega}_i = 0 \end{cases} \tag{4-39}$$

To be more specific,

$$\begin{aligned} m_i\Delta\dot{\tilde{\omega}}_i &= -\left(P_{e,i} - P_{e,i}^* - \frac{m_i}{M_t}\sum_k\left(P_{e,k} - P_{e,k}^*\right)\right) - \left(d_i\omega_i - \frac{m_i}{M_t}\sum_k d_k\omega_k\right) \\ &= \frac{m_i}{M_t}\sum_k\left(\sum_j B_{kj}E_kE_j\left(\sin\tilde{\delta}_{kj} - \sin\tilde{\delta}_{kj}^*\right)\right) - \sum_j B_{ij}E_iE_j\left(\sin\tilde{\delta}_{ij} - \sin\tilde{\delta}_{ij}^*\right) - \left(d_i\omega_i - \frac{m_i}{M_t}\sum_k d_k\omega_k\right) \end{aligned} \tag{4-40}$$

where, $\tilde{\delta}_{kj} = \tilde{\delta}_k - \tilde{\delta}_j$. Similarly to (4-25), set $\mathbf{F} = F\left(\mathbf{C}\tilde{\mathbf{x}}\right) = \left[\left(\sin\tilde{\delta}_{kj} - \sin\tilde{\delta}_{kj}^*\right)_{\{k,j\}\in\boldsymbol{\varepsilon}}\right]^{\mathrm{T}}$.

Take

$$\gamma_i = \frac{1}{M_t}\sum_k\left(\sum_j B_{kj}E_kE_j\left(\sin\tilde{\delta}_{kj} - \sin\tilde{\delta}_{kj}^*\right)\right) - \frac{1}{m_i}\sum_j B_{ij}E_iE_j\left(\sin\tilde{\delta}_{ij} - \sin\tilde{\delta}_{ij}^*\right) \tag{4-41}$$

In matrix form,

$$\begin{bmatrix} \vdots \\ \gamma_i \\ \vdots \end{bmatrix} = \left(\boldsymbol{\gamma}^{(1)} + \boldsymbol{\gamma}^{(2)}\right)\begin{bmatrix} \vdots \\ \sin\tilde{\delta}_{kj} - \sin\tilde{\delta}_{kj}^* \\ \vdots \end{bmatrix}_{\{k,j\}\in\boldsymbol{\varepsilon}} \tag{4-42}$$

where,

$$\boldsymbol{\gamma}^{(1)} = \begin{bmatrix} \frac{1}{M_t}B_{12}E_1E_2 & \cdots & \frac{1}{M_t}B_{kj}E_kE_j & \cdots \\ \vdots & \ddots & & \\ \frac{1}{M_t}B_{12}E_1E_2 & & \ddots & \\ \vdots & & & \ddots \end{bmatrix}_{n\times|\varepsilon|} \tag{4-43}$$

Since the system under consideration is assumed to be lossless, therefore the summation of all electric power flow in the internal node system should be 0 as is shown in the following:

$$\boldsymbol{\gamma}^{(1)}\begin{bmatrix}\vdots\\ \sin\tilde{\delta}_{kj}-\sin\tilde{\delta}_{kj}^{*}\\ \vdots\end{bmatrix}_{\{k,j\}\in\boldsymbol{\varepsilon}}=\begin{bmatrix}\frac{1}{M_t}B_{12}E_1E_2 & \cdots & \frac{1}{M_t}B_{kj}E_kE_j & \cdots\\ \vdots & \ddots & & \\ \frac{1}{M_t}B_{12}E_1E_2 & & \ddots & \\ \vdots & & & \ddots\end{bmatrix}_{n\times|\varepsilon|}\begin{bmatrix}\vdots\\ \sin\tilde{\delta}_{kj}-\sin\tilde{\delta}_{kj}^{*}\\ \vdots\end{bmatrix}_{\{k,j\}\in\boldsymbol{\varepsilon}}=\underline{0}$$

(4-44)

On the other hand, we have

$$\boldsymbol{\gamma}^{(2)}=i^{th}\ node\begin{bmatrix} & & \vdots & & \\ 0\cdots0 & -\frac{1}{m_i}B_{i1}E_iE_1 & \cdots & -\frac{1}{m_i}B_{in}E_iE_n & 0\cdots0\\ & & \vdots & & \end{bmatrix}_{n\times|\varepsilon|}\tag{4-45}$$

The i-th row contains all the branches connecting to bus i.

Take

$$\eta_i=d_i\omega_i-\frac{m_i}{M_t}\sum_k d_k\omega_k\tag{4-46}$$

Substitute ω_i with $\left(\tilde{\omega}_i+\omega_{\mathrm{COA}}\right)$, we have

$$\eta_i=d_i\left(\tilde{\omega}_i+\omega_{\mathrm{COA}}\right)-\frac{m_i}{M_t}\sum_k d_k\left(\tilde{\omega}_k+\omega_{\mathrm{COA}}\right)=d_i\tilde{\omega}_i-\frac{m_i}{M_t}\sum_k d_k\tilde{\omega}_k+\omega_{\mathrm{COA}}\cdot\left(d_i-\frac{m_i}{M_t}\sum_k d_k\right)$$

(4-47)

The first two terms are the linear combination of angular velocities in COA frame and easy to be transferred into matrix form. But the third term on the right-hand side cannot be processed in the same way. Assuming uniform damping, we have

$$\frac{m_i}{d_i} = \lambda = \text{Constant}, \ \forall \ i \in \text{generator set} \tag{4-48}$$

Use this assumption, we have

$$\eta_i = d_i \tilde{\omega}_i - \frac{m_i}{M_t} \sum_k d_k \tilde{\omega}_k = d_i \tilde{\omega}_i - \frac{m_i}{M_t} \sum_k \frac{m_k}{\lambda} \tilde{\omega}_k = d_i \tilde{\omega}_i \tag{4-49}$$

Therefore,

$$\Delta \dot{\tilde{\omega}}_i = -\frac{1}{m_i} \sum_j B_{ij} E_i E_j \left(\sin \tilde{\delta}_{ij} - \sin \tilde{\delta}_{ij}^* \right) - \frac{d_i}{m_i} \tilde{\omega}_i \tag{4-50}$$

To sum up, using the center of angles (COAs) as the reference, the system space model for a lossless power system internal node model in matrix form is as follows:

$$\dot{\tilde{\mathbf{x}}} = \mathbf{A}\tilde{\mathbf{x}} - \mathbf{B}F\left(\mathbf{C}\tilde{\mathbf{x}}\right) \tag{4-51}$$

where,

$$\mathbf{A} = \begin{bmatrix} \mathbf{O}_{n \times n} & \mathbf{I}_{n \times n} \\ \mathbf{O}_{n \times n} & -\mathbf{M}^{-1}\mathbf{D} \end{bmatrix} \tag{4-52}$$

and

$$\mathbf{B} = -\boldsymbol{\gamma}^{(2)} \tag{4-53}$$

For convenience in the rest of the dissertation, the angles and angular velocities in the COA frame will be denoted as δ_i and ω_i, as well as the states, $\mathbf{x} = \left[\mathbf{x}_1, \mathbf{x}_2\right]^{\mathrm{T}}$. The family of Lyapunov functions discussed in equation (4-31) does not have a change in formulation in COA frame. However, by La Salle Invariance Principle [69], the parameter matrices $\mathbf{Q}$ and $\mathbf{K}$ are found such that in some region containing the SEP (here we ignore the subscript without losing generality because any pair of the parameter matrices should satisfy these conditions),

$$\dot{V}(\mathbf{x}) = \mathbf{x}^{\mathrm{T}}\mathbf{QAx} - \mathbf{x}^{\mathrm{T}}\mathbf{QBF} + (\mathbf{Gx})^{\mathrm{T}}\mathbf{KF} \le 0 \tag{4-54}$$

where $\mathbf{Gx} = \begin{bmatrix} \cdots & \dot{\delta}_{kj} & \cdots \end{bmatrix}$ and $\mathbf{F} = F(\mathbf{Cx})$. Taking the $\mathbf{x}$ and $\mathbf{F}$ both to be the states to quasi-linearize the expression we have

$$\begin{aligned}
\dot{V}(\mathbf{x}) &= \mathbf{x}^{\mathrm{T}}\mathbf{QAx} - \mathbf{x}^{\mathrm{T}}\mathbf{QBF} + (\mathbf{Gx})^{\mathrm{T}}\mathbf{KF} \\
&= \mathbf{x}^{\mathrm{T}}\mathbf{QAx} - \mathbf{x}^{\mathrm{T}}\left(\mathbf{QB} - \mathbf{G}^{\mathrm{T}}\mathbf{K}\right)\mathbf{F} \\
&= \begin{bmatrix} \mathbf{x} \\ \mathbf{F} \end{bmatrix}^{\mathrm{T}} \begin{bmatrix} \mathbf{QA} & -\frac{1}{2}\left(\mathbf{QB} - \mathbf{G}^{\mathrm{T}}\mathbf{K}\right) \\ -\frac{1}{2}\left(\mathbf{QB} - \mathbf{G}^{\mathrm{T}}\mathbf{K}\right)^{\mathrm{T}} & 0 \end{bmatrix} \begin{bmatrix} \mathbf{x} \\ \mathbf{F} \end{bmatrix}
\end{aligned} \tag{4-55}$$

Besides, it was proven in [65] that when $\left|\delta_{kj} + \delta_{kj}^{*}\right| \le \pi$,

$$\left(\sin\delta_{kj} - \sin\delta_{kj}^{*}\right)^{2} \le \left(\delta_{kj} - \delta_{kj}^{*}\right)\left(\sin\delta_{kj} - \sin\delta_{kj}^{*}\right) \tag{4-56}$$

Substituting the states into this inequality,

$$\mathbf{F}^{\mathrm{T}}\mathbf{F} \le \mathbf{x}^{\mathrm{T}}\mathbf{C}^{\mathrm{T}}\mathbf{F} \tag{4-57}$$

and in matrix form

$$\begin{bmatrix} \mathbf{x} \\ \mathbf{F} \end{bmatrix}^{\mathrm{T}} \begin{bmatrix} 0 & \frac{1}{2}\mathbf{C}^{\mathrm{T}} \\ \frac{1}{2}\mathbf{C} & -\mathbf{I} \end{bmatrix} \begin{bmatrix} \mathbf{x} \\ \mathbf{F} \end{bmatrix} \ge 0 \tag{4-58}$$

Based on the s-procedure [70], we have

$$-\begin{bmatrix} \mathbf{QA} & -\frac{1}{2}\left(\mathbf{QB} - \mathbf{G}^{\mathrm{T}}\mathbf{K}\right) \\ -\frac{1}{2}\left(\mathbf{QB} - \mathbf{G}^{\mathrm{T}}\mathbf{K}\right)^{\mathrm{T}} & 0 \end{bmatrix} \ge \tau \begin{bmatrix} 0 & \frac{1}{2}\mathbf{C}^{\mathrm{T}} \\ \frac{1}{2}\mathbf{C} & -\mathbf{I} \end{bmatrix} \ge 0 \tag{4-59}$$

where τ is a non-negative scalar number. Further, take $\mathbf{H} = \tau\mathbf{I}$. This inequality guarantees that the problem is discussed within the region specified by $\left|\delta_{kj} + \delta_{kj}^{*}\right| \le \pi$. In this region, the left-hand side of inequality (4-58) holds which makes sure the first term in inequality (4-59) positive semi-definite.

We have the Linear Matrix Inequalities (LMI) to find proper parameter matrices as following:

$$\begin{bmatrix} \mathbf{A}^{\mathrm{T}}\mathbf{Q}+\mathbf{Q}\mathbf{A} & -\left(\mathbf{QB}-\left(\mathbf{KCA}\right)^{\mathrm{T}}-\mathbf{C}^{\mathrm{T}}\mathbf{H}\right) \\ -\left(\mathbf{QB}-\left(\mathbf{KCA}\right)^{\mathrm{T}}-\mathbf{C}^{\mathrm{T}}\mathbf{H}\right)^{\mathrm{T}} & -2\mathbf{H} \end{bmatrix} \leq 0 \tag{4-60}$$

More constraints can be introduced into the process of reaching parameter matrices and thus forming corresponding Lyapunov function in the family. The maximum level set, $\left\{\mathbf{x} \mid V\left(\mathbf{x}\right) \leq v_{\max}\right\}$, of this Lyapunov function that satisfies the conditions specified in the aforementioned Lyapunov's second method and other feasibility constraints serves as the SR estimated with it. An iterative procedure will be conducted to find a proper Lyapunov function in the family that provides maximum SR estimation. This procedure will be discussed in the following section.

4.3.2 Transient Stability Region Estimation With LFF

The basic idea of the constrained stability region assessment is that, for each Lyapunov function generated by the LMIs, find its minimum value. If this minimum value is larger than the function value on the post-fault initial state, this means that the post-fault state will be able to follow its trajectory to reach the stable equilibrium point, the stability of the system within the level-set of this particular Lyapunov function is certified, and thus the maximized stability region is found. It is to be noted that, the minimum value of each Lyapunov function in the family should be found under the constraints of both system original operation limits and the LVRT restrictions. The detailed process is stated as follows.

Step 1) Form up the state space model considering internal nodes with Kron-reduction and transfer this model into COA frame.

Step 2) Set $i=1$; initialize the first Lyapunov function $V^{(i)}(\mathbf{x})$ in the family specified in (4-31) with the parameter matrices values as following

$$\mathbf{Q}_i = \mathbf{Q}\_initial = \begin{bmatrix} 0 & 0 \\ 0 & \mathbf{M} \end{bmatrix}_{2n\times 2n} \tag{4-61}$$

$$\mathbf{K}_i = \mathbf{K}\_initial = \begin{bmatrix} \ddots & 0 & 0 \\ 0 & B_{kj}E_kE_j & 0 \\ 0 & 0 & \ddots \end{bmatrix}_{n\times n} \tag{4-62}$$

Step 3) Evaluate $V^{(i)}(\mathbf{x}_0)$ where $\mathbf{x}_0$ refers to the post-fault initial state, and find $V_{\max}^{(i)}$

The optimization process to find $V_{\max}^{(\bullet)}$ is as follows:

$$\begin{aligned} V_{\max}^{convex} = & \quad \max \quad v \\ s.t. & \quad \mathbf{x} \in \mathbf{FR} \end{aligned} \tag{4-63}$$

where, $\mathbf{FR}$ is the feasibility region defined as

$$\mathbf{FR} = \begin{cases} \{\mathbf{x} : V(\mathbf{x}) < v\} \\ |\delta_{kj}| \le \frac{\pi}{2},\ \{k, j\} \in \boldsymbol{\varepsilon} \\ \text{operation constraints} \end{cases} \tag{4-64}$$

This region is basically defined by two parts, one is that phase angle differences between any two generators should be bounded within $\left[-\pi/2,\ \pi/2\right]$. This constraint will make sure that the problem is convex, which is proved in [65].

Step 4) Solve LMIs in (4-60) combined with $V^{(i+1)}(\mathbf{x}_0) < V_{\max}^{(i)} - \xi$ to find a pair of feasible parameter matrices $\mathbf{Q}_{i+1}$ and $\mathbf{K}_{i+1}$ for $V^{(i+1)}$, where ξ is the predefined step size (this is only a feasible solution to the LMIs and not necessarily the optimal one);

Compensating inequalities within the iteration process for finding new Lyapunov Functions:

$$V^{(i+1)}(\mathbf{x}_0) = \frac{1}{2}\mathbf{x}_0^{\mathrm{T}}\mathbf{Q}_{i+1}\mathbf{x}_0 - \sum_{\{k,j\}\in\boldsymbol{\varepsilon}} K_{i+1,\,\{k,j\}}\left(\cos\delta_{kj,\,0} + \delta_{kj,\,0}\sin\delta_{kj}^{*}\right) < V_{\max}^{(i)} - \xi \tag{4-65}$$

In matrix form, the new constraint is as following:

$$V^{(i+1)}(\mathbf{x}_0) = \frac{1}{2}\mathbf{x}_0^{\mathrm{T}}\mathbf{Q}_{i+1}\mathbf{x}_0 - \begin{bmatrix}1 & \cdots & 1\end{bmatrix}_{1\times|\boldsymbol{\varepsilon}|}\mathbf{K}_{i+1}\left[\cos(\mathbf{E}\boldsymbol{\delta}_0) + (\mathbf{E}\boldsymbol{\delta}_0).\times\sin(\mathbf{E}\boldsymbol{\delta}^{*})\right] < V_{\max}^{(i)} - \xi \tag{4-66}$$

Step 5) Check if $V^{(i+1)}(\mathbf{x}_0) < V_{\min}^{(i+1)}$, stability certificate found, the level set, $V^{(i+1)} < V_{\max}^{(i+1)}$ indicates the stability region; otherwise, set $i = i+1$ and iteratively return to **Step 3)**.

4.4 Constrained Transient Stability Assessment With Lyapunov Functions Family

4.4.1 Constrained Stability Region

Simply adding operational limits to the constraints in the optimization process stated in (4-63) and (4-64) can bring much conservativeness to the estimated SR results because the expansion of the level set will stop immediately once its boundary reaches the FB. However, there are some parts of the FB that have some characteristics which indicate the directions of the trajectories once they meet these parts. Based on these features of the FB, the concept of CSR is established [62] which provides insights for system TSA considering operation limits like renewable energy sources

LVRT constraints. The basic idea is to equivalently convert the original constrained autonomous non-linear system (as shown in equation) to an unconstrained one (as shown in equation).

$$\begin{aligned} &\dot{\mathbf{x}} = f(\mathbf{x}) \\ &h_i(\mathbf{x}) \le 0,\ \forall i \end{aligned} \tag{4-67}$$

$$\dot{\mathbf{x}} = \left(\prod_i h_i(\mathbf{x}) \right) f(\mathbf{x}) \tag{4-68}$$

It can be seen that besides the equilibrium points (EP) of the original system, $\{\mathbf{x} \mid f(\mathbf{x}) = 0\}$, there is another type of EPs that are the points on the feasibility boundary characterized by $\left\{\mathbf{x} \mid \prod_i h_i(\mathbf{x}) = 0\right\}$ of the converted system. These new EPs are classified into three categories: the flow-in EPs, the semi-saddle EPs, and the flow-out EPs[71]. To illustrate, an example is shown in Figure. 20, By definition, CSR of a given SEP, $\mathbf{x}_{sep}$, of a system is a set of points from which the emerging trajectories never exit the FR and converge to $\mathbf{x}_{sep}$. The initial point of an unstable

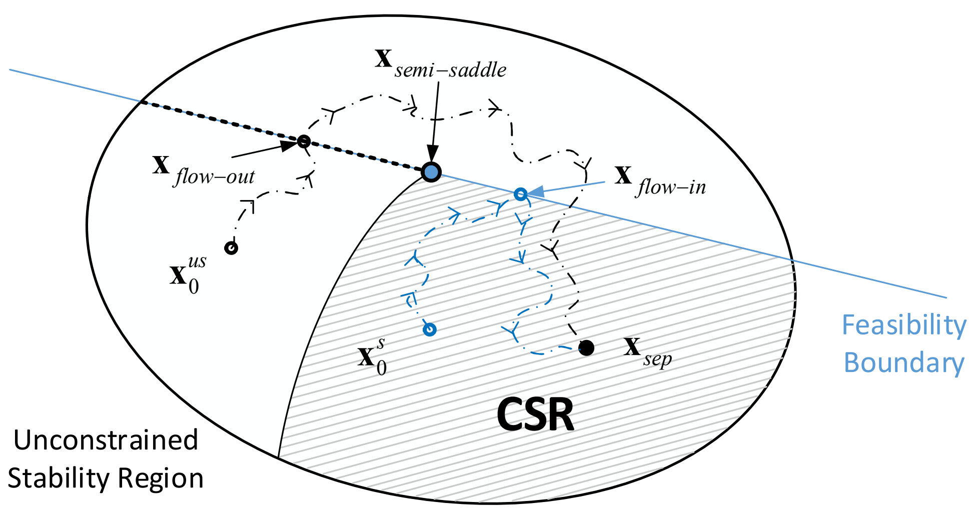

Figure. 20. Constrained Stability Region Example

trajectory, x_0^{us}, is inside the FR. The trajectory starting from it reaches the feasibility boundary

(FB)at one point, $x_{flow-out}$, on the flow-out part and crosses the FB. Thus, part of the trajectory is infeasible and this point is not in the CSR (shaded region). On the other hand, the trajectory starting from the initial point, x_0^s, also reaches the FB. However, the direction of the trajectory is reversed and it returns back to the FR. Hence, this point is inside the CSR.

Furthermore, the FB is comprised of three types of components: the flow-out (dashed line) where trajectories starting in the vicinity cross the boundary to the infeasible region, the flow-in (straight line) where they get repelled to the feasible side and the semi-saddle where they are tangential to the FB [62]. It was shown by Loparo in [62] that only flow-in and semi-saddle components of the FB can lie on the boundary of the CSR.

Now, the complexity of the CSR that can be estimated using only a level set of a given Lyapunov function $V(\mathbf{x})$ is heavily restricted by the degree of the function chosen. This usually introduces conservativeness which can be reduced by using a combination of parts of the FB itself and a level set of the Lyapunov function. The aim is to find the maximal level set $\{\mathbf{x} \mid V(\mathbf{x}) \leq v_{\max}\}$ satisfying the following constraints –

$$\begin{cases} \{\mathbf{x} \mid V(\mathbf{x}) \leq v_{\max}\} \cap \{\mathbf{x} \mid \mathbf{x} \text{ on } \mathbf{FB}\} \subseteq \text{Flow-in} \cup \text{Semi-Saddle} \\ \{\mathbf{x} \mid V(\mathbf{x}) \leq v_{\max}\} \subseteq \{\mathbf{x} \mid \dot{V}(\mathbf{x}) \leq 0\} \\ \{\mathbf{x} \mid V(\mathbf{x}) \leq v_{\max}, \dot{V}(\mathbf{x}) = 0\} = \mathbf{x}_{sep} \end{cases} \tag{4-69}$$

The CSR estimate is then given by $\{\mathbf{x} \mid V(\mathbf{x}) \leq v_{\max}\} \cap \mathbf{FR}$. To be more specific, the flow-in or flow-out characteristics of the FB can be specified with the knowledge of trajectory directions of the state points on the FB. In nature, the states of angular velocities are the time derivatives of the other part of the states, rotor angles. Therefore, it is convenient to find the aforementioned directions if the operation limits are in forms of linear combinations of rotor angles. The directions are just the same linear combinations of corresponding angular velocities. With this linearity assumption, the FB can be easily expressed with linear equations. Detailed formulation of the feasibility analysis is described in the following subsection.

4.4.2 Feasibility Region Assessment

Since the prerequisites of the CSR is that it belongs to a stability region, only the parts of FB inside the Lyapunov function level set is to be considered. The feasibility of the level set estimated with the concerned Lyapunov function which specified by the FR discussed in equation (4-64) is transferred into the question of whether the part of FB encompassed in the level set has flow-out points included.

The FB discussed here is mainly concerned with the linear inequality constraints brought by the convexity constraints and the operation limits. In this dissertation, the main objective is to consider the impacts on the system transient stability caused by renewable energy sources integration. Therefore, the LVRT limits on the system bus voltage magnitudes are taken as operation limits and investigated. The bus voltage magnitudes where renewable energy sources are integrated into the system should be kept above a certain voltage magnitude criterion curve to maintain the online status of these sources. In reality, it is easy to see that there is no linear dependency between system bus voltages and internal nodes rotor angles. The power flow equations can be a good insight to take reference. However, a method is proposed to approximate this non-linear relationship with a series of linear inequalities and in general, a polytope in state space. The detailed process of this method is discussed in the following subsection. As of now, let us assume that we have approximated linear inequalities to represent the LVRT constraints. The inequalities to specify the FR includes linear approximated LVRT constraints and convexity constraints which limit the rotor angle differences in COA frame to be smaller than $\frac{\pi}{2}$, i.e. $\delta_{kj} \leq \frac{\pi}{2}$ and $\delta_{kj} \geq -\frac{\pi}{2}$ where $\{k, j\} \in \boldsymbol{\varepsilon}$.

In general term, the inequalities constraints are

$$\mathbf{L}_{ineq} \cdot \mathbf{x}_1 + \mathbf{l}_{ineq} \leq 0 \tag{4-70}$$

where, $\mathbf{L}_{ineq} \in \mathbf{R}^{N_{ineq} \times n}$ refers to the coefficient matrix specified by the linear dependency within inequality constraints, and N_{ineq} is the number of linear inequality constraints; $\mathbf{l}_{ineq} \in \mathbf{R}^{N_{ineq} \times 1}$ refers to the corresponding constant vector.

The equality constraints are concerned with the COA frame where the summation of rotor angles and angular velocities weighted by generators' inertia constants are 0 as shown in (4-71)

$$\begin{cases} \sum_i m_i \delta_i = 0 \\ \sum_i m_i \omega_i = 0 \end{cases} \tag{4-71}$$

In general term, the equality constraints are

$$\mathbf{L}_{eq} \cdot \mathbf{x} + \mathbf{l}_{eq} = 0 \tag{4-72}$$

where, $\mathbf{L}_{eq} \in \mathbf{R}^{2 \times 2n}$ refers to the coefficient matrix specified by (4-71); $\mathbf{l}_{eq} = \begin{bmatrix} 0 \\ 0 \end{bmatrix}$ refers to the corresponding constant vector.

It is to be noted that the inequality constraints are only concerned with rotor angles, but the equality constraints are concerned with both the rotor angles and the angular velocities. The inequality constraints and the equality constraints together form up the approximated combined feasibility region (ACFR), in which the equality constraints mount the ACFR onto some lower dimensional subspace within the state space and specified by the linear relation in (4-72). The boundaries of the ACFR, i.e. ACFB, are a collection of hyperplanes defined by

$$\mathbf{L}_{ineq} \cdot \mathbf{x}_1 + \mathbf{l}_{ineq} = 0 \tag{4-73}$$

This collection of hyperplanes also serve as facets of the polytope which is most likely different from that of the LVRT constraints approximation because of the introduction of the convex constraints.

Therefore, to check whether the concerned Lyapunov level set $\{\mathbf{x} \mid V(\mathbf{x}) \le v\}$ is feasible or not, one can simply pick up each inequality constraint one by one, set it to be an equality constraint which makes the process reaches the facet, and check whether there will be flow-out points exist on it. The detailed process is described as following.

Step 1) Select the concerned Lyapunov function $V(\mathbf{x})$.

Step 2) Set $i = 1$.

Step 3) Select the i-th inequality. Namely, select the i-th row in $\mathbf{L}_{ineq}$, $\mathbf{L}_{ineq}^{(i)} \in \mathbf{R}^{1\times n}$, and the i-th entry in $\mathbf{l}_{ineq}$, $\mathbf{l}_{ineq}^{(i)} \in R$; Solve the following optimization problem:

$$\begin{array}{ll} & \exists\, \mathbf{x} \\ s.t. & \max_{\mathbf{x}} \ \mathbf{L}_{ineq}^{(i)} \cdot \mathbf{x}_2 > 0 \\ & \mathbf{L}_{ineq}^{(i)} \cdot \mathbf{x}_1 + \mathbf{l}_{ineq}^{(i)} = 0 \\ & \mathbf{L}_{ineq}^{(j)} \cdot \mathbf{x}_1 + \mathbf{l}_{ineq}^{(j)} \le 0 \ , \ \forall\, j \ne i \\ & \mathbf{L}_{eq} \cdot \mathbf{x}_1 + \mathbf{l}_{eq} = 0 \\ & V(\mathbf{x}) \le v \end{array} \tag{4-74}$$

Here, because $\mathbf{L}_{ineq}^{(i)} \cdot \mathbf{x}_2$ is the time derivative of $\left(\mathbf{L}_{ineq}^{(i)} \cdot \mathbf{x}_1 + \mathbf{l}_{ineq}^{(i)}\right)$, the direction change of trajectories can be simply specified by this term.

Step 4) If there is any feasible solution to this optimization problem, this means that there exists at least one point in the level set that can make the candidate estimate CSR contains flow-out point(s) and thus non-invariant as well as invalid. Return infeasible and end the process. Otherwise, move on to the next inequality constraint by having $i = i + 1$ and go to **Step 3)**.

Step 5) If all the inequality constraints are evaluated with the aforementioned process and there is no infeasibility reported, then label the current Lyapunov level-set as feasible and end the process.

4.4.3 Constrained Stability Region Estimation With Lyapunov Functions Family

The CSR is estimated with the process discussed in subsection 4.3.2 combined with the feasibility constraints analyzing approach described in subsection 4.4.2. This can be summarized as follows. The conventional energy function, equation (4-30), is taken as the initial Lyapunov function of a family of the functions in the same formulation. A linear search of the level set value is conducted until the maximum level set containing no flow-out points is obtained. The flow-out point is examined on each ACFB with the aforementioned feasibility analyzing procedure. For the particular fault concerned, if the post-fault initial point in the state space is inside this maximum feasible Lyapunov level set, then the stability of the system under such disturbance and clearing time is certified. Otherwise, the LMIs based on Lyapunov theory and concerned state space region are used to find another pair of parameter matrices which decide the new Lyapunov function in the family. One specified condition, equation (4-65), in this process is added to the LMI optimization problem to guarantee the new Lyapunov function will have improvement in the estimate of CSR in terms of the amount of overlap with the portion of the state space relevant to a given fault trajectory under study.

The estimated CSR considering polytopic feasibility region is visualized in Figure. 21. In this figure, one can see that the original FR is approximated with a polytope. The boundary of this polytope is composed of two parts: flow-out and flow-in. Their connecting points are semi-saddle points. The flow-in and flow-out parts are continuous because of the linearity of approximated ACFB. Using Lyapunov level set to estimate the constrained SR, one would reach the remarkable conservative results by considering the strict constraints. However, using the CSR concept, the level set is able to expand beyond the strict constraints and the result is much less conservative.

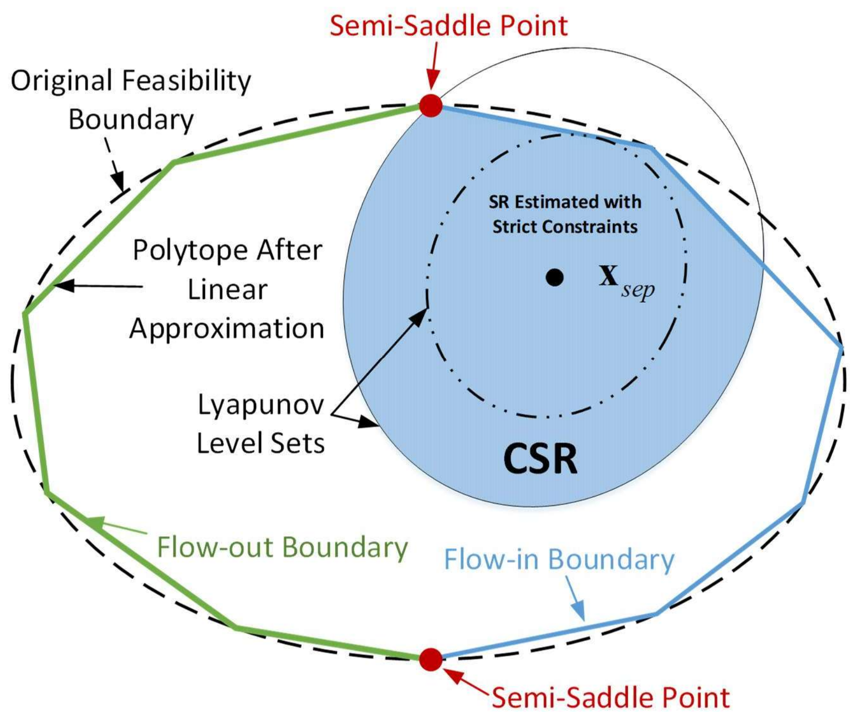

Figure. 21. CSR Estimated With Polytopic Feasibility Region

4.5 Renewables Low Voltage Ride Through Constraints

The LVRT is a security criterion on the renewable energy sources operation. This operation limit is added non-automatically upon the voltage magnitude on the point of common coupling (PCC) of concerned renewables. However, taking the current discussed problem as the background, all the analysis is within the state space and the variables concerned are generator rotor angles and corresponding angular velocities. Therefore, there is a need to represent the bus voltage magnitude in the original power system with these states. The operation limits can thus be considered in the state space. Furthermore, there can be a possibility for potential linear approximation of these operation limits. This is enabled by the following derivation and process.

4.5.1 System Bus Voltage Representation With Generator States

According to (4-12), one can find the linear relation between the system bus voltages $\mathbf{V}$ and the terminal voltages $\mathbf{E}$ of the generators within the system. Both of them contains complex values. Taking $\mathbf{P} \in \mathbf{C}^{N \times n}$

$$\mathbf{P} = -\left(\mathbf{Y}_{bus}^{new}\right)^{-1} \mathbf{Y}_{21} \tag{4-75}$$

one has

$$v_i = \sum_{k=1}^{n} \left(real\left(p_{ik}\right) + j \cdot imag\left(p_{ik}\right)\right) E_k e^{j\delta_k} \tag{4-76}$$

where v_i refers to the voltage on bus i, $real\left(p_{ik}\right)$ and $imag\left(p_{ik}\right)$ refer to the real and imaginary parts of the $\left(i, k\right)$ entry in $\mathbf{P}$, E_k and δ_k are the terminal voltage magnitude and rotor angle of the generator k.

Therefore, the square of the voltage magnitude of bus i is:

$$\left|v_i\right|^2 = \left[\sum_{k=1}^{n} E_k \left(real\left(p_{ik}\right)\cos\delta_k - imag\left(p_{ik}\right)\sin\delta_k\right)\right]^2 + \left[\sum_{k=1}^{n} E_k \left(real\left(p_{ik}\right)\sin\delta_k + imag\left(p_{ik}\right)\cos\delta_k\right)\right]^2 \tag{4-77}$$

Simplify $\left|v_i\right|^2$, we have

$$\begin{cases} A = \left[\sum_{k=1}^{n} E_k \left(real\left(p_{ik}\right) \cdot \cos\delta_k - imag\left(p_{ik}\right) \cdot \sin\delta_k \right) \right]^2 \\ B = \left[\sum_{k=1}^{n} E_k \left(real\left(p_{ik}\right) \cdot \sin\delta_k + imag\left(p_{ik}\right) \cdot \cos\delta_k \right) \right]^2 \end{cases} \tag{4-78}$$

For simplicity, take

$$\begin{cases} C_{k(r)} = E_k \cdot real\left(p_{ik}\right) \\ C_{k(i)} = E_k \cdot imag\left(p_{ik}\right) \end{cases} \tag{4-79}$$

So that

$$A = \left[\sum_{k=1}^{n} \left(C_{k(r)} \cos\delta_k - C_{k(i)} \sin\delta_k \right) \right]^2 \tag{4-80}$$

$$B = \left[\sum_{k=1}^{n} \left(C_{k(r)} \sin\delta_k + C_{k(i)} \cos\delta_k \right) \right]^2 \tag{4-81}$$

Take

$$D_k = \left(C_{k(r)}^2 + C_{k(i)}^2 \right)^{\frac{1}{2}} \tag{4-82}$$

and

$$\cos\delta_{k(c)} = \frac{C_{k(r)}}{\left(C_{k(r)}^2 + C_{k(i)}^2 \right)^{\frac{1}{2}}} \tag{4-83}$$

where, $\delta_{k(c)} \in [0\ ,\ \pi]$ refers to the angle constant that is decided by the system admittances. This constant is corresponding to generator k.

Therefore,

$$C_{k(r)} \cos\delta_k - C_{k(i)} \sin\delta_k = D_k \cos\left(\delta_k + \delta_{k(c)} \right) = e_k \tag{4-84}$$

and

$$C_{k(r)}\sin\delta_k + C_{k(i)}\cos\delta_k = D_k\sin\left(\delta_k + \delta_{k(c)}\right) = f_k \tag{4-85}$$

So

$$\begin{cases} A = \left[\sum_{k=1}^{n} D_k\cos\left(\delta_k + \delta_{k(c)}\right)\right]^2 = \sum_{k}^{n} e_k \sum_{j}^{n} e_j \\ B = \left[\sum_{k=1}^{n} D_k\sin\left(\delta_k + \delta_{k(c)}\right)\right]^2 = \sum_{k}^{n} f_k \sum_{j}^{n} f_j \end{cases} \tag{4-86}$$

Since

$$e_k e_j = D_k\cos\left(\delta_k + \delta_{k(c)}\right) D_j\cos\left(\delta_j + \delta_{j(c)}\right) = D_k D_j\cos\left(\delta_k + \delta_{k(c)}\right)\cos\left(\delta_j + \delta_{j(c)}\right) \tag{4-87}$$

$$f_k f_j = D_k\sin\left(\delta_k + \delta_{k(c)}\right) D_j\sin\left(\delta_j + \delta_{j(c)}\right) = D_k D_j\sin\left(\delta_k + \delta_{k(c)}\right)\sin\left(\delta_j + \delta_{j(c)}\right) \tag{4-88}$$

we have the system bus voltage magnitude $|v_i|^2$ represented by the generators rotor angles or states $\mathbf{x}_1$. These states are in the form of angle differences, so the value is equivalent to that in COA frame.

$$\begin{aligned} |v_i|^2 &= A + B = \sum_k e_k \sum_j e_j + \sum_k f_k \sum_j f_j = \sum_k \sum_j \left(e_k e_j + f_k f_j\right) \\ &= \sum_k \sum_j D_k D_j \left[\cos\left(\delta_k + \delta_{k(c)}\right)\cos\left(\delta_j + \delta_{j(c)}\right) + \sin\left(\delta_k + \delta_{k(c)}\right)\sin\left(\delta_j + \delta_{j(c)}\right)\right] \\ &= \sum_k \sum_j D_k D_j \cos\left(\delta_k - \delta_j + \delta_{k(c)} - \delta_{j(c)}\right) \\ &= \sum_k \sum_j D_k D_j \cos\left(\delta_{kj} + \delta_{kj(c)}\right) \end{aligned} \tag{4-89}$$

where, $\delta_{kj} \in \left[-\frac{\pi}{2}\ ,\ \frac{\pi}{2}\right]$ and $\delta_{kj(c)} \in \left[-\pi\ ,\ \pi\right]$.

4.5.2 Low Voltage Ride Through Constraints

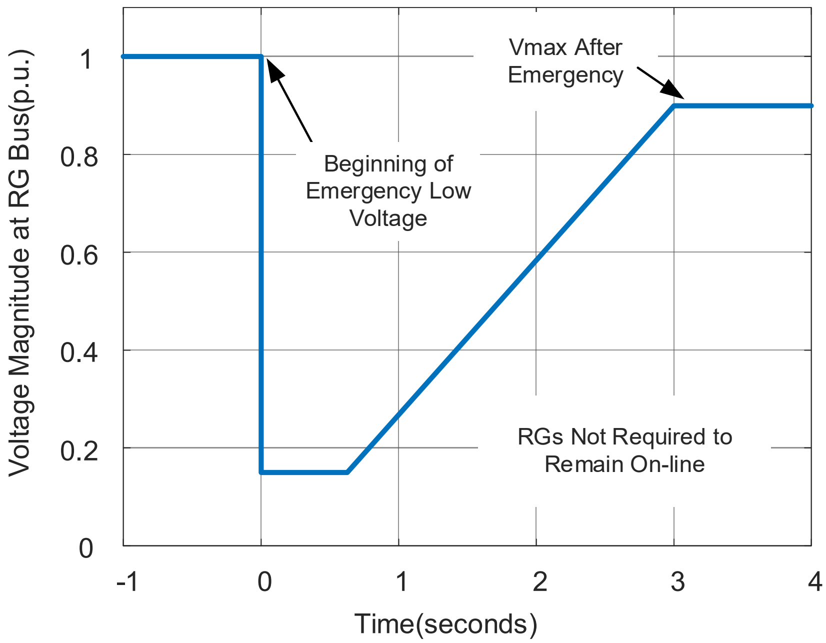

Figure. 22. FERC Low Voltage Ride Through Curve

As introduced before, the LVRT curve gives a lower limit on the bus voltage and violation of which results in RGs tripping. A typical LVRT curve can be seen in Figure. 22 [72]. It can be seen that this curve reveals a relationship between the renewable energy sources connecting bus voltage magnitude and time which can be expressed as a function of time, $V_{LVRT}(t):\mathbf{R}\rightarrow\mathbf{R}$. The operation constraints that keep the concerned renewable sources online is that the bus voltage magnitude is always higher than this curve during and after the disturbance, which can be expressed with the following inequality:

$$h_i(\mathbf{x}_1,t)=|v_i|^2\geq(V_{LVRT}(t))^2 \tag{4-90}$$

where, $i\in\mathbf{N}_{rg}$ and $\mathbf{N}_{rg}$ is the set of bus numbers where the system has renewables integrations.

Time-varying constraints will make the system to be non-autonomous and are difficult to handle in the Lyapunov approach. Therefore it is conservatively converted to the following time independent formulation.

$$|v_i|^2 \geq V_{LVRT,\max} = \max_t \left(V_{LVRT}(t)\right)^2 \tag{4-91}$$

This approach only brings conservativeness in systems with slow voltage recovery and usually not so much in systems where loads are modeled as static. However, this configuration of the LVRT constraints is non-linear and the non-linear term is:

$$g_i(\mathbf{x}_1) = \sum_k \sum_j D_k D_j \cos\left(\delta_{kj} + \delta_{kj(c)}\right) \tag{4-92}$$

Since the cosine function is even, computation of half of the cosine terms in (4-92) can be saved. For the cases where $k = j$, the terms are simply constants. Therefore, for each $g_i(\mathbf{x}_1)$, there are $\binom{n}{2} = \frac{1}{2}n(n-1)$ cosine terms. It can be expressed as follows:

$$g_i(\mathbf{x}_1) = 2 \times \sum_{k=1}^{n} \sum_{j=k+1}^{n} D_k D_j \cos\left(\delta_{kj} + \delta_{kj(c)}\right) + \sum_{k=1}^{n} D_k^2 \tag{4-93}$$

As has been discussed in the previous section, the LVRT constraints should be linearized to fit into the CSR estimation process. This non-linear term is approximated with multiple lines and the feasibility region is thus approximated with these lines to be a polytope. The approximation process is summarized into a kind of optimization problems and discussed in the next subsection.

4.5.3 Polytopic Inner Approximation Of LVRT Constrained Feasibility Region

Since the LVRT constraint is a summation of cosine terms in angle differences with each angle difference pair constrained to the finite region $|\delta_{kj}| \leq \frac{\pi}{2}$, one can simply find a lower linear approximation individually for each cosine term and add them to convert the overall non-linear constraint to a linear one. That being said, this is bound to bring conservativeness in the inner approximation of the LVRT constrained feasibility region. This can be overcome by using a combination of linear functions for approximating each cosine term as shown in Figure. 23 (a), (b), and (c) which demonstrate approximation for different $\delta_{kj(c)}$ values.

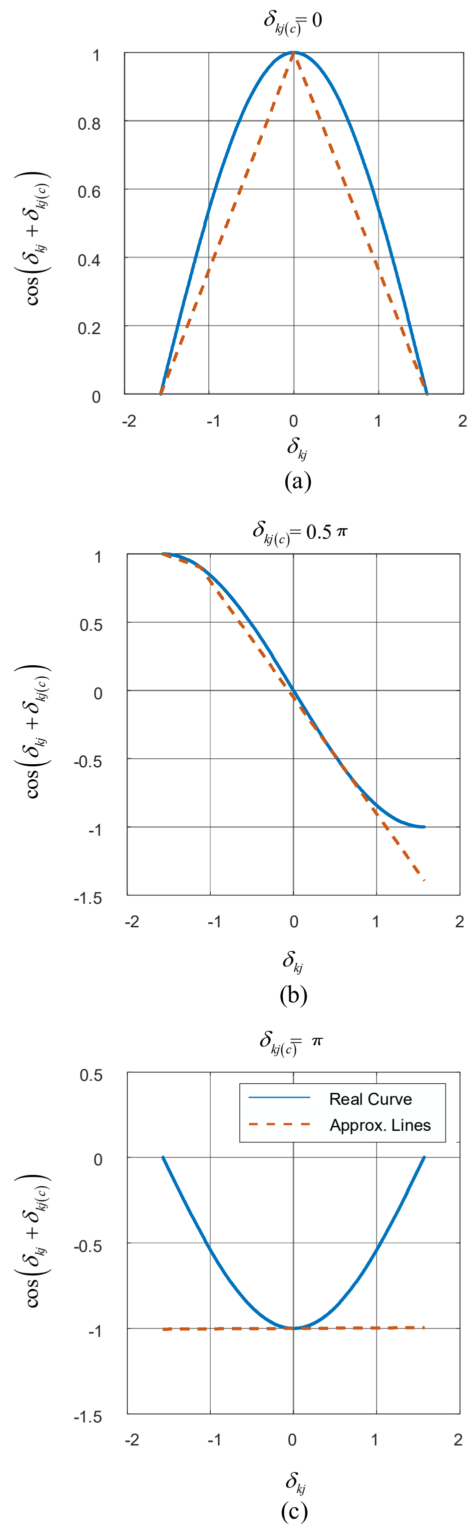

Figure. 23. Examples of Linear Approximation of Single Cosine Curve

However, by introducing multiple lines to approximate each single cosine term, the resulted approximated feasibility region should consider all these lines. This means that the summation of all combinations of the lines for each term should be considered. As an example, assume the concerned LVRT constraint is $g(\mathbf{y}) = a_1 \cos(y_1) + a_2 \cos(y_2) \geq \lambda$. The first term is approximated by the minima of two linear functions, i.e. $\min\left(m_{11}y_1 + c_{11},\, m_{12}y_1 + c_{12}\right)$. Similarly, The second term is approximated by $\min\left(m_{21}y_2 + c_{21},\, m_{22}y_2 + c_{22}\right)$. Then the overall feasibility region approximation is as following.

$$g^{approx}(\mathbf{y}) = \min\left(m_{11}y_1 + c_{11},\, m_{12}y_1 + c_{12}\right) + \min\left(m_{21}y_2 + c_{21},\, m_{22}y_2 + c_{22}\right) \geq \lambda \tag{4-94}$$

This region can also be written by the following set of constraints yielding a polytope –

$$\left\{\begin{array}{l} \mathbf{y} \mid \left(m_{11}y_1 + c_{11}\right) + \left(m_{21}y_2 + c_{21}\right) \geq \lambda \cap \left(m_{12}y_1 + c_{12}\right) + \left(m_{21}y_2 + c_{21}\right) \geq \lambda \cap \\ \quad \left(m_{11}y_1 + c_{11}\right) + \left(m_{22}y_2 + c_{22}\right) \geq \lambda \cap \left(m_{12}y_1 + c_{12}\right) + \left(m_{22}y_2 + c_{22}\right) \geq \lambda \end{array}\right\}$$

Generalizing, an LVRT constraint with $N_{\cos}$ cosine terms where the i th term is approximated by the minimum of $N_{lines,i}$ linear functions results in an overall polytope with $\prod_i^{N_{\cos}} N_{lines,i}$ facets/linear constraints.

Assuming that for a given cosine term $\cos\left(\delta_{kj} + \delta_{kj(c)}\right)$ in Figure. 24, one needs to find a set of lower bounding N_{lines} number of linear functions with the form $m_i \times \delta_{kj} + c_i$ for $i = 1 : N_{lines}$. The approximate function as mentioned before is formulated as $\min_i\left(m_i \times \delta_{kj} + c_i\right)$. Earlier it was seen that $\left|\delta_{kj}\right| \leq \frac{\pi}{2},\ \forall\ k, j$ for convexity of Lyapunov function $V(\mathbf{x})$ which restricts the analysis to this region. The problem of finding these functions can be formulated as the following optimization problem. The objective function value is evaluated with various angle difference's values ranging from $-\frac{\pi}{2}$ to $\frac{\pi}{2}$ and the step size of $\frac{\pi}{1000}$, which can be expressed as $\delta_{kj}(p) = -\frac{\pi}{2} + p \cdot \frac{\pi}{1000}$ and $p = 0:1000$.

$$\begin{aligned} \min_{[m_1, m_2, \cdots],[c_1, c_2, \cdots]} \quad & \sum_{p=0}^{1000}\left(\cos\left(\delta_{kj}(p)+\delta_{kj(c)}\right)-\min\left(\min_i\left(m_i \times \delta_{kj}(p)+c_i\right)\right)\right)^2 \\ s.t. \quad & \cos\left(\delta_{kj}(p)+\delta_{kj(c)}\right) \geq \min\left(\min_i\left(m_i \times \delta_{kj}(p)+c_i\right)\right) \\ & \left|\delta_{kj}(p)\right| \leq \frac{\pi}{2} \end{aligned} \tag{4-95}$$

Directly using m and c as decision variables will result in a space with a large number of local minima. Solutions where the lower bounding approximating function should have intersected the original function but did not were common and evidently suboptimal as shown in Figure. 24. Thus, the search space is restricted by only looking for resulting polytopes having vertices on the actual

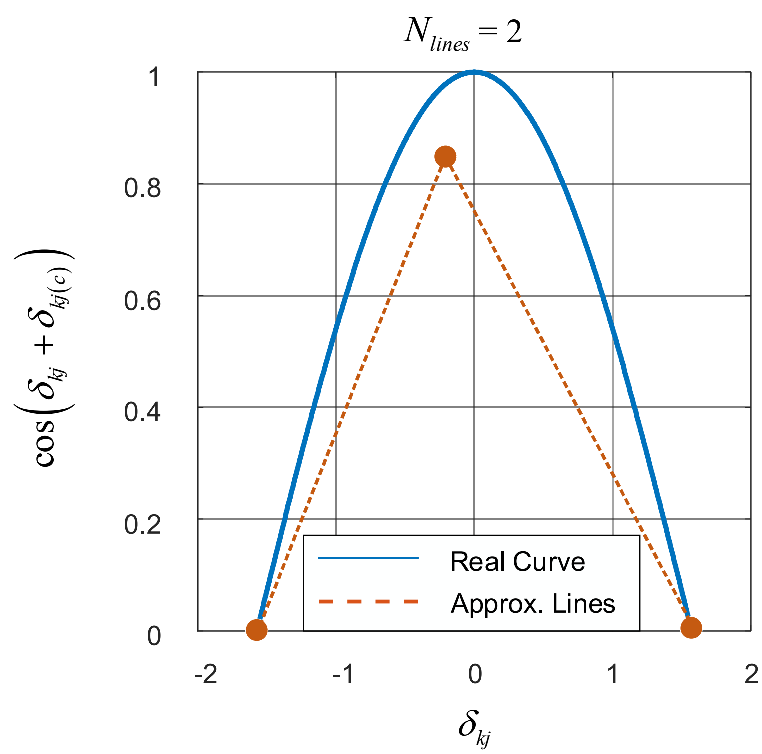

Figure. 24. The Example of Local Optimum

curve. Since the function is in a single variable δ_{kj}, $N_{lines}+1$ number of points are chosen which have the form of $\left\{\left(\delta_{kj}, \cos\left(\delta_{kj}+\delta_{kj(c)}\right)\right)\right\}$, on the original cosine curve. Then they are sorted by their δ_{kj} coordinates. The lines connecting successive points become the approximating linear functions/facets of the final polytope. Thus, the search is now for an optimal set of points on the original curve. This was then solved using particle swarm optimization (PSO)[73]. Conservativeness of the ACFR, when compared to the actual combined feasibility region, decreases with increasing N_{lines} as shown in Figure. 25 (a) and (b). For each RG integrated bus, its approximated LVRT constraints have the linear form as

$$g_i^{approx}\left(\mathbf{x}_1\right) = \mathbf{M}_i \mathbf{L} \mathbf{x}_1 + \sum_{row} \mathbf{C}_i + C_{sep} \geq V_{LVRT,\max} \tag{4-96}$$

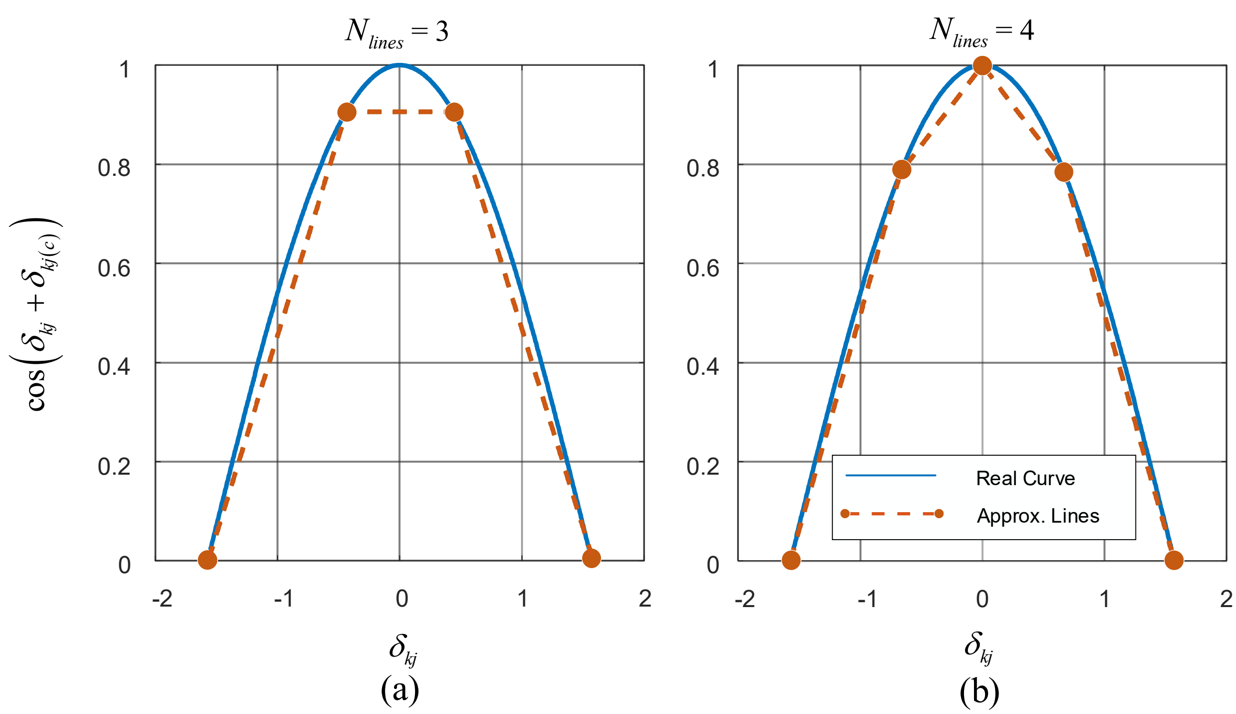

Figure. 25. The Examples of Multiple Lines Used for Approximation

where $\mathbf{M}_i \in \mathbf{R}^{\left(N_{lines} \wedge \binom{n}{2}\right) \times \binom{n}{2}}$ is the parameter matrix referring to the slope of the optimized lines; $\mathbf{L}$ maps rotor angles to angle differences, and then $\mathbf{L}\mathbf{x}_1 = \left[\left(\delta_{kj} - \delta_{kj}^{*} \right)_{\{k,\, j\} \in \boldsymbol{\varepsilon}} \right]^{\mathrm{T}}$; $\mathbf{C}_i \in \mathbf{R}^{\left(N_{lines} \wedge \binom{n}{2}\right) \times \binom{n}{2}}$ is the parameter matric referring to the biases of the optimized lines which are corresponding to each slope in $\mathbf{M}_i$ and $\sum_{row} \mathbf{C}_i$ refers to the constant vector where each entry is the summation of the corresponding row in $\mathbf{C}_i$, take $\mathbf{c}_i^{row} = \sum_{row} \mathbf{C}_i \in \mathbf{R}^{\left(N_{lines} \wedge \binom{n}{2}\right) \times 1}$; $C_{sep} = \mathbf{M}_i \mathbf{L} \boldsymbol{\delta}^{*}$ is the constant used to compensate the decrease brought by SEP values in $\mathbf{x}_1$ and $\boldsymbol{\delta}^{*}$ is the vector of rotor angles of SEP.

The algorithm to find the inequality constraints for the voltage magnitudes on all the buses with renewables integration can be summarized as follows.

Algorithm 1 LVRT Constraints Polytope Approximation

Initialize N_{lines} *and* $i \leftarrow 1$
$P \leftarrow \binom{n}{2}$
$C \leftarrow \binom{N_{lines}}{2}$
while $i \leq N_{rg}$ **do**
    $l \leftarrow 1$
    while $l \leq P$ **do**
        $g_i^{(l)}(\delta_{kj}) \leftarrow C_k C_j \cos(\delta_{kj} - \delta_{kj(c)})$
        Set decision variables $\vec{m} \in R^{N_{lines}}$ *for lines' gradients and* $\vec{c} \in R^{N_{lines}}$ *for lines' biases*
        Set samples $\vec{\delta}_s = -\pi/2 : (\pi/1000) : \pi/2$
        Set up objective function/fitness as previously described
        Use PSO to find optimum $\vec{m}_b^{(l)}, \vec{c}_b^{(l)}$ *for* $g_i^{(l)}$
        $l++$
    Find rectangular grid in P*-D space:*
    $[\mathbf{X}_1, ..., \mathbf{X}_P] = ndgrid(1 : N_{lines}, ..., 1 : N_{lines})$
    $p \leftarrow 1$
    Initialize matrices $\mathbf{M}_k$ *and* $\mathbf{C}_k$ *for generated polytope*
    Set matrix $\mathbf{\Gamma}$ *to restore combination of indices of* $\vec{m}_b$*'s and* $\vec{c}_b$*'s reached by PSO*
    while $p \leq (C \wedge P)$ **do**
        $\mathbf{\Gamma}(p, :) = [\mathbf{X}_1(p), ..., \mathbf{X}_P(p)]$
        Pick (m, c) *pairs from each* $\vec{m}_b^{(l)}, \vec{c}_b^{(l)}$ *based on indices in* $\mathbf{\Gamma}(p, :)$
        Combine them to be two new row vectors $\vec{a}, \vec{b}$
        Concatenate $\vec{a}$ *to* $\mathbf{M}_i$*, and* $\vec{b}$ *to* $\mathbf{C}_i$
        $p++$
    $i++$
return all $\mathbf{M}_i$'s and all $\mathbf{C}_i$'s

For each bus with renewables integration, the pair of slope matrix $\mathbf{M}_i$ and bias matrix $\mathbf{C}_i$ forms the set of linearly approximated LVRT constraints. The union of $\mathbf{M}_i$'s and $\mathbf{C}_i$'s thus forms the complete LVRT constraints in the ACFR.

Taking the Kundur 9-bus/3-generator system[74] as an example, the FR specified by only the convex constraints is shown in Figure. 26. Since there are three generators, the rotor angle differences between either two of them have the number of three. They are limited within $\frac{\pi}{2}$ which makes the FR a cube in the rotor angle difference space.

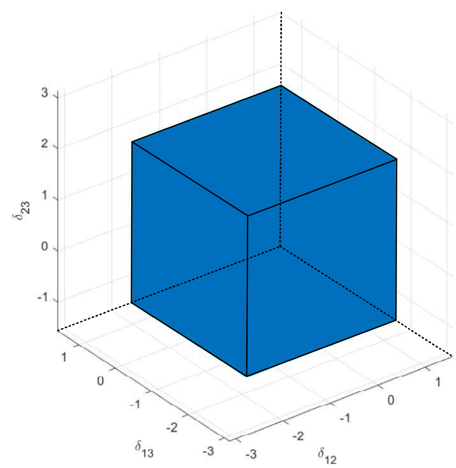

Figure. 26. Bounded phase angles difference polytope.

Considering original LVRT constraints with cosine terms, the LVRT constant is set to be 0.85, the feasibility region is shown in Figure. 27.

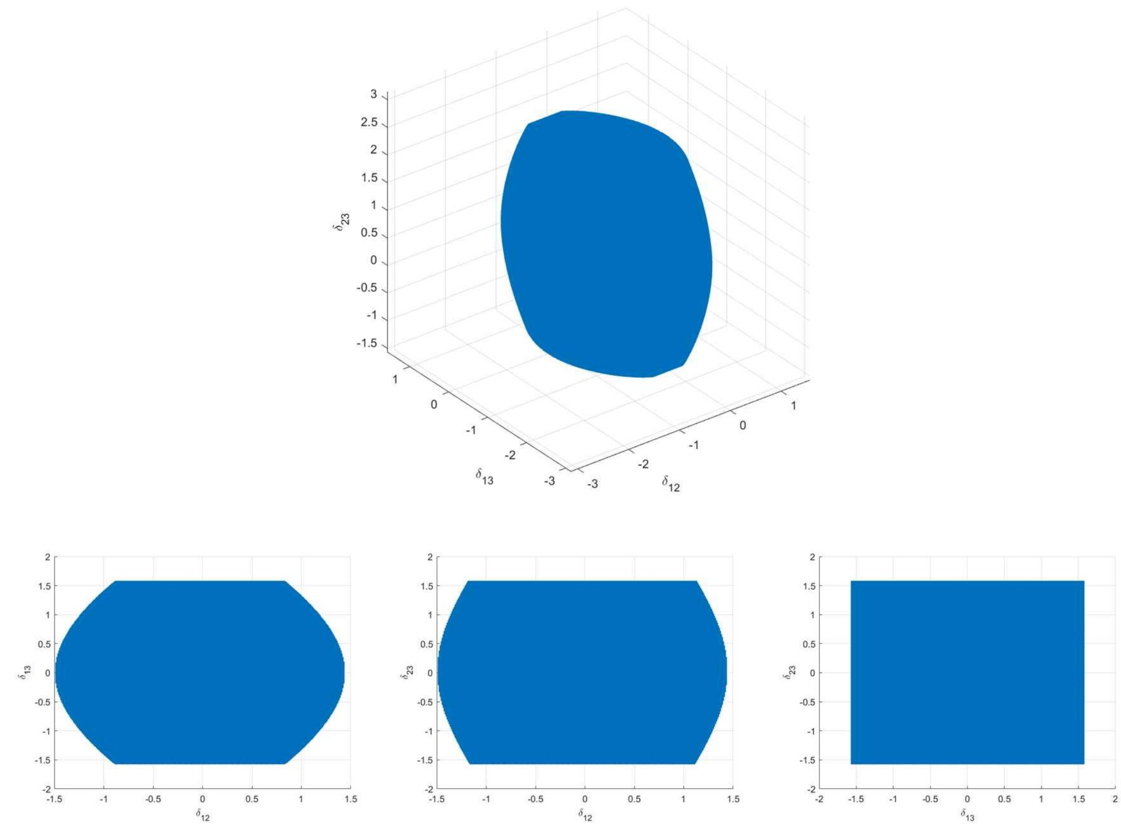

Figure. 27. Feasibility region considering LVRT in cosine form.

With the same LVRT constant, the ACFR reached with the previous algorithm is shown in Figure. 28. In order to provide a better idea of how the LVRT constraint will change with the constant, the ACFR with LVRT constant to be 0.9 is shown in Figure. 29. It can be seen that along with the increase of LVRT constant which is equivalent to raise the LVRT curve, the FR covers a smaller region in the space which matches the case in the real world.

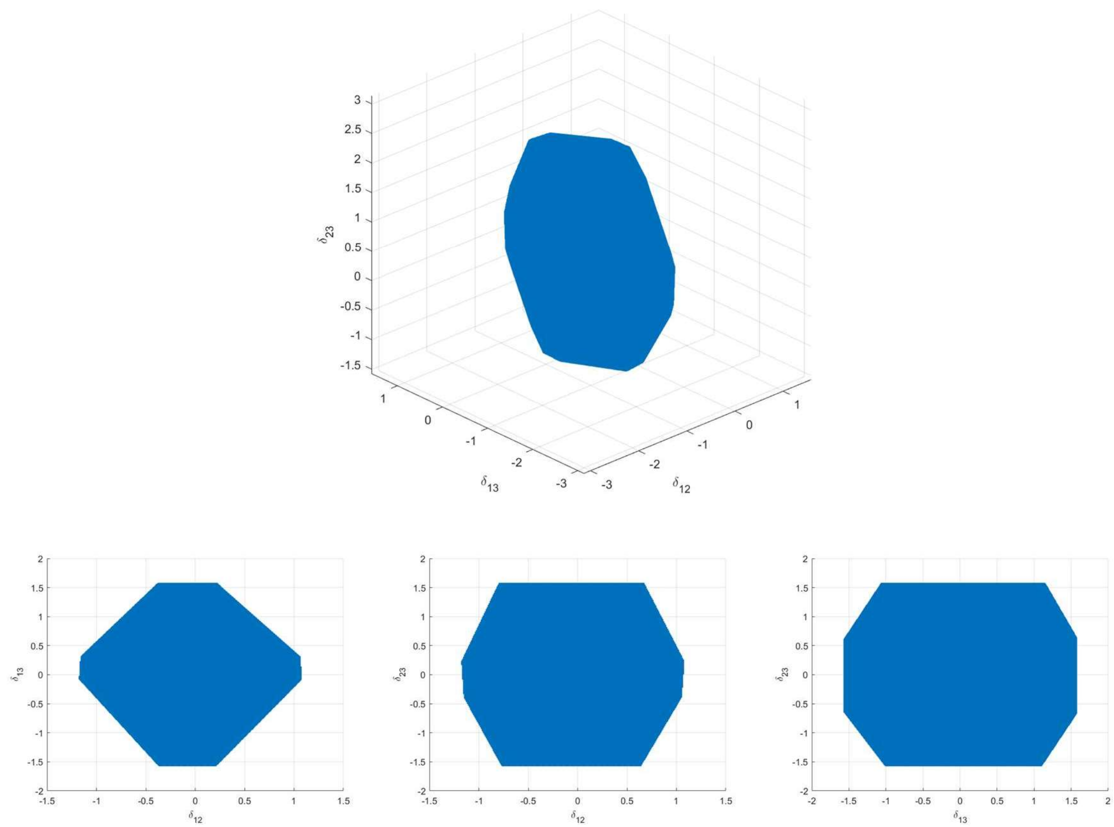

Figure. 28. Feasibility region considering LVRT in linearized form.

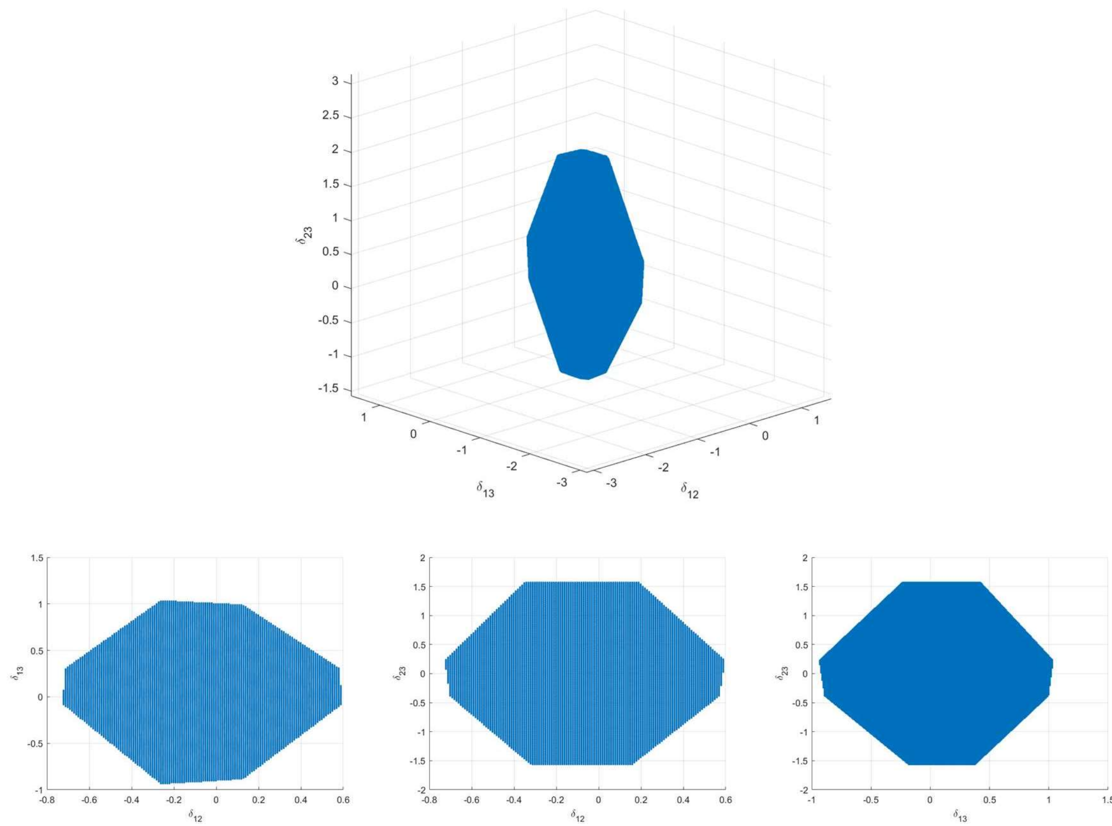

Figure. 29. Feasibility region considering LVRT in linearized form with 0.9 constant.

With these linearized LVRT constraints, the FR and relevant level set optimization problem formulation in the CSR estimation process considering these can be further specified. The feasibility region expressed with linear inequalities is shown in (4-97).

$$\begin{bmatrix} \begin{matrix} \vdots \\ \mathbf{M}_i \\ \vdots \end{matrix} \\ \begin{matrix} 1 & & \underline{0} \\ & \ddots & \\ \underline{0} & & 1 \end{matrix} \\ \begin{matrix} -1 & & \underline{0} \\ & \ddots & \\ \underline{0} & & -1 \end{matrix} \end{bmatrix} \begin{bmatrix} \vdots \\ \delta_{kj} \\ \vdots \end{bmatrix} + \begin{bmatrix} \begin{matrix} \vdots \\ \mathbf{c}_i^{row} + C_{sep} - V_{LVRT,\max} \\ \vdots \end{matrix} \\ \begin{matrix} \vdots \\ \frac{\pi}{2} \\ \vdots \end{matrix} \\ \begin{matrix} \vdots \\ \frac{\pi}{2} \\ \vdots \end{matrix} \end{bmatrix} \ge 0 \qquad (4\text{-}97)$$

where $i \in \{\text{PV buses}\}$.

In state space, the constraints are as following

$$-\begin{bmatrix} \begin{matrix} \vdots \\ \mathbf{M}_i \\ \vdots \end{matrix} & \begin{matrix} \ddots & \vdots & \\ \cdots & \underline{0} & \cdots \\ & \vdots & \ddots \end{matrix} \\ \begin{matrix} 1 & & \underline{0} \\ & \ddots & \\ \underline{0} & & 1 \end{matrix} & \begin{matrix} \ddots & \vdots & \\ \cdots & \underline{0} & \cdots \\ & \vdots & \ddots \end{matrix} \\ \begin{matrix} -1 & & \underline{0} \\ & \ddots & \\ \underline{0} & & -1 \end{matrix} & \begin{matrix} \ddots & \vdots & \\ \cdots & \underline{0} & \cdots \\ & \vdots & \ddots \end{matrix} \end{bmatrix} \begin{bmatrix} \begin{matrix} \vdots \\ \delta_{kj} \\ \vdots \end{matrix} \\ \begin{matrix} \vdots \\ \dot{\delta}_{kj} \\ \vdots \end{matrix} \end{bmatrix} - \begin{bmatrix} \begin{matrix} \vdots \\ \mathbf{c}_i^{row} + C_{sep} - V_{LVRT,\max} \\ \vdots \end{matrix} \\ \begin{matrix} \vdots \\ \frac{\pi}{2} \\ \vdots \end{matrix} \\ \begin{matrix} \vdots \\ \frac{\pi}{2} \\ \vdots \end{matrix} \end{bmatrix} \le 0 \qquad (4\text{-}98)$$

Further

$$-\begin{bmatrix} \boxed{\begin{matrix}\vdots\\ \mathbf{M}_i\\ \vdots\end{matrix}} & \boxed{\begin{matrix}\ddots & \vdots & \iddots\\ \cdots & \underline{0} & \cdots \\ \iddots & \vdots & \ddots\end{matrix}} \\ \boxed{\begin{matrix}1 & & \underline{0}\\ & \ddots & \\ \underline{0} & & 1\end{matrix}} & \boxed{\begin{matrix}\ddots & \vdots & \iddots\\ \cdots & \underline{0} & \cdots \\ \iddots & \vdots & \ddots\end{matrix}} \\ \boxed{\begin{matrix}-1 & & \underline{0}\\ & \ddots & \\ \underline{0} & & -1\end{matrix}} & \boxed{\begin{matrix}\ddots & \vdots & \iddots\\ \cdots & \underline{0} & \cdots \\ \iddots & \vdots & \ddots\end{matrix}} \end{bmatrix} \begin{bmatrix}\mathbf{L} & \mathbf{0}\end{bmatrix} \begin{bmatrix}\mathbf{x}_1\\ \mathbf{x}_2\end{bmatrix} - \begin{bmatrix} \boxed{\begin{matrix}\vdots\\ \mathbf{c}_i^{row} + C_{sep} - V_{LVRT,\max}\\ \vdots\end{matrix}} \\ \boxed{\begin{matrix}\vdots\\ \dfrac{\pi}{2}\\ \vdots\end{matrix}} \\ \boxed{\begin{matrix}\vdots\\ \dfrac{\pi}{2}\\ \vdots\end{matrix}} \end{bmatrix} \le 0 \qquad \text{(4-99)}$$

Therefore, there are three types of sub-optimization problems corresponding to linearized LVRT constraints, angle differences smaller than $\frac{\pi}{2}$, and angle differences larger than $-\frac{\pi}{2}$, respectively.

For each LVRT constraints, take the jth one as an example. Assume the jth linear inequality has the slope vector $\mathbf{a}_j = [a_1 \quad \cdots \quad a_{n(n-1)/2}]$ which is the jth row of the first matrix in LHS in (4-99) and the corresponding bias constant b_j which is the jth entry of the constant vector in LHS in (4-99). The corresponding equivalent sub-problem is composed as follows:

$$\eta_j(v) = \{\exists \mathbf{x}\}$$

$$s.t. \qquad \max\ \mathbf{a}_j [\mathbf{0} \quad \mathbf{L}]\mathbf{x} \le 0$$

$$\mathbf{a}_j [\mathbf{L} \quad \mathbf{0}]\mathbf{x} + b_j = 0$$

$$-\begin{bmatrix} \boxed{\begin{matrix} \vdots \\ \mathbf{a}_{j-1} \\ \mathbf{a}_{j+1} \\ \vdots \end{matrix}} \\ \boxed{\begin{matrix} 1 & & \underline{0} \\ & \ddots & \\ \underline{0} & & 1 \end{matrix}} \\ \boxed{\begin{matrix} -1 & & \underline{0} \\ & \ddots & \\ \underline{0} & & -1 \end{matrix}} \end{bmatrix} [\mathbf{L} \quad \mathbf{0}]\mathbf{x} - \begin{bmatrix} \boxed{\begin{matrix} \vdots \\ b_{j-1} \\ b_{j+1} \\ \vdots \end{matrix}} \\ \boxed{\begin{matrix} \vdots \\ \frac{\pi}{2} \\ \vdots \end{matrix}} \\ \boxed{\begin{matrix} \vdots \\ \frac{\pi}{2} \\ \vdots \end{matrix}} \end{bmatrix} \le 0 \tag{4-100}$$

$$V(\mathbf{x}) < v$$

For each bounded phase angle difference constraint, one particular δ_{kj} is picked to be $\frac{\pi}{2}$ (or $-\frac{\pi}{2}$).

Take $\delta_{kj} = \frac{\pi}{2}$, the sub-problem is turned into

$$\phi_{kj}(v) = \{\exists \mathbf{x}\}$$

s.t. $$\max \ \dot{\delta}_{kj} \le 0$$

$$\delta_{kj} = \frac{\pi}{2}$$

$$-\begin{bmatrix} \boxed{\begin{matrix} \vdots \\ \mathbf{M}_i \\ \vdots \end{matrix}} & \boxed{\begin{matrix} \ddots & \vdots & \iddots \\ \cdots & \underline{0} & \cdots \\ \iddots & \vdots & \ddots \end{matrix}} \\ \boxed{\begin{matrix} 1 & & \underline{0} \\ & \ddots & \\ \underline{0} & & 1 \end{matrix}} & \boxed{\begin{matrix} \ddots & \vdots & \iddots \\ \cdots & \underline{0} & \cdots \\ \iddots & \vdots & \ddots \end{matrix}} \\ \boxed{\begin{matrix} -1 & & \underline{0} \\ & \ddots & \\ \underline{0} & & -1 \end{matrix}} & \boxed{\begin{matrix} \ddots & \vdots & \iddots \\ \cdots & \underline{0} & \cdots \\ \iddots & \vdots & \ddots \end{matrix}} \end{bmatrix} \begin{bmatrix} \mathbf{L} & \mathbf{0} \end{bmatrix} \begin{bmatrix} \mathbf{x}_1 \\ \mathbf{x}_2 \end{bmatrix} - \begin{bmatrix} \boxed{\begin{matrix} \vdots \\ \mathbf{c}_i^{row} + C_{sep} - V_{LVRT,\max} \\ \vdots \end{matrix}} \\ \boxed{\begin{matrix} \vdots \\ \frac{\pi}{2} \\ \vdots \end{matrix}} \\ \boxed{\begin{matrix} \vdots \\ \frac{\pi}{2} \\ \vdots \end{matrix}} \end{bmatrix} \le 0 \qquad (4\text{-}101)$$

$$V(\mathbf{x}) < v$$

Besides, take $\delta_{kj} = -\frac{\pi}{2}$

$$
\begin{gathered}
\gamma_{kj}(v)=\{\exists\,\mathbf{x}\} \\
s.t. \qquad \max\ -\dot{\delta}_{kj}\le 0 \\
\delta_{kj}=-\frac{\pi}{2} \\
-\begin{bmatrix}
\boxed{\begin{matrix}\vdots\\ \mathbf{M}_i\\ \vdots\end{matrix}} & \boxed{\begin{matrix}\ddots & \vdots & \iddots\\ \cdots & \underline{0} & \cdots\\ \iddots & \vdots & \ddots\end{matrix}} \\
\boxed{\begin{matrix}1 & & \underline{0}\\ & \ddots & \\ \underline{0} & & 1\end{matrix}} & \boxed{\begin{matrix}\ddots & \vdots & \iddots\\ \cdots & \underline{0} & \cdots\\ \iddots & \vdots & \ddots\end{matrix}} \\
\boxed{\begin{matrix}-1 & & \underline{0}\\ & \ddots & \\ \underline{0} & & -1\end{matrix}} & \boxed{\begin{matrix}\ddots & \vdots & \iddots\\ \cdots & \underline{0} & \cdots\\ \iddots & \vdots & \ddots\end{matrix}}
\end{bmatrix}
\begin{bmatrix}\mathbf{L} & \mathbf{0}\end{bmatrix}
\begin{bmatrix}\mathbf{x}_1\\ \mathbf{x}_2\end{bmatrix}
-\begin{bmatrix}
\boxed{\begin{matrix}\vdots\\ \mathbf{c}_i^{row}+C_{sep}-V_{LVRT,\max}\\ \vdots\end{matrix}} \\
\boxed{\begin{matrix}\vdots\\ \frac{\pi}{2}\\ \vdots\end{matrix}} \\
\boxed{\begin{matrix}\vdots\\ \frac{\pi}{2}\\ \vdots\end{matrix}}
\end{bmatrix}\le 0 \\
V(\mathbf{x})<v
\end{gathered}
\tag{4-102}
$$

Within the optimization process, the linear search method is used to the level-set value of the current Lyapunov function. For each v, the states should be constrained by the three types of sub-optimization problems listed. The complete optimization problem is formed up as following:

$$
\boxed{
\begin{array}{ll}
 & V_{\max}^{convex}=\max v \\
s.t. & \boxed{\eta_j(v)\neq \text{true}} \\
 & \vdots \\
 & \boxed{\eta_j(v)\neq \text{true}} \\
 & \vdots \\
 & \boxed{\gamma_{kj}(v)\neq \text{true}} \\
 & \vdots
\end{array}
}
\tag{4-103}
$$

4.6 Case Study

The study case used to demonstrate the effectiveness of the proposed method is a 2-machine 3-bus demo system. The network model can be seen in Figure. 30. The reason for using a 2-machine system is that in COA frame the state space becomes 2D making it possible to visualize the CSR. The method can be easily implemented on larger scale systems. The maximum LVRT constant is set to be 0.9 and $V_{LVRT,\max} = (0.9)^2$. The fault being assessed is a three-phase-to-ground fault between bus 1 and bus 2. We ran the fault trajectory for 2 seconds which is the maximum fault clearing time that we wanted to study and then tried to estimate a stability region that could contain the end point of this trajectory. In doing so, we tried to maximize the overlap of the fault trajectory with the post-fault systems stability region estimate which can provide a less conservative estimate of the critical clearing time.

The CSR estimation results can be seen in the following figures. In Figure. 31, we start by using the Energy function as a starting candidate $V_{initial}(\mathbf{x})$ for optimal $V(\mathbf{x})$. As we start expanding its level set, the expansion stops as soon as it hits the edge of the flow out portion on the right, yielding

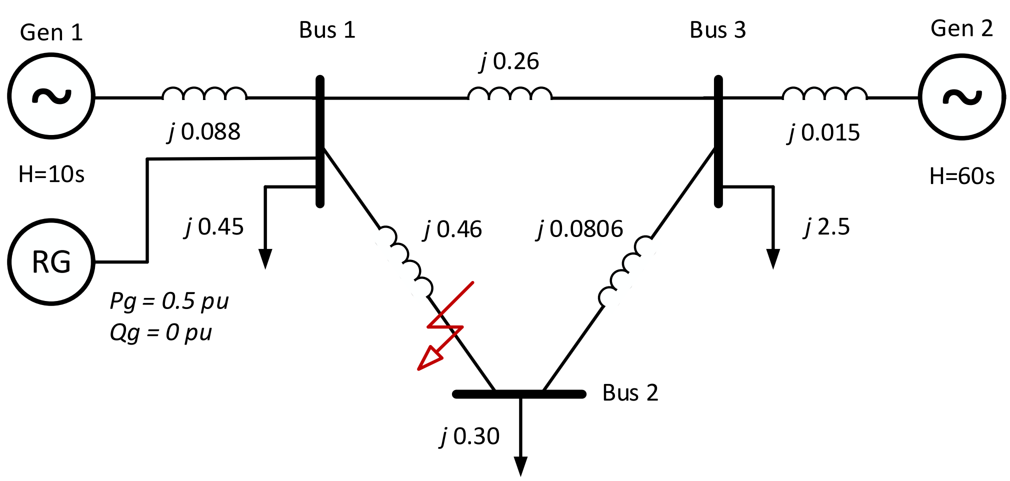

Figure. 30. 2-machine 3-bus Study Case Diagram

the region marked in blue. This level-set is positively invariant, i.e. a valid estimate. The orange arrows in the figure show the vector field of the post-fault system, which is indicated as 'Vector Filed Direction' in the legend. The system trajectory starting from the post-fault initial state $\mathbf{x}_0$ is shown with the dark green curve. Also shown are the boundaries of the original (black lines) and the polytopic approximation (green lines) of the LVRT constrained FR. The region for convexity of V are shown with red lines, which is basically the $\pi/2$ constraints on rotor angle differences. It is easy to see that in this system, the LVRT constraints are more binding and therefore the ACFR is basically the same as LVRT constrained FR. The flow out portions of the corresponding ACFB are marked in grey dashed lines. These can be visually verified through the direction of the vector field in its vicinity. Using the conventional energy function, the post-fault initial state cannot be included into the estimated CSR (blue circle). Therefore, the system stability cannot be certified.

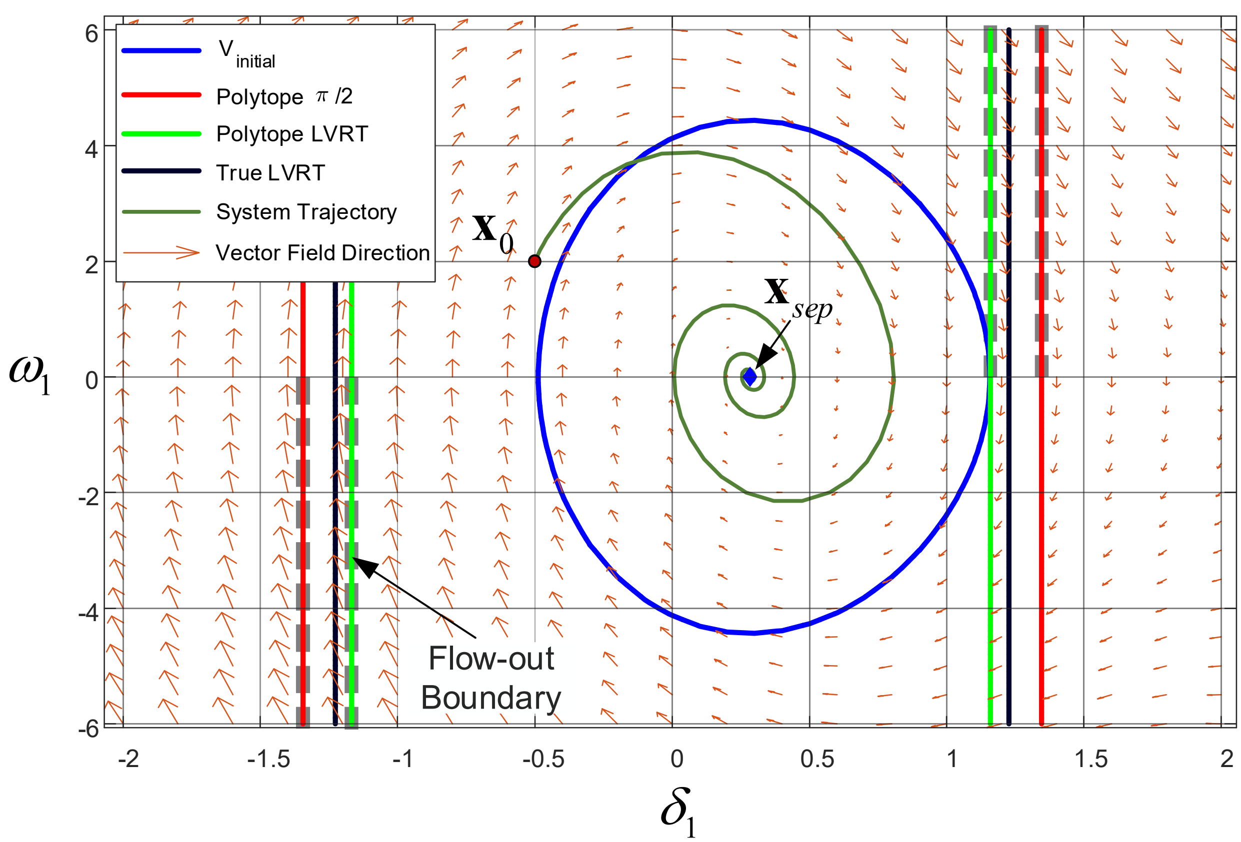

Figure. 31. Estimated Stability Region with Conventional Energy Function

As the iterative estimation process goes, it can be observed in Figure. 32 that the level-set reached by the second Lyapunov function $V_2(\mathbf{x})$ is more biased towards the binding LVRT constraint and more customized to the post-fault initial state and corresponding system trajectory. Part of the level-set envelops only flow-in part of FB. The estimated CSR is the intersecting region inside the level set and the binding ACFB. Compared to $V_{initial}(\mathbf{x})$ (energy function), the successive CSR estimates enclose a larger area of the relevant portion of the state space. The second Lyapunov function expands beyond the first one engulfing the flow-in portion of the ACFB on the right-hand side. For the fault under study, this estimate encloses a longer portion of the sustained fault trajectory and therefore the critical clearing time estimate which is the time it takes to exit this region will be less conservative. The system stability is also certified by including the post-fault initial state inside the level set.

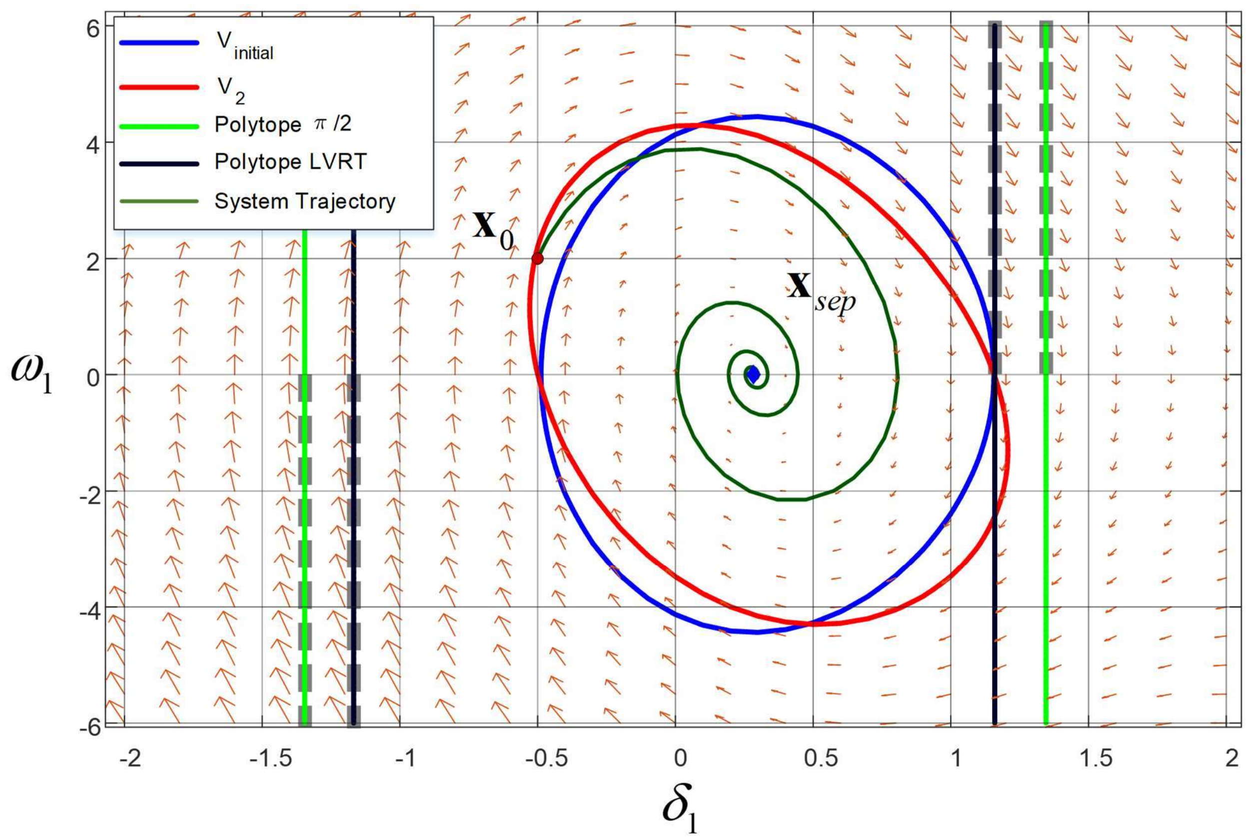

Figure. 32. Estimated Stability Region with Proposed Method

The two Lyapunov functions' values distributions are demonstrated in Figure. and Figure. to provide a clear idea about the variation along with the iterative process. The absolute values of these three function make no sense when they are compared with each other because these values are only meaningful when considered with respect to the particular concerned Lyapunov function and are used for reaching the shape and covering an area of SR to be estimated.

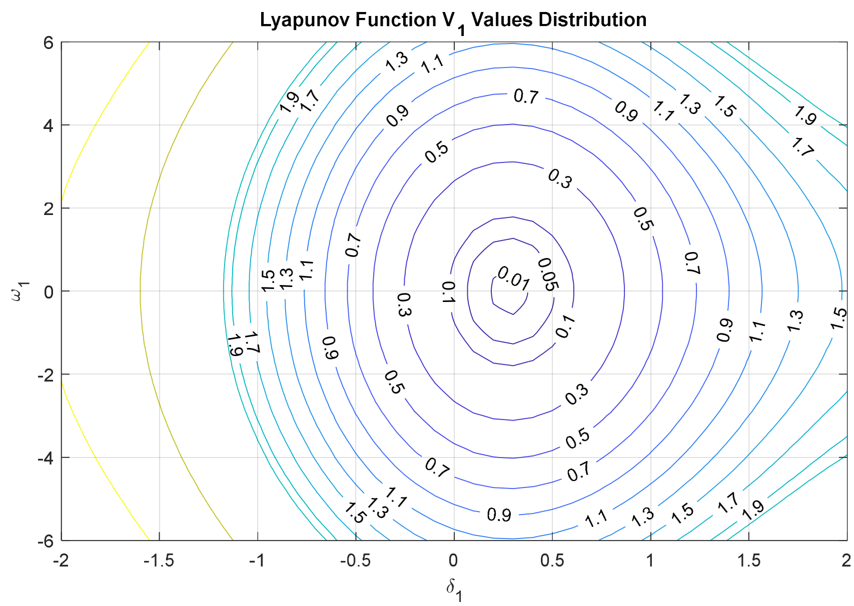

Figure. 33. Lyapunov Function V1($V_{initial}(\mathbf{x})$) Values Distribution

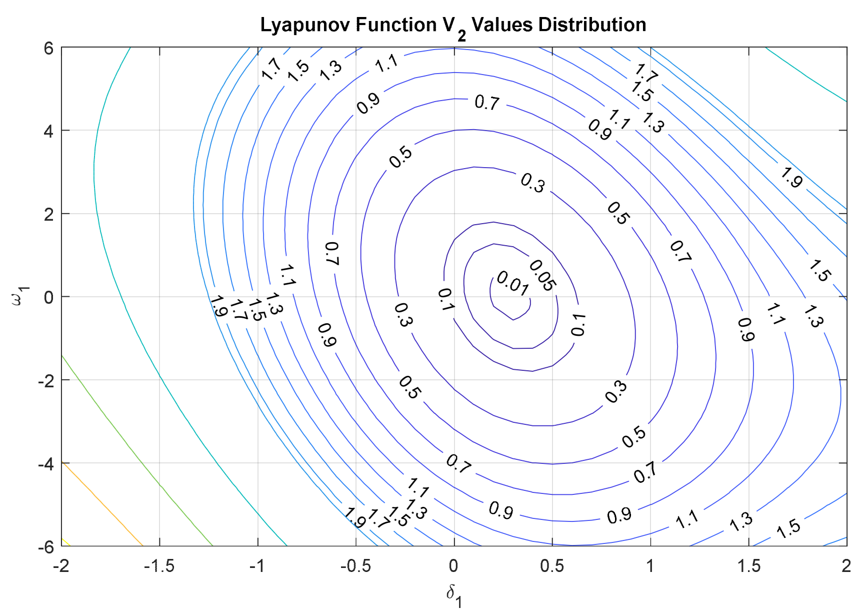

Figure. 34. Lyapunov Function V2 Values Distribution

For comparison, the CSR estimation without considering the LVRT constraints are shown in the Figure. 35. It can be easily seen that without the operation limits on RES integrated buses, the CSR is larger than the estimated results before.

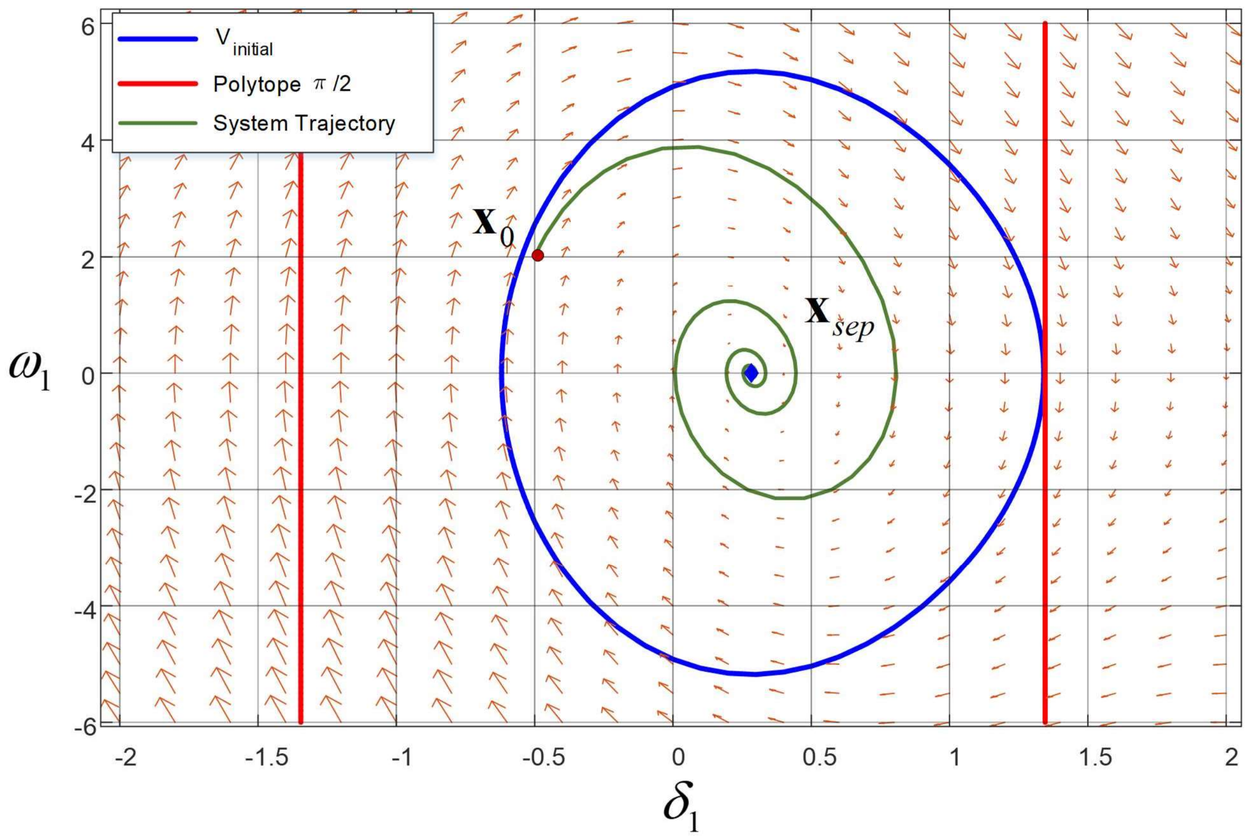

Figure. 35. Estimated Stability Region with Proposed Method

4.7 Discussions

In this paper, the transient stability region of an LVRT constrained power system is estimated using the LFF method combined with a convex approximation of the FR. LVRT constraints are first derived in terms of generator rotor angles. Then, the FR considering both LVRT and convexity of Lyapunov function candidates is optimally approximated with a polytope for convexity of the CSR estimation problem. Finally, Lyapunov functions in COA frame found through solving some LMIs are used to estimate the CSR. The method's effectiveness is demonstrated on a 2-machine 3-bus lossless test case. The proposed method is a good first step for capturing the instabilities arising from tripping of such generation during system disturbances as more RGs are integrated into power systems.

For future work, we will be exploring the applicability of this approach to more detailed power system models. There are no theoretical roadblocks in doing so.

CHAPTER 5. ADAPTIVE LVRT CONTROL CONSIDERING SYSTEM VOLTAGE SECURITY

5.1 Introduction

Low Voltage Ride Through is an effective mechanism for maintaining power system stability and security. With continuous increasing renewable energy sources integrated into the modern power system, this mechanism is gaining more and more significance. The main reason is that along with more flexibility brought by the renewable energy sources, there are also more complex dynamics caused by tripping actions triggered by the violation of the LVRT operation constraints on them[75]. The tripping of these power supplies further endanger the voltage security of the system. The required load margin for system secure operation is also more difficult to satisfy.

The conventional LVRT criterions are defined by the widely recognized standards, regulatory agencies, and/or equipment producers, which is a general operation limit. The system takes them as hard requirements and if the voltage on the corresponding bus is lower than the LVRT curve, the renewable energy source will be tripped instantaneously no matter whether the disturbance on the system will influence the source or not. This is obviously a conservative scheme to deal with these scenarios. However, there have not been researches attempting to cope with this conservativeness for renewables energy sources operating from the system perspective. Most of the studies focus on finding more adaptive control schemes for detailed converter-interfaced devices which takes the LVRT curves as a fixed reference. Researchers in [76] try to find the optimized control scheme so that the renewable energy source will not violate the LVRT constraint under certain disturbances.

In this chapter, a method to adaptively adjust the LVRT curves of the renewable energy sources in the system is proposed to find the optimal the tripping settings, so that the load margin requirement can be satisfied and the system with high renewables penetration can operate in a much less conservative way.

5.2 Power System Disturbances and Load Margin

Load margin plays an important role in power electric utilities' assessment of system voltage security. Generally, the utility will set up a lower limit on this margin, which indicates the minimum required load pick-up capability of the system before it reaches the non-converging or voltage collapse operation points. This also serves as a criterion on system planning[77] and operation.

The increasing penetration of renewable energy sources brings more uncertainty and difficulty to the system to satisfy this operation limit. As is well known, the increase of load in the system can bring more pressure to the system on maintaining voltage stability. Or to be more specific, with the energy demand rising and the less responsive reaction of supplies, the system will very possibly face low voltage issues. The renewable energy sources might suffer from these low voltages and be tripped off-line if exceed the predefined LVRT constraints. Losing these energy sources causes insufficient power supply which further sabotages system voltage stability and make the load margin criterion much harder to be reached.

The LVRT constraints on renewables energy sources are necessary though. These limits on the integration of these sources help to reduce the possibility that the sources passively participate in or feed the faults under the circumstances where the low voltage scenarios are brought by local disturbances. Take the disturbance shown in Figure. 36 as an example. The fault happens within

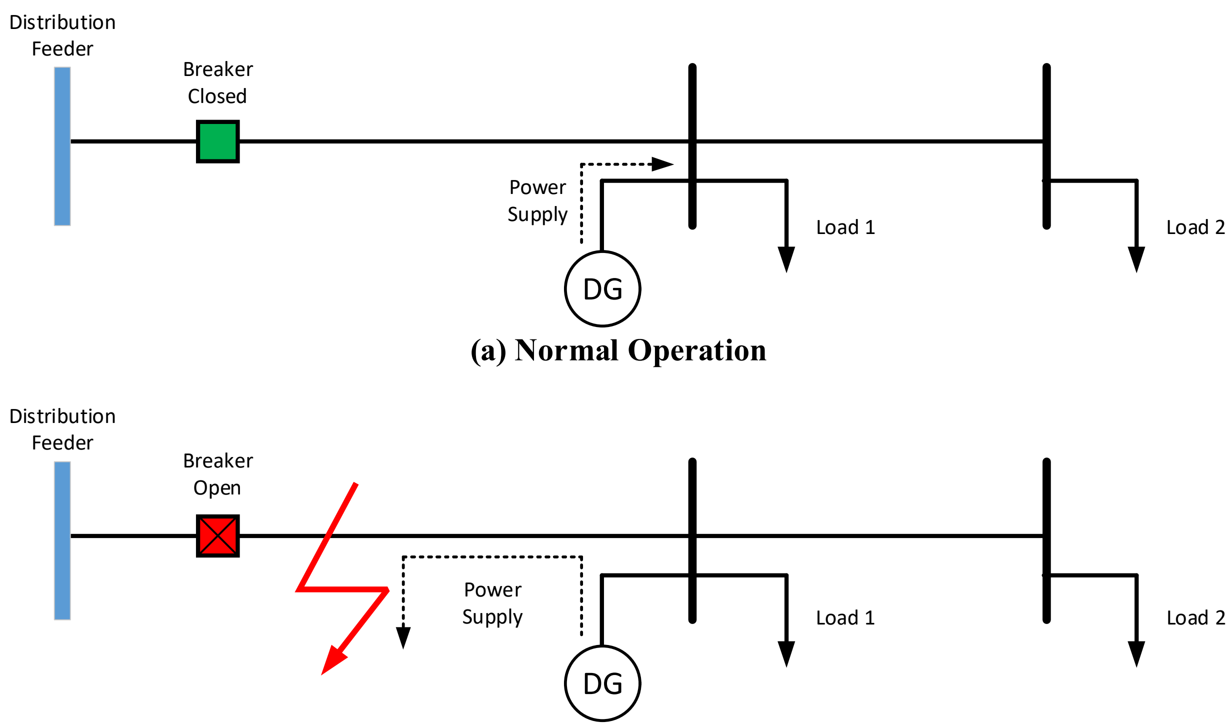

(a) Normal Operation

(b) Fault Happens

Figure. 36. Renewable Energy Sources Impacts under Distribution Level Disturbances

the low voltages side of the feeder where most of the renewable energy sources are integrated into the system. As the protection installed mainly acts to isolate the faults from the high voltage side, the renewable sources may still be feeding the fault after the relay functions which may cause a significant problem to distribution system operation. Therefore, the LVRT mechanism makes the judgment based on the corresponding bus voltage profile and actively trip the renewable source off-line, which prevents the situation from deterioration and provide a positive contribution to system restabilization under disturbances.

However, if the fault happens on the transmission system as shown in Figure. 37, which may also cause low voltage scenarios, the tripping of renewable energy sources because of exceeding LVRT constraints might not only do hardly any help to preventing exacerbation of the fault's negative impacts but lose quite an amount of power supply and make it more difficult to satisfy the load

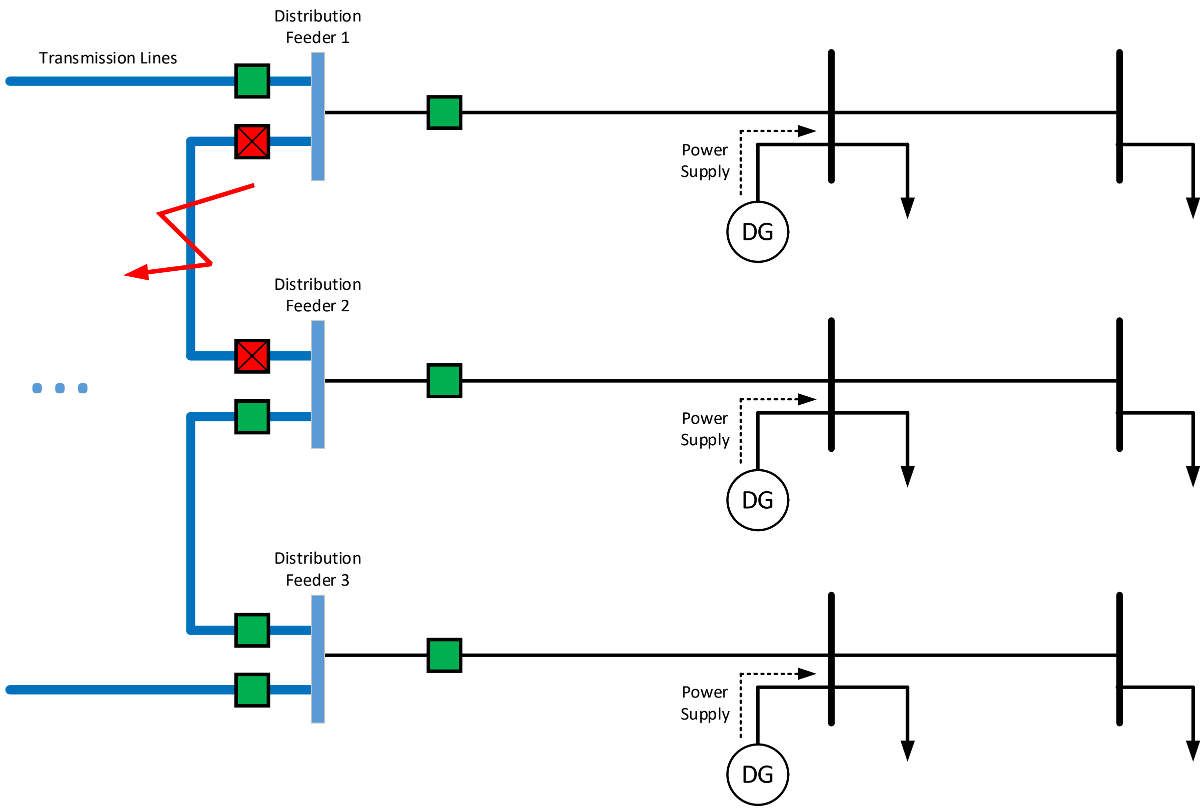

Figure. 37. Renewable Energy Sources Impacts under Transmission Level Disturbances

margin. Therefore, a method to adaptively adjust the LVRT curve itself would be useful to prevent the system from abandoning large quantity of renewable energy and reduce the unnecessary dynamic brought by the tripping actions of these renewable energy sources in the system.

5.3 System Operation Simulation Considering Renewables Tripping Using Continuation Power Flow

The continuation power flow (CPF) is an effective method to demonstrate the system's capability to maintain voltage stable with increasing load on the buses. It can track the system's operation states along with the proportional increase of the loads in the system. These typical traces can be demonstrated with the P-V curve of the certain bus in the system as is shown in Figure. 38.

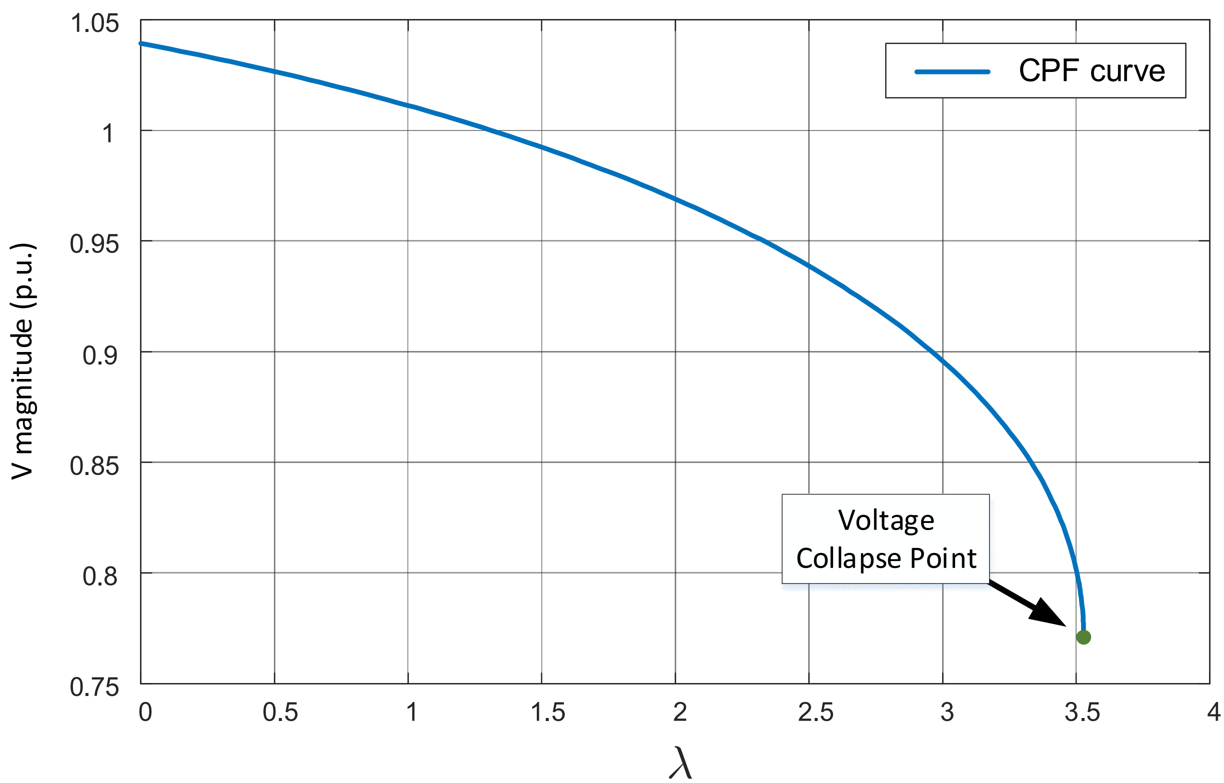

Figure. 38. Example P-V (λ -V) Curve

As the load margin (λ) in the system is increased continuously, the voltage magnitudes on the buses are decreased accordingly. When the reduction finally exceeds the LVRT constraint, the corresponding renewable energy source is tripped off-line. Since the whole analysis is assessed in the steady state, the dynamic part within the LVRT curve is omitted and only the constant part within the LVRT curve after the disturbance is taken as the criterion. The tripping of the renewables certainly changes system status and topology. Therefore, the system will operate on a different track in terms of the P-V curve. Since the connection status of renewables is a discrete variable, this change of track looks more like a 'jump' from one curve to another in P-V space. Within the procedure to achieve the P-V curve considering the tripping of the RGs, the linear interpolation method [78] is used to find out the load margin at the point where the LVRT constant is reached. This is because that generally when the LVRT constraint breaking is realized by the CPF, it has already passed the load margin where the voltage on the concerned RG bus reaches the exact value of the LVRT constant. The equilibrium under the resulted load margin is searched by normal Newton-Raphson iterative method on the new curve which indicates the new system configuration after the tripping of the corresponding RG.

There are also cases where there is no equilibrium point when trying to jump to another curve. This is basically because that different curves have different load margins where voltages collapse. Generally, since there is a loss of power supply, namely RGs, when any jump occurs, the load margin at the voltage collapse point is to be reduced. Since there is no equilibrium, in order to help the system to continue function, the tripping action of the particular RG is blocked to maintain the system operation staying on the original curve. This RG is thus remained connected. The blocking of certain RGs in the system is also indicating that the LVRT constants of these RGs need to be adjusted, or specifically lower down to some extent. The aim of the work in this chapter is to find out an optimized set of RGs to be blocked from tripping so that the system's P-V curve can reach the specified load margin limit with minimum adjustment on the LVRT settings.

Take a 9-bus 3-RG system as an example. 3 RGs are installed on bus 5, 7, 9 respectively. The 'jumping' behaviors are shown in Figure. 39. The 'sol-1 0 1' in the legend indicates the P-V curve with the connection status of RGs to be that RG on bus 5 is connected, RG on bus 7 is not connected, and RG on bus 9 is connected.

To be more specific, with the load margin increases, the first RG that reaches its LVRT limit and is tripped offline is bus 9 and its LVRT limit is 0.9 p.u. The jumping behavior is pointed out as 'Jump 1' in Figure. 39 and more details are shown in Figure. 40 (a). It can be seen that the system jumps from the curve 'sol-1 1 1' to the curve 'sol-1 1 0'. The second RG that reaches its LVRT limit is bus 5 and the system jumps from the curve 'sol-1 1 0' to the curve 'sol-0 1 0' which is shown in Figure. 40 (b).

The example of the RG being blocked from tripping can be seen in Figure. 41. It can be seen that the RG on bus 7 reaches its LVRT constraint and is to be tripped, which means that the system tries to jump from the curve ‘sol-0 1 0’ to the curve ‘sol-0 0 0’. However, before the load margin where the RG to be tripped, the curve ‘sol-0 0 0’ has reached its nose point and the system with all three RGs tripped cannot reach the aforementioned load margin. In addition, the lower limit on load margin is yet satisfied. Therefore, the RG on bus 7 has to be maintained to be connected to allow the system to proceed for further checking on operation states under a larger load margin.

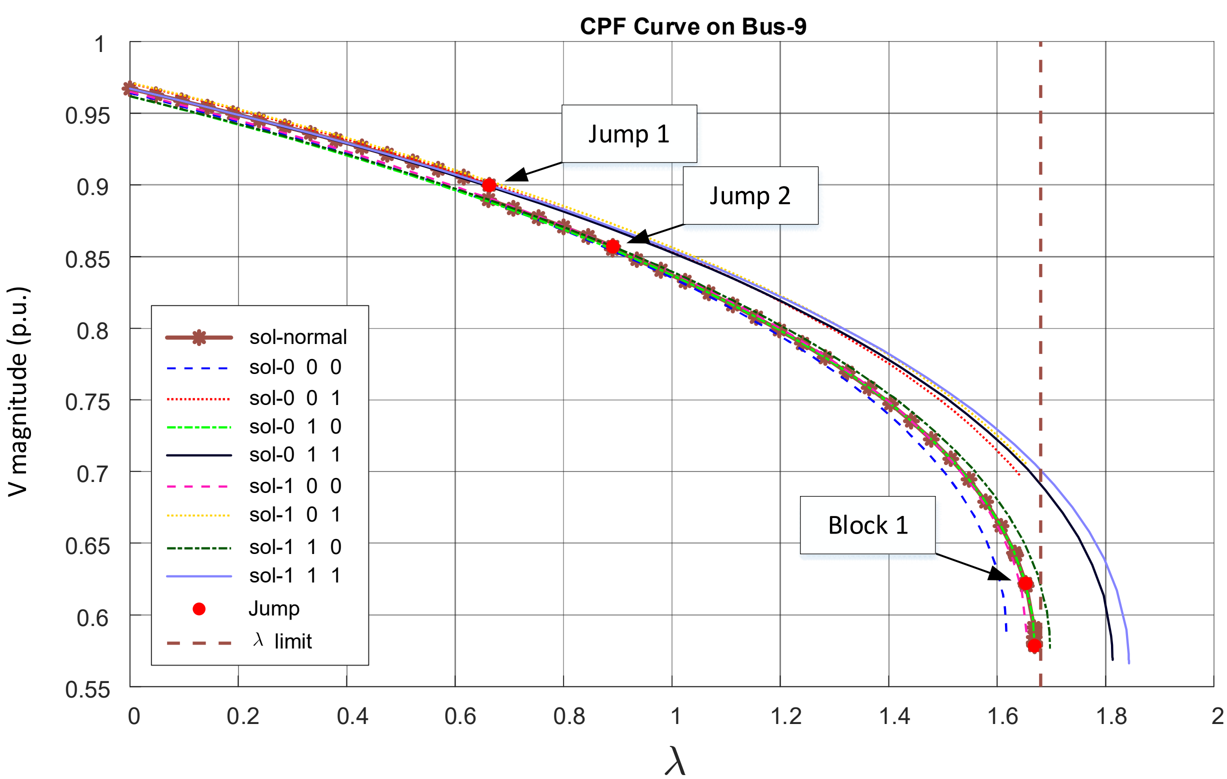

Figure. 39. Example of Jumping Behavior of System with DGs

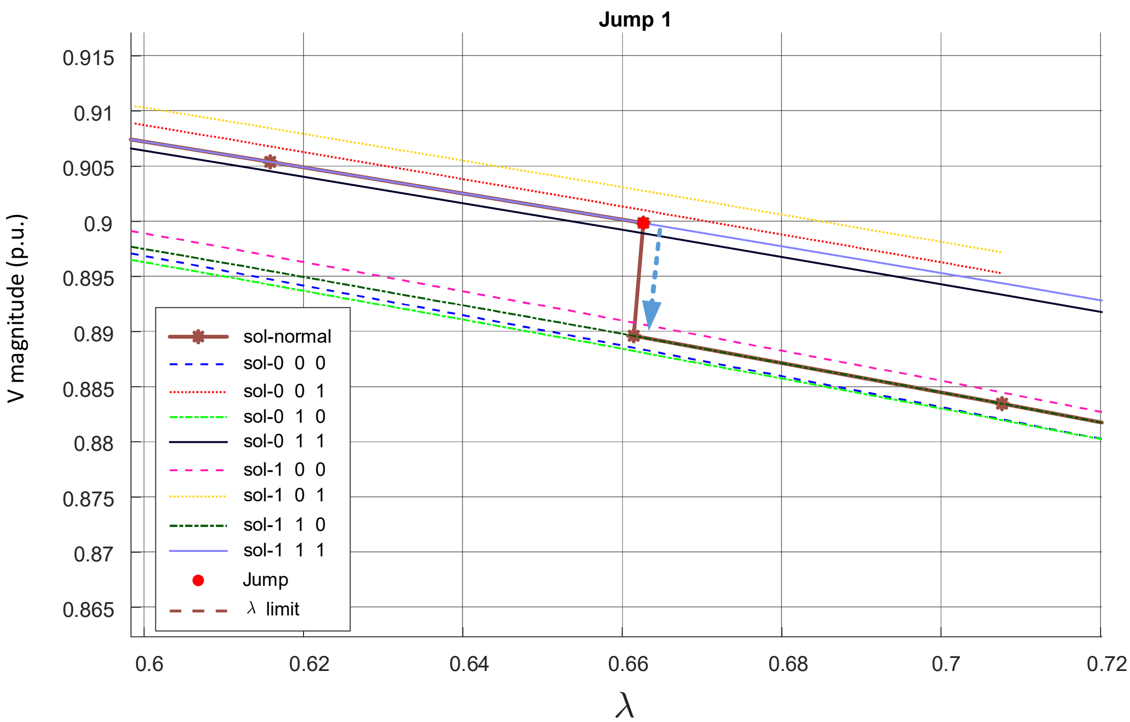

(a) Jump 1 From Curve sol-1 1 1 to sol-1 1 0

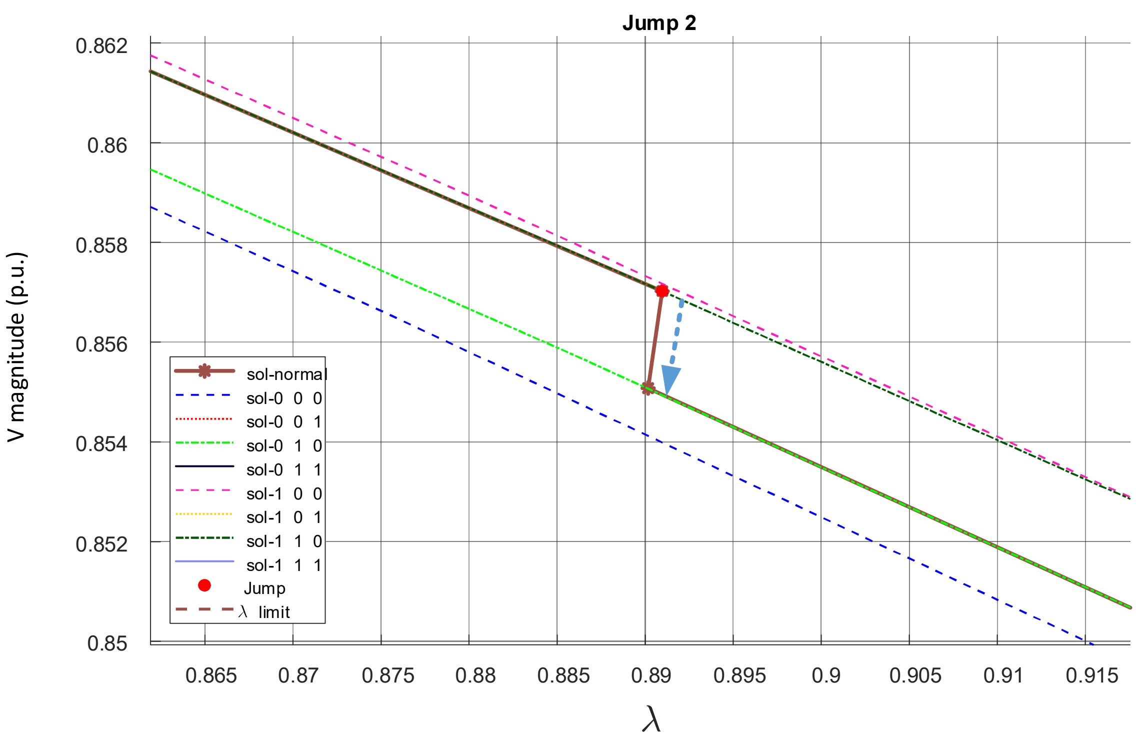

(b) Jump 2 From Curve sol-1 1 0 to sol-0 1 0

Figure. 40. Jump Behaviors Details

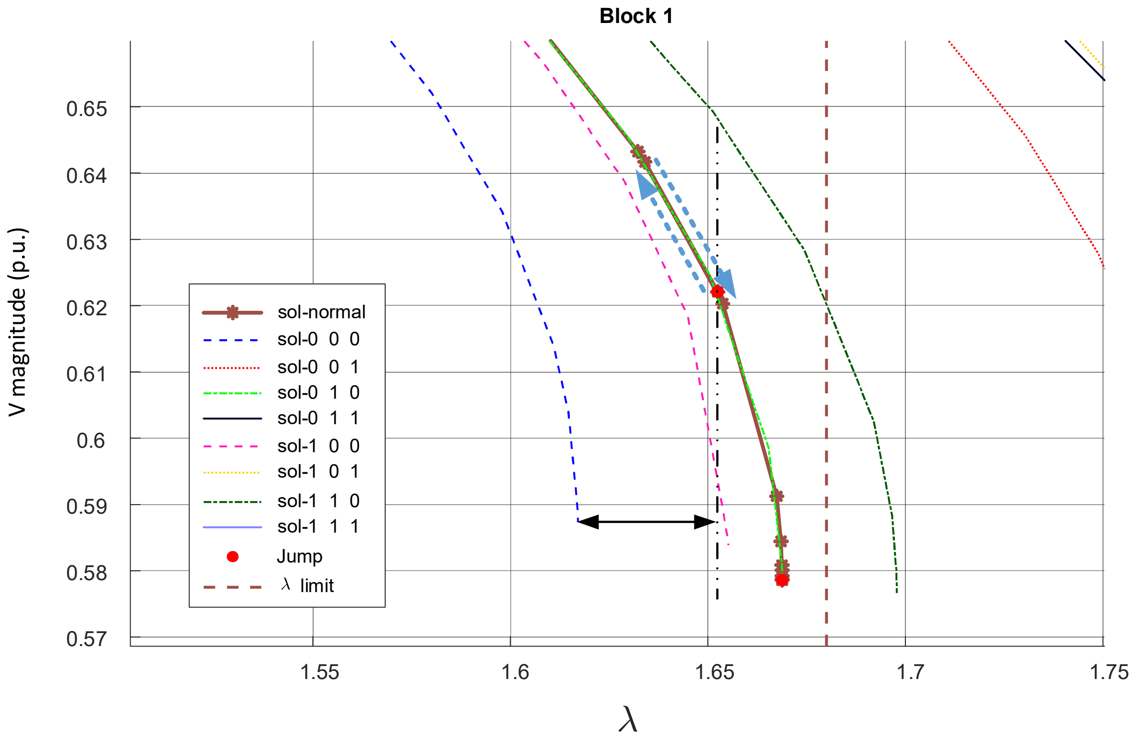

Figure. 41. Blocking Behaviors Details

5.4 Renewables Adaptive LVRT Optimization

As the RGs may be tripped off within the process of load margin increasing, it is harder for the system with large penetration of RGs to reach the load margin decided based on the topmost curve where all the RGs are assumed to be maintained online. Therefore, a method is proposed to adaptively adjust the LVRT settings of the relevant RGs, so that the system can still satisfy the predefined load margin limit. The first step is to identify the critical RGs in the system whose LVRT settings to be adjusted. Then the CPF is run based on the system where all the RGs remain their original LVRT settings, so they are tripped naturally when the bus voltages drop under the LVRT limit. The resulted P-V curve is used as a basis for further RGs settings adjustment. All the adjusting or non-adjusting combinations of the critical RGs are considered by estimating the load margin improvement upon the original P-V curve. Feasible combinations are selected to find out actual load margin improvement and detailed LVRT values to be adjusted. Finally, among these feasible solutions, the one with minimum adjustment to the LVRT settings of the RGs is selected as the optimization result.

5.4.1 Critical RGs Identification

The criticality of the RGs is identified based on their voltages at the load margin limit, λ_{limit}. Assuming that all the RGs remain online until the load margin is increased to λ_{limit}, the voltages of the corresponding buses are compared with their constant LVRT constraints. If the bus voltage is lower than the LVRT constant, the RG is more possible to be influenced by the load increase and thus has a chance to be tripped during system operation. Thus, it is necessary to consider adjusting its LVRT constant which may help to maintain the system to be on the upper P-V curve and to improve the load margin of the system. On the other hand, if the system has reached the pre-set load margin and the voltage of the corresponding RG is still higher than its LVRT limit, this means that this RG is less influenced by the load increase in the system, and thus less critical. There is also basically no need to consider adjusting this RG's LVRT constant.

However, for large scale systems, the CPF processing can be very much time consuming and less efficient. Therefore, a method to predict the voltage magnitudes on the P-V curve is proposed.

There have been several existing methods for voltage predictions. A typical method is proposed in [79] using auto-regressive based method and three complex voltage phasors to predict voltage phasors with larger load margin. The method formulation is as followings. The complex voltage phasor $V_i(\lambda) = V_{i,real} + jV_{i,imag}$ is assumed to be a quadratic function of the load margin λ :

$$V_i(\lambda) = a_i + b_i\lambda + c_i\lambda^2 \tag{5-1}$$

where, V_i indicates the voltage on bus i; a_i, b_i, and c_i are the corresponding parameters with bus i.

Therefore, using three known points $\left(V_i^{(1)},\ \lambda_1\right)$, $\left(V_i^{(2)},\ \lambda_2\right)$, $\left(V_i^{(3)},\ \lambda_3\right)$ on the designated P-V curve, it is easy to acquire the parameters with the following linear equations set:

$$\begin{bmatrix} V_i^{(1)}(\lambda_1) \\ V_i^{(2)}(\lambda_2) \\ V_i^{(3)}(\lambda_3) \end{bmatrix} = \begin{bmatrix} V_{i,real}^{(1)} + jV_{i,imag}^{(1)} \\ V_{i,real}^{(2)} + jV_{i,imag}^{(2)} \\ V_{i,real}^{(3)} + jV_{i,imag}^{(3)} \end{bmatrix} = \begin{bmatrix} 1 & \lambda_1 & \lambda_1^2 \\ 1 & \lambda_2 & \lambda_2^2 \\ 1 & \lambda_3 & \lambda_3^2 \end{bmatrix} \begin{bmatrix} a_i \\ b_i \\ c_i \end{bmatrix} \tag{5-2}$$

Take the IEEE 14 bus system as an example, assuming each load bus is equipped with one RG. The best and worst estimation results are shown in Figure. 42.

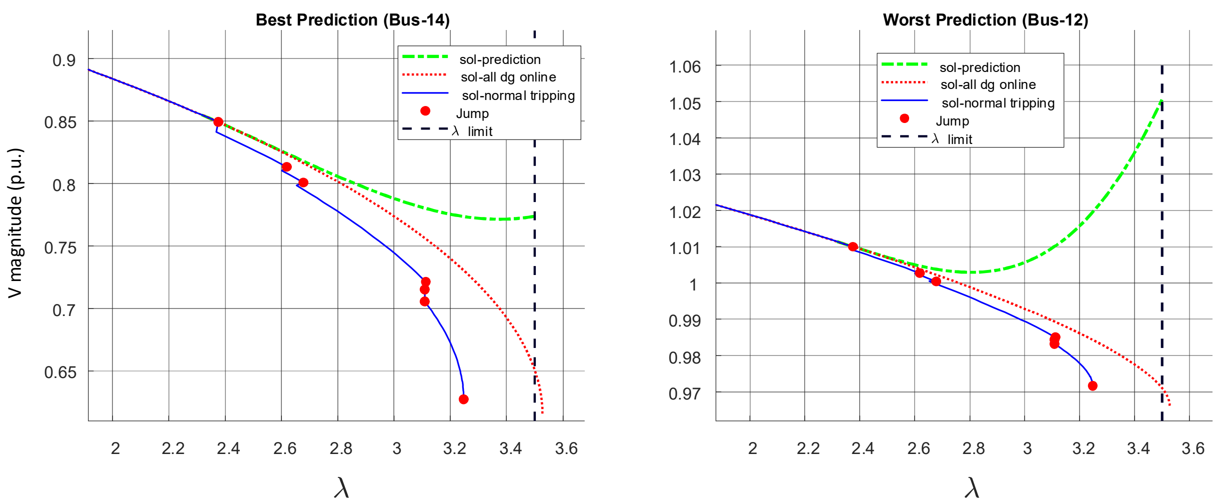

Figure. 42. Voltage Prediction Results – Auto Regression

The last three points before the jumping are taken as initial data for the auto-regression. This method performs well when it is far away from the nose point in the curve because of the closeness to linearity. However, as the λ_{limit} is closer to the nose point, the voltage prediction on the less linear part does not perform very well.

Another method proposed by Chiang, et al in [80] considers the non-linearity and uses a parabola to simulate the nose part of the P-V curve. However, this method needs the knowledge of the nose point to find the proper parabola function, which can be seen in its formulation as follows:

$$\begin{cases} \lambda_1 = \alpha_i + \beta_i V_i^{(1)} + \gamma_i \left(V_i^{(1)}\right)^2 \\ \lambda_2 = \alpha_i + \beta_i V_i^{(2)} + \gamma_i \left(V_i^{(2)}\right)^2 \\ \lambda_{nose} = \alpha_i + \beta_i V_i^{(nose)} + \gamma_i \left(V_i^{(nose)}\right)^2 \\ 0 = \beta_i + \gamma_i V_i^{(nose)} \end{cases} \tag{5-3}$$

where, the three parameters α_i, β_i, γ_i, and the voltage magnitude at the nose point $V_i^{(nose)}$ are unknown and to be found out; λ_1, λ_2 are the load margin values and $V_i^{(1)}$, $V_i^{(2)}$ are the voltage magnitudes of two points on the curve. The parabola approximation seems to be able to better simulate the non-linear part close to the nose point. However, there is no information about the nose point, which makes it impossible to know λ_{nose} before the processing. A modification is made to cope with it. The slope acquired with two points on the early part of the curve is used as the tangent of the linear part

$$\begin{cases} \lambda_{N_p-1} = \alpha_i + \beta_i V_i^{(N_p-1)} + \gamma_i \left(V_i^{(N_p-1)}\right)^2 \\ \lambda_{N_p} = \alpha_i + \beta_i V_i^{(N_p)} + \gamma_i \left(V_i^{(N_p)}\right)^2 \\ \dfrac{V_i^{(1)} - V_i^{(2)}}{\lambda_1 - \lambda_2} = \beta_i + \gamma_i V_i^{(1)} \end{cases} \tag{5-4}$$

where N_p refers to the number of the data points in the known part of the P-V curve; $\left(V_i^{(1)}, \lambda_1\right)$ and $\left(V_i^{(2)}, \lambda_2\right)$ are the two points on the curve where the P-V curve shows more linearity. Using the same study case as the previous method, the best and worst estimation results are shown in

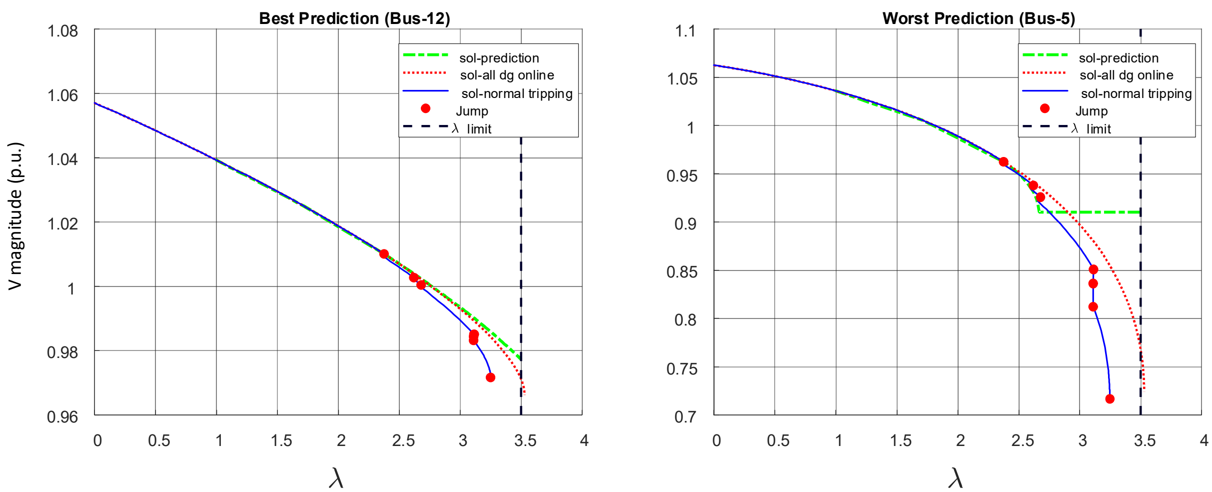

Figure. 43. Voltage Prediction Results – Parabola

Figure. 43. As can be seen, this method works pretty well for some of the cases where the curve shape is closer to a parabola. However, for some of the curves, the simulation may provide very conservative results and the parabola reaches its nose point far faster than the actual P-V curve, which makes the approximation and prediction results invalid.

Therefore, a method using the full family of quadratic functions, or more intuitively an ellipse, is proposed to better fit the P-V curve with a smaller curvature arc around the nose part where the load margin limit is more likely to exist. The quadratic function used as the general form to approximate the curve of bus i is as follows:

$$\begin{bmatrix} \lambda^2 & \lambda V_i & V_i^2 & \lambda & V_i & 1 \end{bmatrix} \begin{bmatrix} \alpha_i \\ \beta_i \\ \gamma_i \\ \sigma_i \\ \eta_i \\ \mu_i \end{bmatrix} = 0 \tag{5-5}$$

Using multiple known points on the P-V curve, one can form up a linear LSE optimization problem. Based on the shape of general P-V curve, the major axis of the ellipse should either lie on or tilt to the λ-axis. Therefore, there is one constraint added to the LSE that guarantees $\alpha_i \leq \gamma_i$ as following:

$$\begin{bmatrix} \lambda^2 & \lambda V_i & V_i^2 & \lambda & V_i & 1 \end{bmatrix} \begin{bmatrix} 1 \\ 0 \\ -1 \\ 0 \\ 0 \\ 0 \end{bmatrix} \leq 0 \tag{5-6}$$

The points used to conduct the LSE process can only be acquired from the P-V curve which only corresponds to the upper-right part of the candidate ellipse. Therefore, in order to bring in enough ellipse information in the LSE formulation and not to lose information provided by the last several points acquired on the actual curve, the points are selected with the following manner:

$$\text{Index}_{\text{selected}} = N_{data\_vol} - [0,\ Fibonacci(3:7)] \tag{5-7}$$

where, $\text{Index}_{\text{selected}}$ is the selected indices of the data points; N_{data_vol} indicates the total number of data points before (including) the first jump point; $Fibonacci(3:7) = \begin{bmatrix} 2 & 3 & 5 & 8 & 13 \end{bmatrix}$ is the third to the seventh entry in the Fibonacci sequence[81]. Selecting the data point for LSE this way will help to maintain the curvature characteristics of the P-V curve. Using the same example case, the prediction results are shown in Figure. 44.

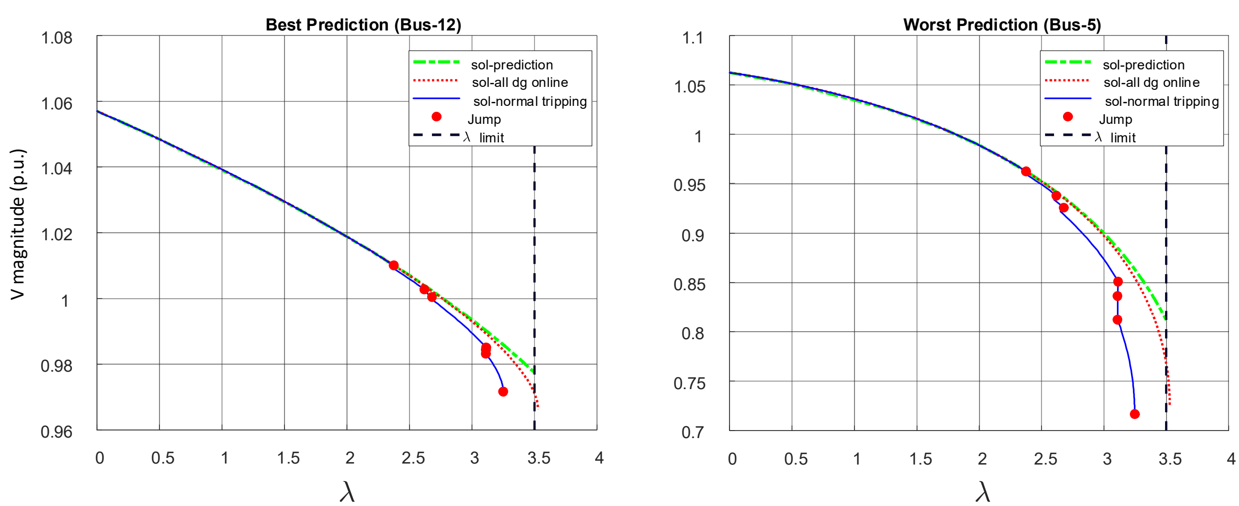

Figure. 44. Voltage Prediction Results – Full Quadratic

As can be seen from the figure, the voltage magnitudes prediction results are much better for buses whose P-V curves have comparatively smaller curvatures. There does exist some compromise for other buses like bus 12. However, because for this kind of buses, their voltages are not very sensitive to the load increase, the voltage drops slower than other buses. The error occurred generally cannot make great differences.

Therefore, the method proposed for the voltage prediction can provide satisfactory voltage magnitudes values estimation at the load margin limit. This will enable us to screen out the critical RGs whose LVRT constraints are being considered to be adjusted in the following sections.

5.4.2 Adaptive LVRT Adjustment Optimization

The core of finding adaptive LVRT settings for the RGs in the system can be summarized to the problem of whether to block the RGs from tripping during the system operation. The blocking here means that the LVRT constants of the concerned RGs are decreased to some extent that the low voltage occurred cannot trigger the tripping actions. In this way, the system is able to avoid jumping to the lower curve resulting in failing to reach the load margin lower limit. However, it is crucial to find out which sets of RGs to block that can enable the system to satisfy this limit and the result is reached through finding the solution that has the minimum change to the LVRT constraints among these feasible sets.

(a) Find feasible RGs blocking solution candidates

Since the critical RGs are acquired based on the aforementioned method in subsection 5.4.1 and the system operation states under original RG LVRT settings are reached as discussed in section 5.3, the load margin variations for different RG blocking status combinations can be estimated. The original simulation results can be taken as a basis from which the variation starts to enact. It might also contain RG blocking actions for the system not being able to jump to another curve, however, these actions might not necessarily be the optimal solution for the system to reach the load margin limit compared to other possible combinations of RG online status. These statuses can naturally be represented by binary variables. For example, if there are 5 RGs in a system, the RGs status parameter can be expressed as $\mathbf{P}_{RG} = \begin{bmatrix} p_1 & p_2 & p_3 & p_4 & p_5 \end{bmatrix}$, where p_1 refers to the connection status of the first RG and so on so forth. $\mathbf{P}_{RG} = \begin{bmatrix} 1 & 0 & 1 & 0 & 0 \end{bmatrix}$ indicates that only RG 1 and RG 3 are connected to the system. If the k-th RG's status has the change of Δp_k, the change in the load margin, $\Delta\lambda$ can be expressed as

$$\Delta\lambda = \frac{d\lambda}{dp_k}\Delta p_k \tag{5-8}$$

Greene et al provided an approach to find out the sensitivity $\frac{d\lambda}{dp_k}$ which is described in [82]. The basic idea is to use the zero eigenvector to eliminate the singular part of the Jacobian matrix term at the nose point. So that the concerned sensitivity part can be derived.

Assume the equilibria of the system satisfy the following equation set:

$$\mathbf{f}\left(\mathbf{x},\, \lambda,\, \mathbf{P}_{RG}\right) = 0 \tag{5-9}$$

where, $\mathbf{f}(\bullet)$ can be derived with the conventional power flow equations; $\mathbf{x}$ refers to the vector of the system states in the power flow formulation which includes the voltage magnitudes and phase angles on each of the buses; λ is the load margin.

At the nose point, the Jacobian matrix $\mathbf{f}_{\mathbf{x}} = \frac{\partial \mathbf{f}}{\partial \mathbf{x}}$ is singular. Therefore, there has to exist a left zero eigenvector $\boldsymbol{\upsilon}\left(\mathbf{x},\, \lambda,\, \mathbf{P}_{RG}\right)$ (a row vector) such that

$$\boldsymbol{\upsilon}(\mathbf{x},\lambda,\mathbf{P}_{RG})\mathbf{f}_{\mathbf{x}}(\mathbf{x},\lambda,\mathbf{P}_{RG})=0 \tag{5-10}$$

This is based on the definition of the zero eigenvector. At the nose point, it is easy to find out that the full Jacobian of $\mathbf{f}(\mathbf{x},\lambda,\mathbf{P}_{RG})$ is zero, which leads to

$$\left.\frac{\partial \mathbf{f}}{\partial \mathbf{x}}\right|_* d\mathbf{x}+\left.\frac{\partial \mathbf{f}}{\partial \lambda}\right|_* d\lambda+\left.\frac{\partial \mathbf{f}}{\partial \mathbf{P}_{RG}}\right|_* d\mathbf{P}_{RG}=0 \tag{5-11}$$

where, $\bullet|_*$ indicates evaluated at the nose point.

Pre-multiply by $\boldsymbol{\upsilon}(\mathbf{x},\lambda,\mathbf{P}_{RG})$ yields,

$$\boldsymbol{\upsilon}\left.\frac{\partial \mathbf{f}}{\partial \lambda}\right|_* d\lambda+\boldsymbol{\upsilon}\left.\frac{\partial \mathbf{f}}{\partial \mathbf{P}_{RG}}\right|_* d\mathbf{P}_{RG}=0 \tag{5-12}$$

The term $\boldsymbol{\upsilon}\left.\frac{\partial \mathbf{f}}{\partial \mathbf{x}}\right|_* d\mathbf{x}$ is eliminated by its zero eigenvector. Further, for any particular parameter p_k within $\mathbf{P}_{RG}$, one has

$$\frac{d\lambda}{dp_k}=-\frac{\boldsymbol{\upsilon}\left.\frac{\partial \mathbf{f}}{\partial p_k}\right|_*}{\boldsymbol{\upsilon}\left.\frac{\partial \mathbf{f}}{\partial \lambda}\right|_*} \tag{5-13}$$

Therefore, with the knowledge of the nose point and information needed by the static calculation of the system under original normal operation conditions, one can find the load margin variation at the nose point with respect to any possible RGs status combination in the system. One thing to be noted here is that the variation of load margin $\Delta\lambda$ refers to the change of nose point load margin of the original P-V curve, which means the load margin after the RG status change of $\Delta\mathbf{P}_{RG}$ is

$$\lambda_{new}^*=\lambda_{original}^*+\Delta\mathbf{P}_{RG}\frac{d\lambda}{d\mathbf{P}_{RG}} \tag{5-14}$$

where λ_{new}^{*} is the load margin of the nose point after the RG status change; $\lambda_{original}^{*}$ is the load margin of the nose point acquired from the simulation results in section 5.3; and

$$\frac{d\lambda}{d\mathbf{P}_{RG}} = \begin{bmatrix} \cdots & \frac{d\lambda}{dp_k} & \cdots \end{bmatrix}^{\mathrm{T}} \tag{5-15}$$

The parameters here are not limited to binary or discrete variables, which can also be a set of continuous variables, even $\mathbf{P}_{RG}$ is discrete in the physical world. This will bring much convenience for future further computation.

It is also noted that the load margin change is an estimated value due to the linear approximation within the derivation process. The detailed explanation can be found in [82]. Therefore, there is a need for CPF computation after the candidate LVRT setting adjustment solutions found for true improvement on load margin validation.

However, at this stage, this method will help us to filter out the feasible LVRT adjustment solutions which can help the system satisfy load margin limit without conducting CPF for every single case, which saves a remarkable amount of computation efforts and costs.

(b) Find corresponding LVRT constants adjustment estimation

After the estimation of the load margin variation brought by the RGs status change, it is simple to filter out the feasible solutions, or which group of RGs to be kept online to make the system satisfy the load margin limit as follows:

$$\lambda_{new}^{*} \geq \lambda_{\text{limit}} \tag{5-16}$$

However, this is only qualitative results. There is still a need to find out how much each RG's LVRT constant to be adjusted to maintain the system on the curve corresponding to the reached feasible solutions.

CPF computation can provide more precise answers, but the computation burden is significant. Therefore, a method to estimate the voltage on the load margin limit of each curve is proposed in this subsection. This method is iterative and starts from known equilibrium points on the original curve. There are two scenarios depending on whether the original curve has passed the load margin limit λ_{limit} or not. For different scenarios, there are different technics to avoid iterative process collapse due to large differences in system states.

Scenario 1: The original curve has passed the load margin limit as shown in Figure. 45.

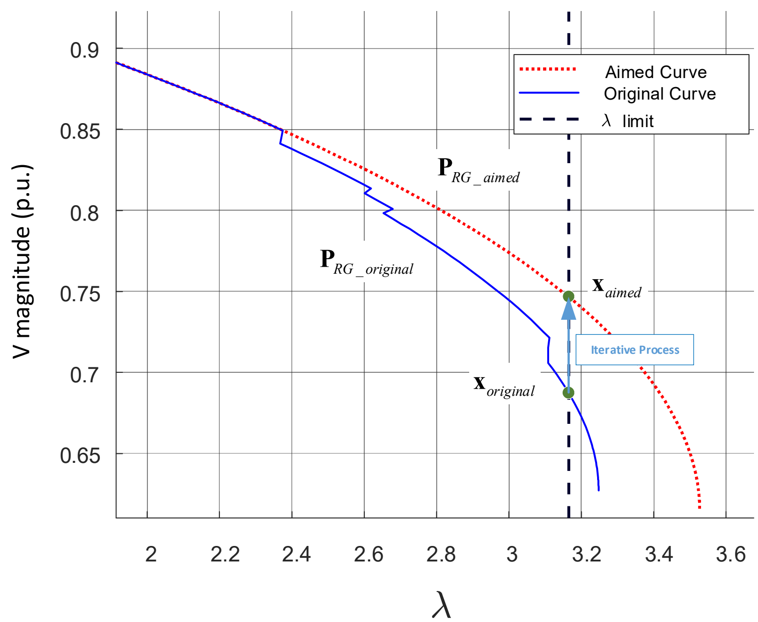

Figure. 45. System State Estimation on Feasible Curves – Scenario 1

As can be seen in the figure, the original curve has passed the load margin limit. However, there is still tripping in the original solution path, which means there is still space to optimize the RGs' operation within this case. Since the only true operation information one has at this stage is the original curve which is specified by RG status $\mathbf{P}_{RG\_original}$, all the computation should be based on this solid information to have more valid results. The purpose here is to find out the voltages of RG equipped buses in the aimed system when it reaches the load margin limit. This aimed system is specified by the corresponding RG status $\mathbf{P}_{RG\_aimed}$. The voltages are parts of the system states $\mathbf{x}_{aimed}$ as shown in the figure. The way to reach these interested states is to find out the system static state equations and using Newton-Raphson method to iteratively approach $\mathbf{x}_{aimed}$ starting from the known $\mathbf{x}_{original}$ which is the states of the original system on the load margin limit.

It is to be noted that the intuition of the starting point of the iterative process is the closest point to the aimed point in the state space. However, in this case, there is no way to find out where the aimed point is. Thus, the most secured starting point would be the known state point which is also on the load margin limit.

Scenario 2: The original curve has not passed the load margin limit as shown in Figure. 46.

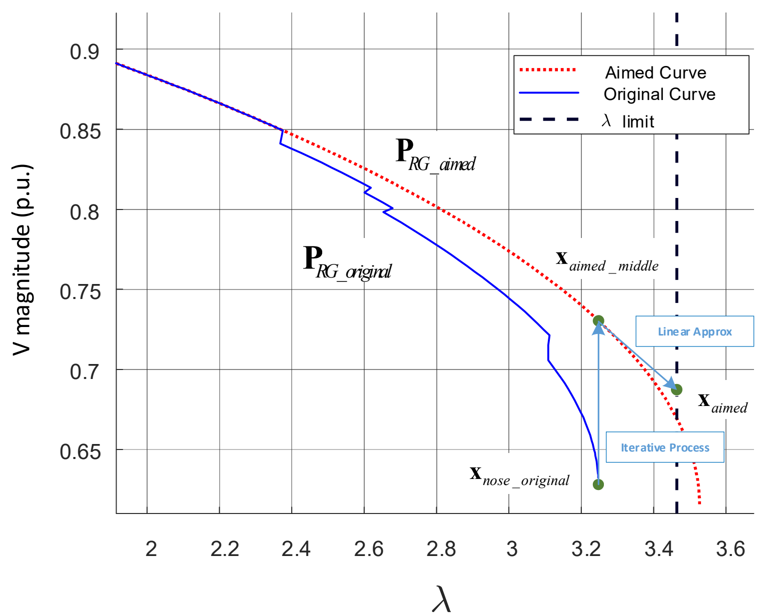

Figure. 46. System State Estimation on Feasible Curves – Scenario 2

As can be seen from the figure, the original curve does not reach the load margin limit. Therefore, it is generally not realistic to use the same method in scenario 1. The closest state point will be the nose point of the original curve $\mathbf{x}_{nose\_original}$. Example cases experiments illustrated that there is a large chance of non-convergence if directly applying the iterative process starting from the point $\mathbf{x}_{nose\_original}$.

Therefore, the method is modified here to first find out the point of $\mathbf{x}_{aimed\_middle}$ with a similar approach in scenario 1. This point is taken as a medium and the voltage values at the load margin limit are reached through linear approximation based on the sensitivity of system states with respect to load margin.

The current concerned RG status $\mathbf{P}_{RG\_current}$ is taken as a feasible candidate blocking solution if the equilibrium point can be founded. This means that for $\mathbf{P}_{RG\_current}$, based on the estimation of load margin improvement, blocking the RGs with the status of 1 in $\mathbf{P}_{RG\_current}$ can help the system to satisfy the load margin limit. The voltages on the RG installed buses at the load margin limit are compared with corresponding RGs' LVRT constant. The adjustment on the LVRT constants under the current solution can be expressed in.

$$\mathbf{D}_{LVRT\_current} = \max\left\{\left(\mathbf{V}_{LVRT} - \mathbf{V}_{RG\_current}\right),\ \mathbf{0}\right\} \tag{5-17}$$

where, $\mathbf{D}_{LVRT\_current}$ is the vector of LVRT adjustment with current RG blocking solution; $\mathbf{V}_{LVRT}$ is the vector of RGs' LVRT constants; $\mathbf{V}_{RG\_current}$ is the vector of voltage magnitudes of RG installed buses; $\max\{\bullet,\ \mathbf{0}\}$ refers to the entry-wise comparison between the subtraction results and zero vector, which means that if the current voltage is higher than the corresponding LVRT constant, then there is no need to adjust the LVRT constant and the adjustment is 0.

Although the accustomed methods for different scenarios are designed, there are still chances that the system cannot find an equilibrium point for estimating the voltages of the RG buses at the load margin limit. The RG statuses of these cases are taken as infeasible solutions.

(c) Find optimal LVRT adjustment solution

The LVRT is a character designed for system security, therefore, the adjustment upon the LVRT constants is preferably small. The feasible candidate RGs blocking solutions are acquired from the previous step. Given the LVRT constants adjustment values for the feasible solutions, the optimum is selected so that the total decrease of all the LVRT constants in the system is the smallest.

It is to be noted that all the quantitative results so far are estimated results. In order to find the true improvement on the load margin and LVRT adjustment values, and to avoid erroneous influence brought by the estimation, the candidates are ranked with respect to the total LVRT adjustment in descending order. The first 5 candidates are selected to conduct further evaluation with CPF. The final LVRT adjustment results are provided by this CPF simulation process to reach more accurate results. The complete process is shown in the following flow chart in Figure. 47. The method is implemented on a study case in the following section.

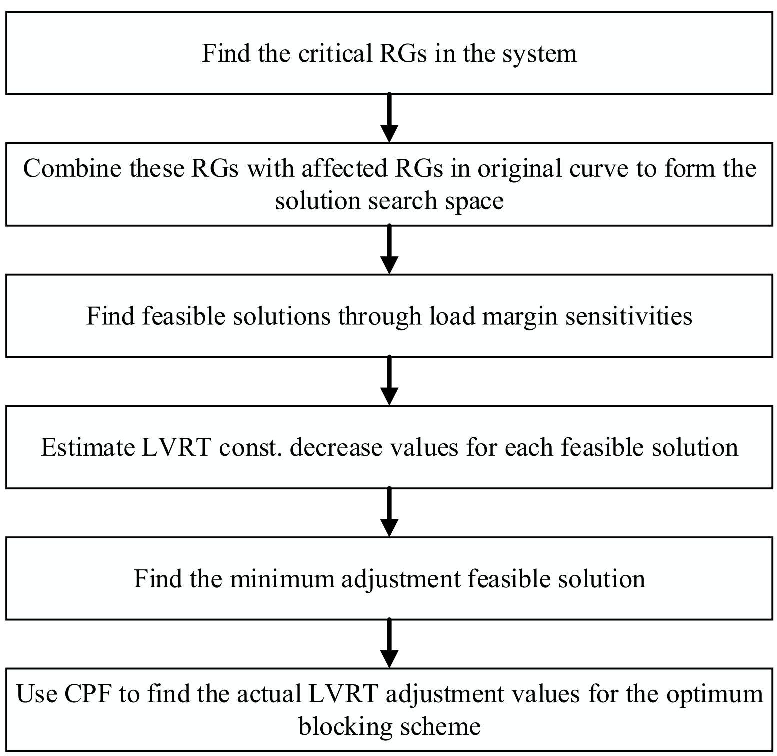

Figure. 47. Flow Chart for Adaptive LVRT Adjustment Method

5.5 Case Study

The study case used is a 9-bus 3-generator 6-RG case. The system diagram is shown in Figure. 48. For every load bus, there is an RG installed providing active power. This design is meant to simulate the high RG penetration system in the real world. The detailed bus and line data are listed in the following tables. The load margin limit is set to be 1.7.

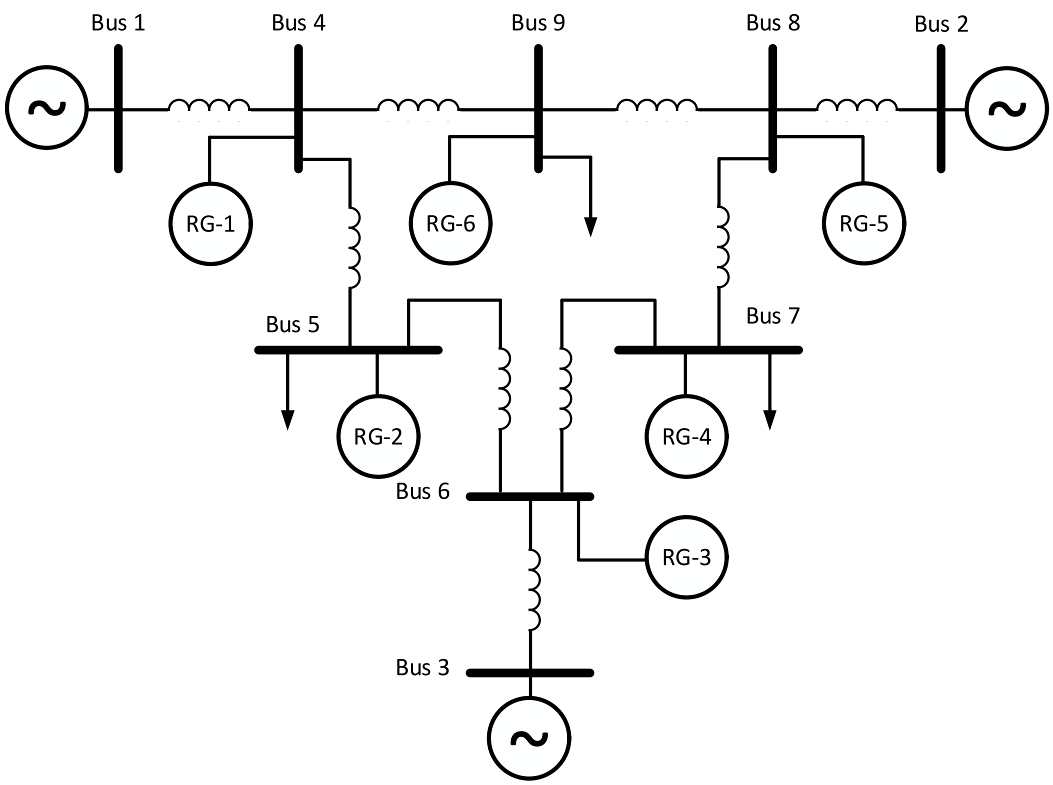

Figure. 48. Study Case Diagram

TABLE 4. STUDY CASE BUS DATA (P.U.)

Bus Number	Bus Type	Voltage Mag	Phase Angle	PG	QG	PD	QD	PG Lower Limit	PG Upper Limit	QG Lower Limit	QG Upper Limit
1	3	1	0	0	0	0	0	0	0	999	-999
2	2	1	0	1.13	0	0	0	0	0	3	-3
3	2	1	0	0.65	0	0	0	0	0	3	-3
4	1	1	0	0	0	0	0	0	0	999	-999
5	1	1	0	0	0	0.9	0.3	0	0	999	-999
6	1	1	0	0	0	0	0	0	0	999	-999
7	1	1	0	0	0	1	0.35	0	0	999	-999
8	1	1	0	0	0	0	0	0	0	999	-999
9	1	1	0	0	0	1.25	0.5	0	0	999	-999

TABLE 5. STUDY CASE LINE DATA (P.U.)

From Bus	To Bus	R	X	y	Online
1	4	0	0.0576	0	1
4	5	0.017	0.092	0.079	1
5	6	0.039	0.17	0.179	1
3	6	0	0.0586	0	1
6	7	0.0119	0.1008	0.1045	1
7	8	0.0085	0.072	0.0745	1
8	2	0	0.0625	0	1
8	9	0.032	0.161	0.153	1
9	4	0.01	0.085	0.088	1

TABLE 6. STUDY CASE RG DATA (P.U.)

Bus Number	PG	QG	LVRT Constant	Connection Status
4	0.1	0	0.8	1
5	0.2	0	0.9	1
6	0.1	0	0.8	1
7	0.5	0	0.83	1
8	0.05	0	0.8	1
9	0.4	0	0.8	1

With original LVRT constants settings, there are three tripping events and one blocking events happening. The original curves of the four events are shown in the chronological order as follows.

Event 1: Tripping of RG on Bus 5 at the load margin of 0.9217 for violating LVRT constant of 0.9 p.u.

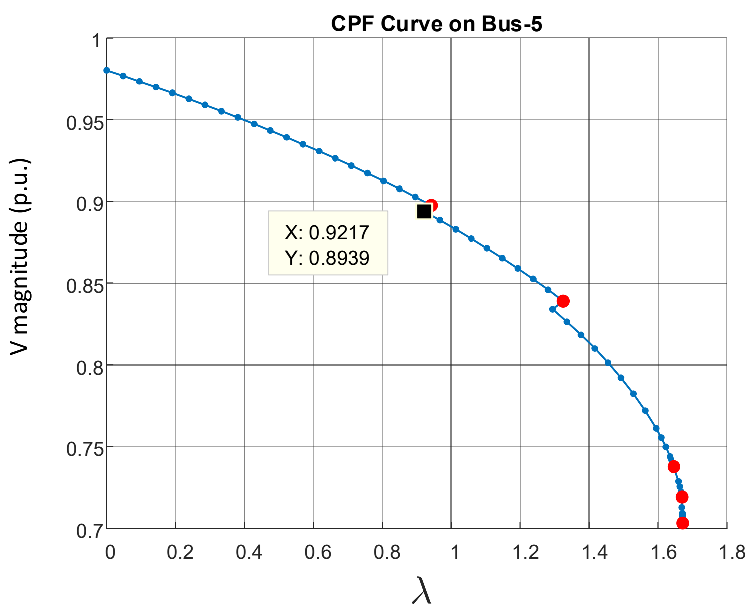

Figure. 49. Event – Tripping RG on Bus 5

Event 2: Tripping of RG on Bus 9 at the load margin of 1.2943 for violating LVRT constant of 0.8 p.u.

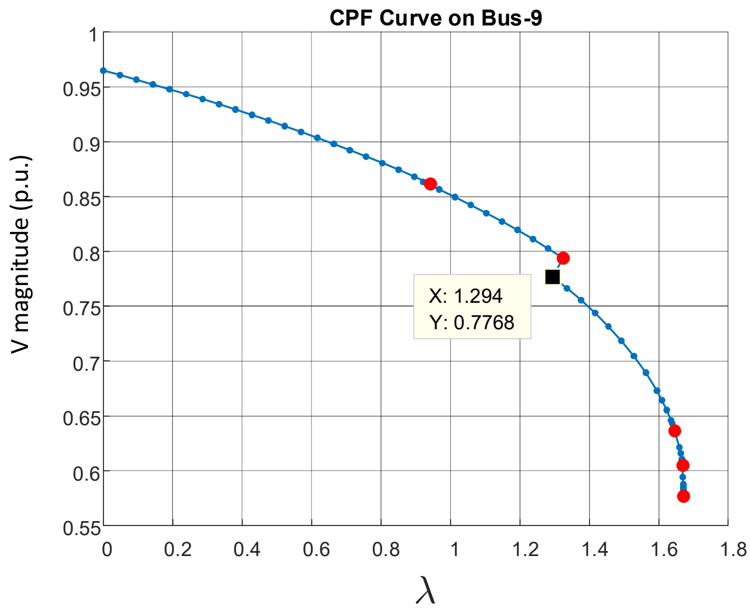

Figure. 50. Event – Tripping RG on Bus 9

Event 3: Blocking of RG on Bus 7 at the load margin of 1.6385 for violating LVRT constant of 0.83 p.u.

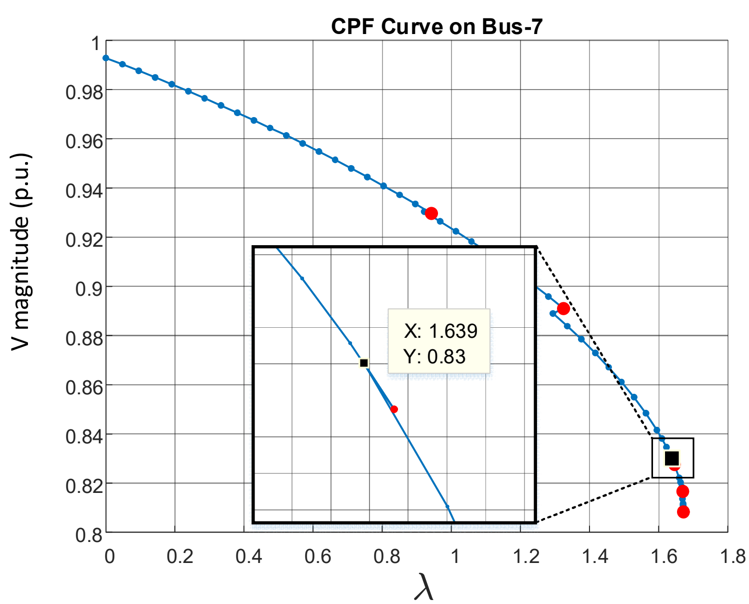

Figure. 51. Event – Blocking RG on Bus 7

Event 4: Tripping of RG on Bus 4 at the load margin of 1.6385 for violating LVRT constant of 0.83 p.u.

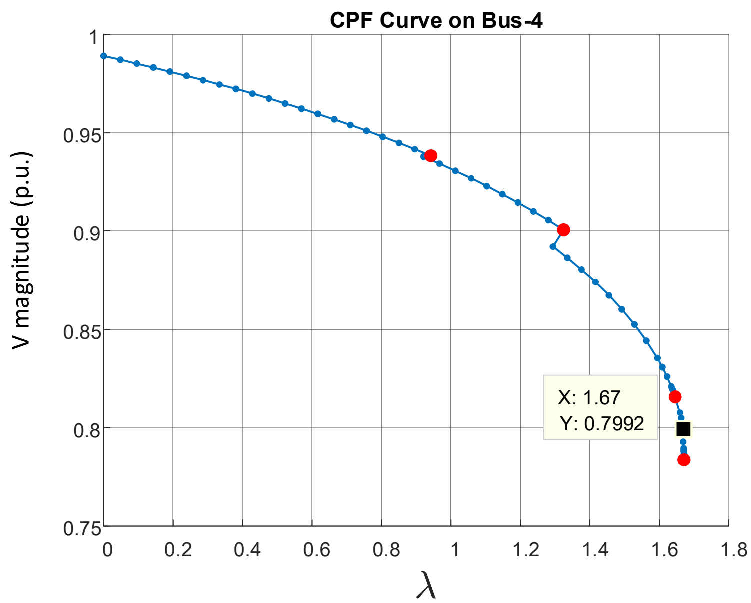

Figure. 52. Event – Blocking RG on Bus 4

The predicted critical buses are Bus 5 and Bus 9. The prediction results as listed as the following:

TABLE 7. CRITICAL BUS PREDICTION

Bus w/ RG	Predicted Voltage (p.u.)	LVRT Constant (p.u.)
4	0.8579	0.8
5	0.7802	0.9
6	0.9298	0.8
7	0.847	0.83
8	0.893	0.8
9	0.7006	0.8

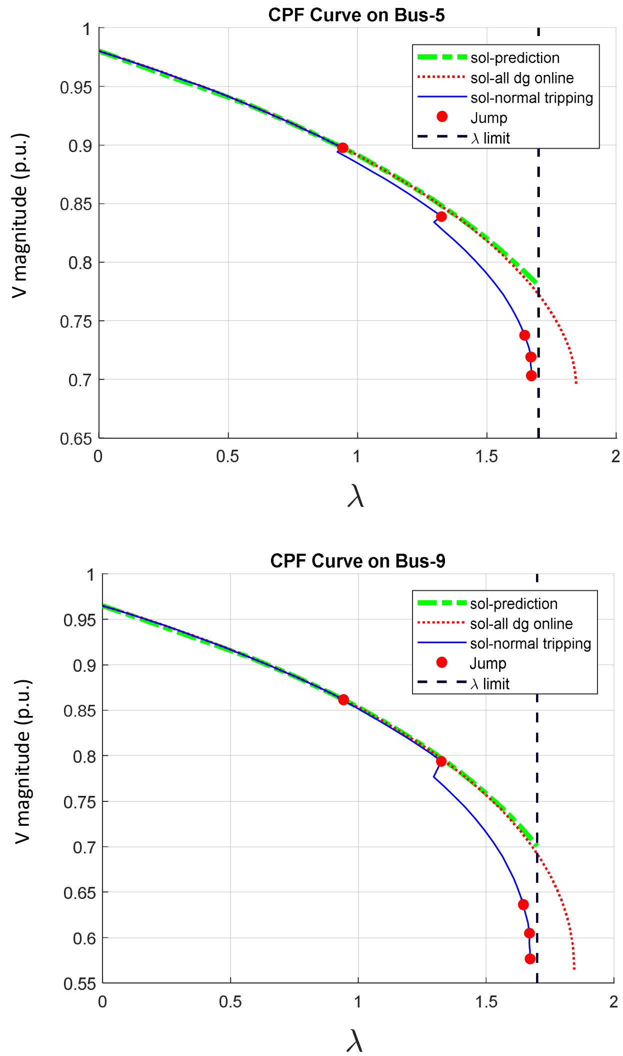

Figure. 53. Critical Bus Voltage Prediction Results

Both of these two buses are included in the original solution and none of the unvisited buses (Bus 6 and Bus 8) are labeled as critical. Therefore, both Bus 6 and Bus 8 are considered to be blocked within the later RG blocking combinations evaluating process.

The top five RG LVRT constant decrease solutions reached with the method introduced as scenario 2 in subsection 5.4.2 (b) since the load margin of the original curve is 1.6723 which does not reach the load margin limit of 1.7. These solutions are listed as follows:

TABLE 8. ESTIMATED RG BLOCKING SOLUTIONS W/ LOWEST LVRT ADJUSTMENT

		Bus 4	Bus 5	Bus 6	Bus 7	Bus 8	Bus 9	Load Margin Increase
Solution 1	RG Blocking	1	0	1	1	0	1	0.1529
	LVRT Const. Decrease	0	0	0	0	0	0.1153	
Solution 2	RG Blocking	0	0	1	1	1	1	0.1475
	LVRT Const. Decrease	0	0	0	0	0	0.1187	
Solution 3	RG Blocking	1	0	0	0	0	1	0.1332
	LVRT Const. Decrease	0	0	0	0	0	0.1282	
Solution 4	RG Blocking	0	0	0	0	1	1	0.1279
	LVRT Const. Decrease	0	0	0	0	0	0.1303	
Solution 5	RG Blocking	0	1	1	1	0	0	0.0292
	LVRT Const. Decrease	0	0.1713	0	0.0139	0	0	

Evaluate the previous solutions with the actual CPF process. The true necessary decrease on LVRT constants and the corresponding increase on load margin are listed in the following table. Among these solutions, the one ranked fifth in the previous table is proved to be infeasible.

Therefore, the actual best result is only blocking Bus 9 by adjusting it LVRT constant from 0.8 to 0.6822, and this will help to increase the system load margin from 1.6723 to 1.7901 which satisfies the load margin limit of 1.7.

TABLE 9. LVRT ADJUSTMENT EVALUATION W/ CPF

		Bus 4	Bus 5	Bus 6	Bus 7	Bus 8	Bus 9	Load Margin Increase
Solution 1	RG Blocking	1	0	1	1	0	1	0.1178
	LVRT Const. Decrease	0	0	0	0	0	0.1178	
Solution 2	RG Blocking	0	0	1	1	1	1	0.1134
	LVRT Const. Decrease	0	0	0	0	0	0.1178	
Solution 3	RG Blocking	1	0	0	0	0	1	0.0887
	LVRT Const. Decrease	0	0	0	0	0	0.1178	
Solution 4	RG Blocking	0	0	0	0	1	1	0.0830
	LVRT Const. Decrease	0	0	0	0	0	0.1178	

5.6 Discussions

An approach to adaptively adjust the RG LVRT settings integrated into the system to satisfy the load margin limit is proposed in this section. This method can help the system to integrate larger penetration of renewable energy without the need to worry about the insecurity brought by the possibility of those RGs being involved in system local disturbances. At the same time, this method largely decreases the computation efforts brought by remarkably repetitively using CPF with various estimation technics. The approach is deployed to the 9-bus test case. The results demonstrated the effectiveness of the method. Proper solution schemes are proposed and the load margin limit is satisfied with the RG LVRT constants adjusting plan.

There is also a potential for future works based on the established method. The method can be deployed to larger scale test cases which will further reveal its efficient characteristic by filtering out infeasible and less effective RGs blocking combinations with estimation. This can be phenomenal in terms of saving computation efforts especially for a large number of RGs integrated systems. The selection of the number of sorted candidate RGs blocking combinations can also be made to be adaptive to the system's characteristics and/or users' requirements. There is also a possibility to improve the objective function for candidate solutions sorting over the simple summation of LVRT change which is used here. For example, the RG capacity can be considered as a weight when evaluating the impacts of corresponding RG LVRT variation.

CHAPTER 6. CONCLUSIONS AND FUTURE WORK

This dissertation focuses on the power system transient and voltage stability assessment and corresponding control mechanism considering renewables energy integration based on the calibrated system model with PMU measurements. The transmission line parameters in the system are firstly estimated with the proposed method. This method takes advantages of the widely utilized PMU measurements. The error characteristics of the PMU measurement data is studied and the corresponding error model is constructed. The algorithm for system line parameters estimation and data utilization method is designed accordingly. Test cases study demonstrates the effectiveness and efficiency of the proposed approach. The whole method is built upon the assumption of the sole reference, which relives utilities' potential economic burden to purchase multiple costly revenue measurement hardware and endures the method with more practicality in real-world utilization.

The validated model built with these more accurate line parameters sets up the foundation for further analysis and computation of system transient and voltage stability which is enabled to provide significant guidance for system operation based on more factual system information and less mismatch with the reality. With the renewables integration as the main concern, the method based on LFF and CSR is proposed. The LVRT characteristics of the renewables are transformed into state space and the customized polytopic approximation method is introduced to adapt this operation limits to the CSR estimation process. A test case is used to illustrate the CSR estimation process. It is intuitively reasonable and shown in the results that the integration of renewables will bring negative influence to the system constrained stability region. Hence, it is necessary to use the proposed method for much less conservative estimation of the stability region close to the renewables operation limit where the system states will more possibly locate when the system suffers from disturbances.

The LVRT is taken as a standardized operation limit when assessing the system CSR. The problem thus becomes 'is it possible to find out a method to actively and adaptively adjust the LVRT curve for better and less conservative system stability', which is more directly investigated from the perspective of system voltage security. The system load margin is set to be the metric and its lower limit the final goal to reach. A voltage prediction method is formulated to select critical RGs for downscale the searching space dimensionality. Sensitivity based estimation method is established to find out the potential RGs and the quantity of their LVRT constants to be adjusted. The optimization is conducted to find out the feasible adjustment scheme with minimum LVRT adjustment. The approach is tested with a study case. The results show that the tripping of RGs as the system loads rise can very possibly cause the lack of load margin in the system and thus endangers the system voltage security. By adjusting the LVRT constants of some of the RGs, they are enabled to bear more severe low voltage scenarios and help to maintain the system load margin. Due to the effective prediction and estimation method proposed, the whole approach is efficient and scalable without enormous computation burden brought by repeating the CPF process.

To sum up, the study presented in this work addresses the transient stability assessment constrained by renewables operation limits and adaptive adjustment of these limits for improved system voltage security, which are both based on the timely calibrated system model with PMU measurements. Given the conclusions reached addressing these contents, there are still several possible future works to be studied:

- **Short transmission lines parameters estimation**: It can be seen in CHAPTER 3 that the algorithm provides estimation results with comparatively larger errors. The main reasons are proposed and can be addressed by introducing more numerically stable technics in future research.

- **More detailed LVRT constraints**: The LVRT constraints are formulated with constants in CHAPTER 4 for simplicity. The more detailed LVRT constraints can include more dynamic characteristics and information from the original LVRT curve and will help bring more reality into the assessment solution process.

- **More detailed RG dynamic model**: Similar to introducing more details about the LVRT constraints, the deployment of the more detailed RG dynamic model can help to build up a system model closer to reality. Currently, in this work, the RGs are taken as negative active loads when constructing the system internal node model, which leaves the potential for further improvement.

- **Large scale study cases**: The CSR assessment method proposed in this work tends to create and fully exploit linearity and convexity of the model and constraints, which guarantees its scalability. The computation of the introduced test case has the time complexity in the dozen second scale. Thus, implementing the proposed method to large scale study cases can be conducted in the future.

- **More robust LVRT adjustment scheme**: CPF used in CHAPTER 5 is a conventional and reliable method for system voltage tracking under various load status. However, the limitation is that the variation of the load in the system is synchronized, which is not the case in reality. At the same time, there is also uncertainty and intermittence in RGs power output. Hence, it is worth studying that the uncertainty of the RG output and load change is taken into consideration and more robust technics are to be introduced to formulate a more robust LVRT adjustment method.

REFERENCES

[1] REN21, “RENEWABLES 2018 GLOBAL STATUS REPORT.” [Online]. Available: http://www.ren21.net/gsr-2018. [Accessed: 20-Mar-2019].

[2] “IEA - World Energy Statistics and Balances.” [Online]. Available: https://www.iea.org/classicstats/relateddatabases/worldenergystatisticsandbalances/. [Accessed: 20-Mar-2019].

[3] “World Energy Outlook 2017,” *IEA Webstore*. [Online]. Available: https://webstore.iea.org/world-energy-outlook-2017. [Accessed: 20-Mar-2019].

[4] “U.S. Energy Information Administration - EIA - Independent Statistics and Analysis.” [Online]. Available: https://www.eia.gov/outlooks/aeo/data/browser/#/?id=50-IEO2017&region=0-0&cases=Reference&start=2010&end=2020&f=A&linechart=Reference-d082317.2-50-IEO2017&map=&sourcekey=0. [Accessed: 20-Mar-2019].

[5] APS, “Integrating Renewable Electricity on the Grid.” [Online]. Available: https://www.aps.org/policy/reports/popa-reports/integrating.cfm. [Accessed: 20-Mar-2019].

[6] N. Mohammadi, J. Taylor, and Y. Wang, “Towards Smarter Cities: Linking Human Mobility and Energy Use Fluctuations across Building Types,” *Hawaii Int. Conf. Syst. Sci. 2017 HICSS-50*, Jan. 2017.

[7] Wang Yan and Taylor John E., “DUET: Data-Driven Approach Based on Latent Dirichlet Allocation Topic Modeling,” *J. Comput. Civ. Eng.*, vol. 33, no. 3, p. 04019023, May 2019.

[8] Y. Wang, Q. Wang, and J. E. Taylor, “Aggregated responses of human mobility to severe winter storms: An empirical study,” *PLOS ONE*, vol. 12, no. 12, p. e0188734, Dec. 2017.

[9] Y. Wang and J. E. Taylor, “Coupling sentiment and human mobility in natural disasters: a Twitter-based study of the 2014 South Napa Earthquake,” *Nat. Hazards*, vol. 92, no. 2, pp. 907–925, Jun. 2018.

[10] C. Wang, D. Wu, H. Zeng, and V. A. Centeno, “CPS based electric vehicle charging directing system design in Smart Grid,” in *2016 IEEE Power Energy Society Innovative Smart Grid Technologies Conference (ISGT)*, 2016, pp. 1–5.

[11] C. Wang, J. Delport, and Y. Wang, “Lateral Motion Prediction of On-Road Preceding Vehicles: A Data-Driven Approach,” *Sensors*, vol. 19, no. 9, p. 2111, Jan. 2019.

[12] N. Muralidhar *et al.*, “Illiad: InteLLigent Invariant and Anomaly Detection in Cyber-Physical Systems,” *ACM Trans Intell Syst Technol*, vol. 9, no. 3, pp. 35:1–35:20, Jan. 2018.

[13] P. Beiter, “2016 Renewable Energy Grid Integration Data Book,” p. 93.

[14] X. Li, C. Mishra, and J. De La Ree, “Frequency Control of Decoupled Synchronous Machine Using Koopman Operator Based Model Predictive,” in *arXiv:1901.05341 [eess]*, 2019.

[15] C. Mishra, J. S. Thorp, V. A. Centeno, and A. Pal, “Transient Stability Assessment of Cascade Tripping of Renewable Sources Using SOS,” in *2018 IEEE Power Energy Society General Meeting (PESGM)*, 2018, pp. 1–5.

[16] Z. Nie, D. Yang, V. Centeno, and K. D. Jones, “A PMU-based voltage security assessment framework using hoeffding-tree-based learning,” in *2017 19th International Conference on Intelligent System Application to Power Systems (ISAP)*, 2017, pp. 1–6.

[17] E. Mitchell-Colgan, C. Mishra, and V. A. Centeno, “Optimal wind farm placement considering system constraints and investment and uncertainty costs,” in *2015 IEEE Power Energy Society General Meeting*, 2015, pp. 1–5.

[18] “IEEE Standard for Interconnection and Interoperability of Distributed Energy Resources with Associated Electric Power Systems Interfaces,” *IEEE Std 1547-2018 Revis. IEEE Std 1547-2003*, pp. 1–138, Apr. 2018.

[19] M. Bockarjova and G. Andersson, “Transmission Line Conductor Temperature Impact on State Estimation Accuracy,” in *2007 IEEE Lausanne Power Tech*, 2007, pp. 701–706.

[20] “IEEE Standard Requirements for Instrument Transformers,” *IEEE Std C5713-2008 Revis. IEEE Std C5713-1993*, pp. 1–90, Jul. 2008.

[21] P. Kundur *et al.*, “Definition and classification of power system stability IEEE/CIGRE joint task force on stability terms and definitions,” *IEEE Trans. Power Syst.*, vol. 19, no. 3, pp. 1387–1401, Aug. 2004.

[22] A. H. El-abiad and K. Nagappan, “Transient Stability Regions of Multimachine Power Systems,” *IEEE Trans. Power Appar. Syst.*, vol. PAS-85, no. 2, pp. 169–179, Feb. 1966.

[23] A. Michel, A. Fouad, and V. Vittal, “Power system transient stability using individual machine energy functions,” *IEEE Trans. Circuits Syst.*, vol. 30, no. 5, pp. 266–276, May 1983.

[24] A. Llamas, “Assessment of direct methods in power system transient stability analysis for on-line applications,” 1992.

[25] “Proposed Terms amp; Definitions for Power System Stability,” *IEEE Trans. Power Appar. Syst.*, vol. PAS-101, no. 7, pp. 1894–1898, Jul. 1982.

[26] V. Venkatasubramanian, H. Schättler, and J. Zaborszky, “Stability Regions for Differential-Algebraic Systems,” in *Systems, Models and Feedback: Theory and Applications*, A. Isidori and T.-J. Tarn, Eds. Boston, MA: Birkhäuser Boston, 1992, pp. 385–402.

[27] G. A. Maria, C. Tang, and J. Kim, “Hybrid transient stability analysis (power systems),” *IEEE Trans. Power Syst.*, vol. 5, no. 2, pp. 384–393, May 1990.

[28] T. Athay, R. Podmore, and S. Virmani, “A Practical Method for the Direct Analysis of Transient Stability,” *IEEE Trans. Power Appar. Syst.*, vol. PAS-98, no. 2, pp. 573–584, Mar. 1979.

[29] H.-D. Chiang, Felix. F. Wu, and Pravin. P. Varaiya, “A BCU method for direct analysis of power system transient stability,” *IEEE Trans. Power Syst.*, vol. 9, no. 3, pp. 1194–1208, Aug. 1994.

[30] C. Mishra, J. S. Thorp, V. A. Centeno, and A. Pal, “Estimating Relevant Portion of Stability Region using Lyapunov Approach and Sum of Squares,” in *2018 IEEE Power Energy Society General Meeting (PESGM)*, 2018, pp. 1–5.

[31] C. Mishra, J. S. Thorp, V. A. Centeno, and A. Pal, “Stability region estimation under low voltage ride through constraints using sum of squares,” in *2017 North American Power Symposium (NAPS)*, 2017, pp. 1–6.

[32] D. Eltigani and S. Masri, “Challenges of integrating renewable energy sources to smart grids: A review,” *Renew. Sustain. Energy Rev.*, vol. 52, pp. 770–780, Dec. 2015.

[33] D. Yang, Z. Nie, K. Jones, and V. Centeno, “Adaptive decision-trees-based regional voltage control,” in *2017 North American Power Symposium (NAPS)*, 2017, pp. 1–6.

[34] D. Yang, “A power system network partition framework for data-driven regional voltage control,” in *2017 North American Power Symposium (NAPS)*, 2017, pp. 1–6.

[35] V. Ajjarapu and C. Christy, “The continuation power flow: a tool for steady state voltage stability analysis,” in *[Proceedings] Conference Papers 1991 Power Industry Computer Application Conference*, 1991, pp. 304–311.

[36] A. G. Phadke and J. S. Thorp, *Synchronized Phasor Measurements and Their Applications*. Springer US, 2008.

[37] C. Mishra, K. D. Jones, A. Pal, and V. A. Centeno, "Binary particle swarm optimisation-based optimal substation coverage algorithm for phasor measurement unit installations in practical systems," *IET Gener. Transm. Amp Distrib.*, vol. 10, no. 2, pp. 555–562, Feb. 2016.

[38] A. Pal, C. Mishra, A. K. S. Vullikanti, and S. S. Ravi, "General optimal substation coverage algorithm for phasor measurement unit placement in practical systems," *IET Gener. Transm. Amp Distrib.*, vol. 11, no. 2, pp. 347–353, Jan. 2017.

[39] S. A. Boyer, *Scada: Supervisory Control And Data Acquisition*, 4th ed. USA: International Society of Automation, 2009.

[40] F. Mahmood, H. Hooshyar, J. Lavenius, A. Bidadfar, P. Lund, and L. Vanfretti, "Real-Time Reduced Steady-State Model Synthesis of Active Distribution Networks Using PMU Measurements," *IEEE Trans. Power Deliv.*, vol. 32, no. 1, pp. 546–555, Feb. 2017.

[41] Q. Jiang, B. Wang, and X. Li, "An Efficient PMU-Based Fault-Location Technique for Multiterminal Transmission Lines," *IEEE Trans. Power Deliv.*, vol. 29, no. 4, pp. 1675–1682, Aug. 2014.

[42] M. Pignati, L. Zanni, P. Romano, R. Cherkaoui, and M. Paolone, "Fault Detection and Faulted Line Identification in Active Distribution Networks Using Synchrophasors-Based Real-Time State Estimation," *IEEE Trans. Power Deliv.*, vol. 32, no. 1, pp. 381–392, Feb. 2017.

[43] D. Shi, D. J. Tylavsky, and N. Logic, "An Adaptive Method for Detection and Correction of Errors in PMU Measurements," *IEEE Trans. Smart Grid*, vol. 3, no. 4, pp. 1575–1583, Dec. 2012.

[44] X. Zhang *et al.*, "Experimental measurement of PMU error distribution and its impact on load model identification," in *2016 IEEE Power and Energy Society General Meeting (PESGM)*, 2016, pp. 1–5.

[45] Q. Zhang, V. Vittal, G. T. Heydt, N. Logic, and S. Sturgill, "The Integrated Calibration of Synchronized Phasor Measurement Data in Power Transmission Systems," *IEEE Trans. Power Deliv.*, vol. 26, no. 4, pp. 2573–2581, Oct. 2011.

[46] Z. Wu, K. Thomas, R. Sun, V. A. Centeno, and A. G. Phadke, "Three-phase instrument transformer calibration with synchronized phasor measurements," in *2012 IEEE PES Innovative Smart Grid Technologies (ISGT)*, 2012, pp. 1–6.

[47] A. Pal, P. Chatterjee, J. S. Thorp, and V. A. Centeno, "Online Calibration of Voltage Transformers Using Synchrophasor Measurements," *IEEE Trans. Power Deliv.*, vol. 31, no. 1, pp. 370–380, Feb. 2016.

[48] A. G. Phadke and J. S. Thorp, "HISTORY AND APPLICATIONS OF PHASOR MEASUREMENTS," in *2006 IEEE PES Power Systems Conference and Exposition*, 2006, pp. 331–335.

[49] P. Chatterjee, A. Pal, J. S. Thorp, J. D. L. R. Lopez, and V. A. Centeno, "Error reduction of phasor measurement unit data considering practical constraints," *IET Gener. Transm. Amp Distrib.*, vol. 12, no. 10, pp. 2332–2339, Feb. 2018.

[50] G. Benmouyal, E. O. Schweitzer, and A. Guzman, "Synchronized phasor measurement in protective relays for protection, control, and analysis of electric power systems," in *57th Annual Conference for Protective Relay Engineers, 2004*, 2004, pp. 419–450.

[51] B. Kamgar-Parsi, B. Kamgar-Parsi, and M. Brosh, "Distribution and moments of the weighted sum of uniforms random variables, with applications in reducing monte carlo simulations," *J. Stat. Comput. Simul.*, vol. 52, no. 4, pp. 399–414, Jul. 1995.

[52] C. Mishra, V. A. Centeno, and A. Pal, "Kalman-filter based recursive regression for three-phase line parameter estimation using synchrophasor measurements," in *2015 IEEE Power Energy Society General Meeting*, 2015, pp. 1–5.

[53] Z. Wu, L. T. Zora, and A. G. Phadke, "Simultaneous transmission line parameter and PMU measurement calibration," in *2015 IEEE Power Energy Society General Meeting*, 2015, pp. 1–5.

[54] M. Asprou and E. Kyriakides, "Identification and Estimation of Erroneous Transmission Line Parameters Using PMU Measurements," *IEEE Trans. Power Deliv.*, vol. 32, no. 6, pp. 2510–2519, Dec. 2017.

[55] P. Ren, H. Lev-Ari, and A. Abur, "Tracking Three-Phase Untransposed Transmission Line Parameters Using Synchronized Measurements," *IEEE Trans. Power Syst.*, vol. 33, no. 4, pp. 4155–4163, Jul. 2018.

[56] D. Shi, D. J. Tylavsky, K. M. Koellner, N. Logic, and D. E. Wheeler, "Transmission line parameter identification using PMU measurements," *Eur. Trans. Electr. Power*, vol. 21, no. 4, pp. 1574–1588, 2011.

[57] "Texas 2000-June 2016 - Illinois Center for a Smarter Electric Grid (ICSEG)." .

[58] D. F. Williamson, R. A. Parker, and J. S. Kendrick, “The box plot: a simple visual method to interpret data,” *Ann. Intern. Med.*, vol. 110, no. 11, pp. 916–921, Jun. 1989.

[59] C. Mishra, S. P. Singh, and J. Rokadia, “Optimal power flow in the presence of wind power using modified cuckoo search,” *IET Gener. Transm. Amp Distrib.*, vol. 9, no. 7, pp. 615–626, Feb. 2015.

[60] “Direct Methods for Stability Analysis of Electric Power Systems: Theoretical Foundation, BCU Methodologies, and Applications: Hsiao-Dong Chiang: 9780470484401: Amazon.com: Books.” [Online]. Available: https://www.amazon.com/Methods-Stability-Analysis-Electric-Systems/dp/0470484403. [Accessed: 10-Sep-2018].

[61] C. L. Barrett *et al.*, “Impact of a Surface Nuclear Blast on the Transient Stability of the Power System,” in *Critical Information Infrastructures Security*, 2016, pp. 153–158.

[62] K. L. Praprost and K. A. Loparo, “A stability theory for constrained dynamic systems with applications to electric power systems,” *IEEE Trans. Autom. Control*, vol. 41, no. 11, pp. 1605–1617, Nov. 1996.

[63] A. P. Sohn, A. L. Abrantes, L. F. C. Alberto, and H. Chiang, “Stability region of a wind power system under low-voltage ride-through constraint,” in *2016 IEEE Power and Energy Society General Meeting (PESGM)*, 2016, pp. 1–5.

[64] H. Chiang, F. F. Wu, P. P. Varaiya, and C. Tan, “Theory of the potential energy boundary surface,” in *1985 24th IEEE Conference on Decision and Control*, 1985, pp. 49–51.

[65] T. L. Vu and K. Turitsyn, “Lyapunov Functions Family Approach to Transient Stability Assessment,” *IEEE Trans. Power Syst.*, vol. 31, no. 2, pp. 1269–1277, Mar. 2016.

[66] F. Dorfler and F. Bullo, “Kron Reduction of Graphs With Applications to Electrical Networks,” *IEEE Trans. Circuits Syst. Regul. Pap.*, vol. 60, no. 1, pp. 150–163, Jan. 2013.

[67] A. M. Lyapunov, “The general problem of the stability of motion,” *Int. J. Control*, vol. 55, no. 3, pp. 531–534, Mar. 1992.

[68] C. J. Tavora and O. J. M. Smith, “Stability Analysis of Power Systems,” *IEEE Trans. Power Appar. Syst.*, vol. PAS-91, no. 3, pp. 1138–1144, May 1972.

[69] “Nonlinear Systems (3rd Edition): Hassan K. Khalil: 9780130673893: Amazon.com: Books.” [Online]. Available: https://www.amazon.com/Nonlinear-Systems-3rd-Hassan-Khalil/dp/0130673897. [Accessed: 03-Oct-2018].

[70] S. P. Boyd and L. Vandenberghe, *Convex optimization*. Cambridge, UK ; New York: Cambridge University Press, 2004.

[71] C. Mishra, "Studying the Impact of Solar Photovoltaic on Transient Stability of Power Systems using Direct Methods," Dec. 2017.

[72] N. M. Brownell, J. T. Kelliher, and S. G. Kelly, "Interconnection for Wind Energy," p. 85, 2005.

[73] J. Kennedy and R. Eberhart, "Particle swarm optimization," in *Proceedings of ICNN'95 - International Conference on Neural Networks*, 1995, vol. 4, pp. 1942–1948 vol.4.

[74] P. Kundur, *Power system stability and control*. New York, NY: McGraw-Hill, 1994.

[75] A. Tbaileh, C. Mishra, and K. Thomas, "PV impacts on dynamic voltage stability," in *SoutheastCon 2017*, 2017, pp. 1–5.

[76] H. M. Hasanien, "An Adaptive Control Strategy for Low Voltage Ride Through Capability Enhancement of Grid-Connected Photovoltaic Power Plants," *IEEE Trans. Power Syst.*, vol. 31, no. 4, pp. 3230–3237, Jul. 2016.

[77] C. Wang, "The investment allocation of the distribution system optimization based on an improved PSO," in *2014 IEEE PES General Meeting | Conference Exposition*, 2014, pp. 1–5.

[78] T. Blu, P. Thevenaz, and M. Unser, "Linear Interpolation Revitalized," *IEEE Trans. Image Process.*, vol. 13, no. 5, pp. 710–719, May 2004.

[79] F. Gao, J. S. Thorp, A. Pal, and S. Gao, "Dynamic state prediction based on Auto-Regressive (AR) Model using PMU data," in *2012 IEEE Power and Energy Conference at Illinois*, 2012, pp. 1–5.

[80] H.-D. Chiang, C.-S. Wang, and A. J. Flueck, "Look-ahead voltage and load margin contingency selection functions for large-scale power systems," *IEEE Trans. Power Syst.*, vol. 12, no. 1, pp. 173–180, Feb. 1997.

[81] A. F. Horadam, "A Generalized Fibonacci Sequence," *Am. Math. Mon.*, vol. 68, no. 5, pp. 455–459, May 1961.

[82] S. Greene, I. Dobson, and F. L. Alvarado, "Sensitivity of the loading margin to voltage collapse with respect to arbitrary parameters," *IEEE Trans. Power Syst.*, vol. 12, no. 1, pp. 262–272, Feb. 1997.